



## DEFENSE TECHNICAL INFORMATION CENTER

*Information for the Defense Community*

DTIC<sup>®</sup> has determined on 

Month	Day	Year
05	16	2008

 that this Technical Document has the Distribution Statement checked below. The current distribution for this document can be found in the DTIC<sup>®</sup> Technical Report Database.

☒ **DISTRIBUTION STATEMENT A.** Approved for public release; distribution is unlimited.

☐ **© COPYRIGHTED.** U.S. Government or Federal Rights License. All other rights and uses except those permitted by copyright law are reserved by the copyright owner.

☐ **DISTRIBUTION STATEMENT B.** Distribution authorized to U.S. Government agencies only. Other requests for this document shall be referred to controlling office.

☐ **DISTRIBUTION STATEMENT C.** Distribution authorized to U.S. Government Agencies and their contractors. Other requests for this document shall be referred to controlling office.

☐ **DISTRIBUTION STATEMENT D.** Distribution authorized to the Department of Defense and U.S. DoD contractors only. Other requests shall be referred to controlling office.

☐ **DISTRIBUTION STATEMENT E.** Distribution authorized to DoD Components only. Other requests shall be referred to controlling office.

☐ **DISTRIBUTION STATEMENT F.** Further dissemination only as directed by controlling office or higher DoD authority.

*Distribution Statement F is also used when a document does not contain a distribution statement and no distribution statement can be determined.*

☐ **DISTRIBUTION STATEMENT X.** Distribution authorized to U.S. Government Agencies and private individuals or enterprises eligible to obtain export-controlled technical data in accordance with DoDD 5230.25.

CU  
PEGRAM-  
PR  
Jan-  
Dec69  
c.1

# PEGRAM NUCLEAR PHYSICS LABORATORIES

**Columbia University**  
**in the City of New York**

LOAN COPY: RETURN TO  
AFWL (WL0L)  
KIRTLAND AFB, N MEX

Department of Physics



PROGRESS REPORT FOR JANUARY 1969 THROUGH DECEMBER 1969  
TO THE UNITED STATES ATOMIC ENERGY COMMISSION

The research reported in this document was  
made possible through the support extended  
to Columbia University by the United States  
Atomic Energy Commission, under

A.E.C. Contract AT(30-1) 73

W. W. Havens, Jr., Director

Reproduction in whole or in part is permitted for any purpose  
of the United States Government





## LEGAL NOTICE

This report was prepared as an account of Government sponsored work. Neither the United States, nor the Commission, nor any person acting on behalf of the Commission:

- A. Makes any warranty or representation, expressed or implied, with respect to the accuracy, completeness, or usefulness of the information contained in this report, or that the use of any information, apparatus, method, or process disclosed in this report may not infringe privately owned rights; or
- B. Assumes any liabilities with respect to the use of, or for damages resulting from the use of any information, apparatus, method, or process disclosed in this report.

As used in the above, "person acting on behalf of the Commission" includes any employee or contractor of the Commission, or employee of such contractor, to the extent that such employee or contractor of the Commission, or employee of such contractor prepares, disseminates, or provides access to, any information pursuant to his employment or contract with the Commission, or his employment with such contractor.

NYO-73-293  
UC-34 Physics

PEGRAM NUCLEAR PHYSICS  
LABORATORIES

Progress Report for January 1969 through December 1969  
to the United States Atomic Energy Commission

The research reported in this document was  
made possible through the support extended  
to Columbia University by the United States  
Atomic Energy Commission, under

A. E. C. Contract AT(30-1) 73

W. W. Havens, Jr., Director

COLUMBIA UNIVERSITY  
DEPARTMENT OF PHYSICS  
NEW YORK, NEW YORK 10027

20080514418



# CONTENTS

	<u>Page</u>
I. NEUTRON PHYSICS	1
A. Nevis Synchrocyclotron Neutron Spectrometer Total and Self Indication Cross Section Measurements	1
B. Radiative Capture Cross Section Measurements in the Low keV Region	12
C. Gamma Ray Spectra from Radiative Capture in the Resonance Region	13
D. Possible Determination of the Spins of Slow Neutron Resonances of Fissile Nuclei	14
E. Variation of Fission Fragment Kinetic Energy and Yield of Long-Range Alpha Particles in the Resonance Neutron Induced Fission of $^{233}\text{U}$	17
F. Mass Distribution of Fission Fragments by Simultaneous Energy and Time-of-Flight Measurements	18
G. Comparison of Mass Distributions of Fission Fragments from Spontaneous and Induced Fission of Compound Nucleus $^{240}\text{Pu}$	19
H. Search for Delayed Fission Following Prompt Gamma Ray Emission in Fissile Nuclei	22
I. Neutron Fission Cross Section of $^{229}\text{Th}$ in the Resonance Region	23
J. Total Neutron Cross Section of $^{16}\text{O}$ at the 2.37 MeV Anti-Resonance	23
K. $\gamma$ -Radiation from (d,n) Reactions on Nuclei in the d-s Shell	31
L. $K = 1/2$ and $K = 5/2$ Components in the Ground State of $^{27}\text{Al}$	31
M. Pulse Shape Discrimination with Large Diameter Size of Liquid Scintillators	33

II.	NUCLEAR REACTIONS WITH CHARGED PARTICLES	52
A.	Van de Graaff Accelerator	52
B.	Particle-Gamma Ray Angular Correlations	60
C.	( $^3\text{He}, p$ ) Reactions on $^{24}\text{Mg}$ , $^{26}\text{Mg}$ , $^{28}\text{Si}$	63
D.	Levels in $^{28}\text{Al}$	64
E.	Proton Bremsstrahlung from Carbon	65
F.	Reduction of Background in Charged Particle Spectra	66
III.	BETA AND GAMMA SPECTROSCOPY AND ITS APPLICATION TO THE STUDY OF NUCLEAR STRUCTURE AND WEAK INTERACTION	70
A.	The Double Beta Decay Experiment	70
B.	Experiment on the Einstein-Podolsky-Rosen Paradox	73
C.	Mössbauer Effect Following Coulomb Excitation: Tungsten	79
D.	Mössbauer Effect Following Coulomb Excitation: Hafnium	81
E.	The Mössbauer Effect as a Technique of Medical Research	84
F.	Proposed Investigations Using Oriented Nuclei in $^3\text{He}/^4\text{He}$ Dilution Refrigerator	88
IV.	MUONIC ATOMS AND NUCLEAR STRUCTURE	92
A.	Charge Distribution of the Nd Isotopes	93
B.	Isotope Shifts in Tin; Comparison of Muonic and Optical Measurements	98
C.	Isotope Shifts in Barium	106
D.	Isotone Shift in Muonic X-Rays in the Tin Region	107
E.	Finite Distribution of Nuclear M1 and E2 Moments in Muonic $^{115}\text{In}$ , $^{133}\text{Cs}$ and $^{141}\text{Pr}$	114



F.	The Resonance Process and the Intensity Anomaly in Muonic $^{127}\text{I}$	117
G.	Nuclear Polarization in Deformed Nuclei	122
H.	Parameters of the Charge Distribution of Deformed Nuclei	124
I.	Muon and Pion Induced Fission of Uranium Isotopes	126
V.	NEUTRON INTERACTIONS WITH CONDENSED MATTER	135
VI.	KINETICS OF NEUTRON AND PHOTON GASES	137
A.	Moments Solution to the Time-Independent Neutron Transport Equation	137
B.	The Effect of Cross Section Fluctuations on Fast Neutron Transport	139
C.	Reconstructure of the Spatial Dependence of the Flux from the Spatial Moments	141
D.	A Discrete-Energy Discrete-Ordinate Transport Computational Technique	142
E.	Data Preparation and Analysis Computer	142
F.	Effects of Perturbations on Particle Transport in Otherwise Homogeneous Media	143
G.	High Energy Gamma Ray Production by 14 MeV Neutrons	144
H.	Response of Ge Li Detectors to Gamma Radiations	145
VII.	ELECTRONIC INSTRUMENT DEVELOPMENT	148
A.	Time Analyzer	148
B.	262,000 Channel Time-of-Flight Analyzer	171
C.	PHA Interface	180
D.	256 Channel ADC Interface	184
E.	SEL Card Reader and Line Printer Interfaces	184

F.	Incremental Plotter Control	193
G.	Card Reader and Control	196
H.	Single Channel Analyzer	199
I.	A Time Pick-Off Circuit for the Van de Graaff Accelerator	204
APPENDICES		211
A.	Journal Publications	211
B.	Papers Presented at Meetings	213
C.	Dissertations	215



## I. NEUTRON PHYSICS

### A. Nevis Synchrocyclotron Neutron Spectrometer - Total and Self Indication Cross Section Measurements - H. Camarda G. Hacken, F. Rahn, H. I. Liou, S. Wynchank, M. Slagowitz, W. W. Havens, Jr. and J. Rainwater

#### 1. Analysis of Results

The neutron spectrometer run in 1968 using an EMR6050 on-line computer data acquisition system to provide 8192 histogram channels resulted in an unusually large amount of high quality data. Most of the resonances observed in  $^{86,87,88}\text{Sr}$ ,  $^{151,153}\text{Eu}$ ,  $^{152,154}\text{Sm}$ ,  $^{154,158}\text{Gd}$  and  $^{177}\text{Hf}$  have not previously been reported. Separate isotopes of  $^{235}\text{U}$ ,  $^{115}\text{In}$ ,  $^{63}\text{Cu}$ ,  $^{142,143,144,145,146,148}\text{Nd}$ ,  $^{160,167,168,170}\text{Er}$ ,  $^{171,172,173}\text{Yb}$ ,  $^{174,176}\text{Yb}$ ,  $^{139}\text{La}$ ,  $^{182,184,186}\text{W}$  were investigated. Natural Na, Al, Fe, Cu, Co, Mn, Ta, La, Pr, Nd, In, Er, Yb were also studied.

In the past year much of the final analysis of this data has been completed. An improved data acquisition system using the faster EMR6130 computer has been developed. Complete reports on the analysis and results of the investigations will be given in a series of papers. A brief summary and some illustrative results are given below.

In most cases the use of smaller separated isotope sample area (1 1/4" x 5") allowing a greater thickness extended the energy range which could be investigated. The thicker samples improved the detection of small resonances.

Analysis of transmission and self indication measurements for  $^{86,87,88}\text{Sr}$  have been completed covering the energy range from 1 eV to > 20 keV. The useful energy range is several times larger than

has been previously reported for these nuclei. The distributions of level spacings and neutron widths along with the correlation of various parameters have been presented.<sup>(1)</sup>

Levels have been identified and  $g \Gamma n$ 's extracted: 24 levels from 588 eV to 23087 eV in  $^{86}\text{Sr}$ , 37 levels from 3.53 eV to 9974 eV in  $^{87}\text{Sr}$ , and 7 levels from 12389 eV to 88329 eV in  $^{88}\text{Sr}$ .

Graphs of level number vs.  $E_n$  for  $^{86,88}\text{Sr}$  and  $\Sigma g \Gamma n^0$  for  $^{87}\text{Sr}$  are presented in Figure I.A.1. and Figure I.A.2.

The resonance energies and parameters for 90 levels in  $^{161}\text{Eu}$ , 68 levels in  $^{153}\text{Eu}$ , 29 levels in  $^{152}\text{Sm}$  and 20 levels in  $^{154}\text{Sm}$  were analyzed for the energy region up to 100 eV for  $^{151,153}\text{Eu}$ , 1500 eV for  $^{152}\text{Sm}$  and 2500 eV for  $^{154}\text{Sm}$ .

Most of the above mentioned levels had not previously been reported including two in the previously reported range up to 27 eV in  $^{151}\text{Eu}$  and 2 in the previously reported range up to 23 eV in  $^{153}\text{Eu}$ .

$\overline{\Gamma}_\gamma$  was 96 meV and 94 meV for  $^{151,153}\text{Eu}$  and 68 meV, 78 meV for  $^{152,154}\text{Sm}$ .

Table I.A.1. gives values of observed average resonance spacing,  $\overline{D}$ , s-wave strength function,  $s_0$ , and total resonance integral above .414 eV,  $I$ . The resonance integral determined from the data is compared with the resonance integral above the cadmium (0.55 w) cut off measured by others. These results have been reported

---

<sup>1</sup>F. Rahn et al., "Neutron Resonance Spectroscopy IV:  $\text{Eu}^{151}$  and  $\text{Eu}^{153}$ ," presented at the Spring 1969 Meeting of the Am. Phys. Soc., Washington, D. C. (BAPS 14, no. 4); F. Rahn et al., "Neutron Resonance Spectroscopy,  $\text{Sm}^{152,154}$ ,  $\text{Sr}^{86,87,88}$ ," presented at the Fall 1969 Meeting of the Am. Phys. Soc., Boulder, Colorado (BAPS 14, no. 12, 1235).



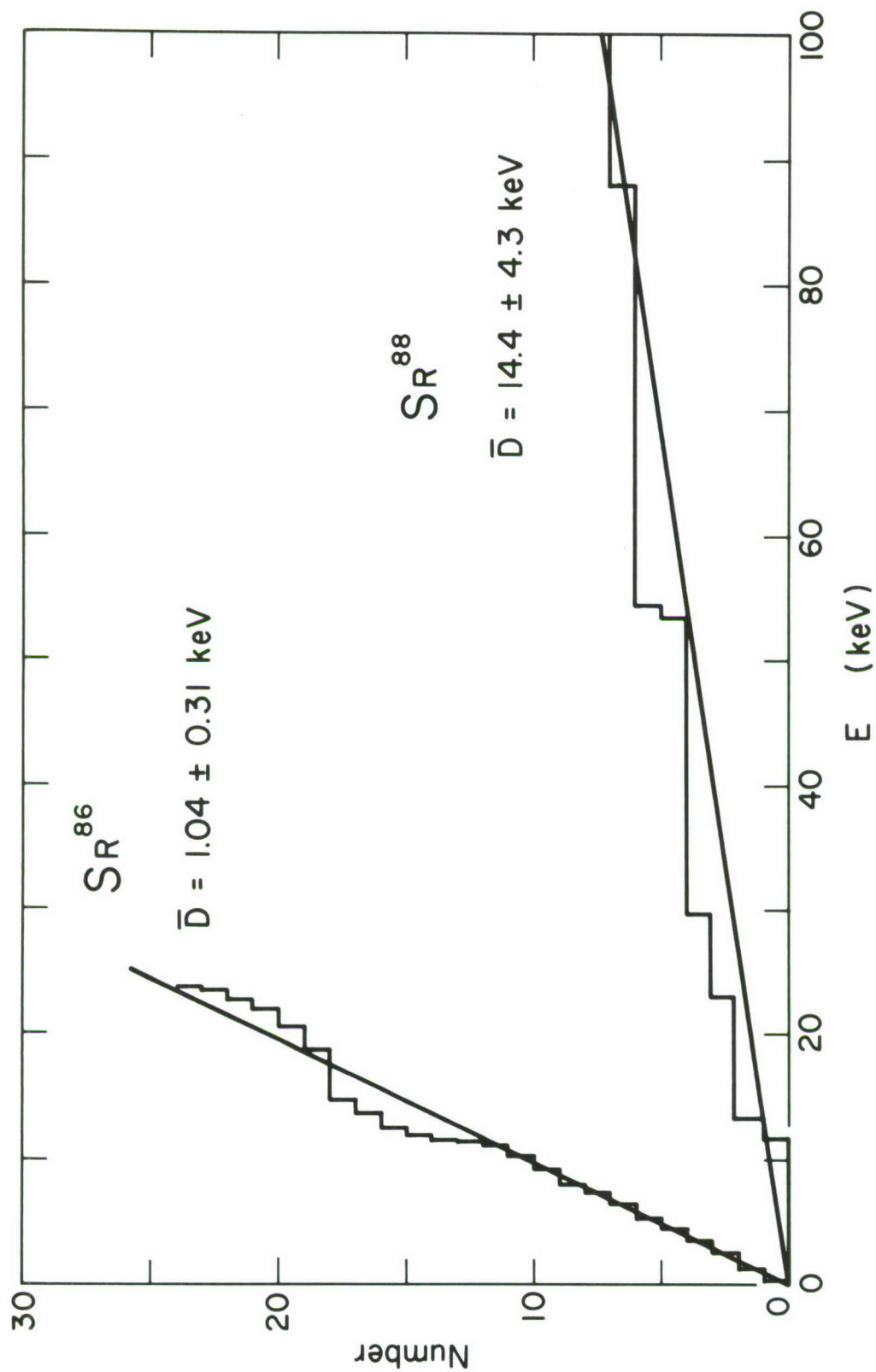


Figure I.A.1.

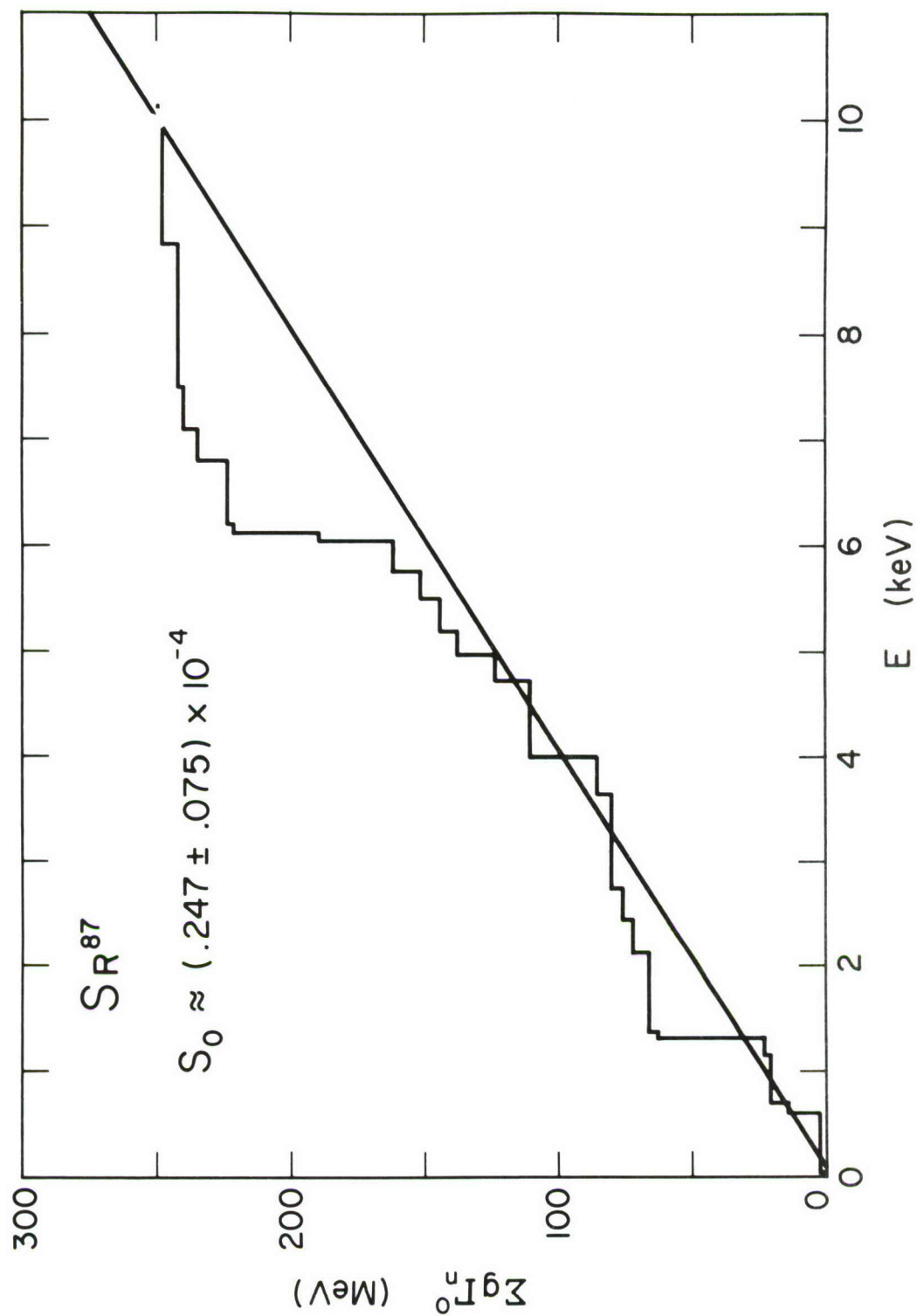


Figure I.A.2.

TABLE I.A.1.

Resonance Parameters and Capture Integrals  
for  $\text{Eu}^{151,153}$  and  $\text{Sm}^{152,154}$

Isotope	$g \Gamma_n^o$ (MeV)	D(eV)	$S_o(x10^4)$	$I_{c.414}$ calculated	$I_{c.55}$ calculated	$I_{c.55}$ measured
$\text{Eu}^{151}$	$.359 \pm .053$	$1.04 \pm .07$	$3.25 \pm .51$	$6559 \pm 687$	<b>3300</b>	$3741^{2*}$
$\text{Eu}^{153}$	$.355 \pm .059$	$1.45 \pm .12$	$2.42 \pm .47$	$2332 \pm 205$	2198	$1833^{2*}$
$\text{Sm}^{152}$	$142 \pm 37$	$52.7 \pm 7.6$	$2.72 \pm .83$	$2644 \pm 604$	2635	$3100^4, 3162^4, 2850^6$
$\text{Sm}^{154}$	$238 \pm 75$	$125 \pm 20$	$1.90 \pm .66$	$154 \pm 40$	150	-----

<sup>2\*</sup> J. Rogers, Trans. Am. Nucl. Soc. 10, 259 (1967).



at the meeting of the American Nuclear Society.<sup>(1)</sup>

Data from 1 eV to 1700 eV for  $^{171}\text{Yb}$ ,  $^{167}\text{Er}$  and to 20 keV for  $^{172,174,176}\text{Yb}$ ,  $^{166,168,170}\text{Er}$  have been analyzed yielding resonance parameters for over 1000 levels. The large number of analyzed levels, many previously unreported, allow for an improved statistical study of these nuclei.

Some of the results<sup>(2)</sup> are presented in Table I.A.2. Isotopic identification and resonance parameters<sup>(3)</sup> were determined for  $^{182,184,186}\text{W}$  over an energy range  $0.0 \lesssim E \lesssim 15$  keV. From these parameters quantities of physical interest were determined. For example, the strength function,  $S$ , and average level spacing,  $D$ , found for  $^{182,184,186}\text{W}$  are respectively:  $S^\circ = 2.43 \pm .29$ ,  $D = 68.0 \pm 4.4$  eV,  $S^\circ = 2.33 \pm .30$ ,  $D = 90.0 \pm 6.4$  eV,  $S^\circ = 2.29 \pm .32$ ,  $D = 120.0 \pm 7.2$  eV.

Previously reported resonance parameters extended to 22 keV. The new results represent a significant improvement in quality and energy range covered.

---

<sup>1</sup>F. Rahn et al., "Neutron Resonance Spectroscopy IV:  $\text{Eu}^{151}$  and  $\text{Eu}^{153}$ ," presented at the Spring 1969 Meeting of the Am. Phys. Soc., Washington, D. C. (BAPS 14, no. 4); C. Ho, F. Rahn, Measurement of the Cross Section Resonance Parameters and Integral of  $\text{Eu}-157$ ,  $\text{Eu}-153$ ,  $\text{Sm}-152$  and  $\text{Sm}-154$ , ANS, winter meeting, Dec., 1969, San Francisco.

<sup>2</sup>H. Liou et al., "Neutron Resonance Spectroscopy V: Argon and the Isotopes of Yb and Er," presented at the Spring 1969 Meeting of the Am. Phys. Soc., Washington, D. C. (BAPS, 14, no. 4, 495).

<sup>3</sup>H. Camarda et al., "Neutron Resonance Spectroscopy II:  $\text{W}^{182}$ ,  $\text{W}^{184}$ ,  $\text{W}^{186}$ , Washington APS Meeting, April, 1969 (BAPS 14.4).

TABLE I.A.2.

Gross Structure Parameters of Yb and Er Isotopes

Isotope	Examined (keV) Interval	No. of Levels	$\langle D \rangle$ (eV)	$S_0 \times 10^4$
Yb <sup>171</sup>	0.0 - 1.7	165	$7.0 \pm 0.9$	$1.83 \pm 0.28$
Yb <sup>172</sup>	0.0 - 10.7	95	$64.7 \pm 9.4$	$1.45 \pm 0.30$
Yb <sup>174</sup>	0.0 - 29.3	105	$188 \pm 21$	$1.24 \pm 0.28$
Yb <sup>176</sup>	0.0 - 26.2	77	$236 \pm 36$	$1.88 \pm 0.37$
Er <sup>166</sup>	0.0 - 9.5	152	$48.5 \pm 2.9$	$1.89 \pm 0.31$
Er <sup>167</sup>	0.0 - 1.7	263	$4.2 \pm 0.4$	$2.07 \pm 0.29$
Er <sup>168</sup>	0.0 - 15.0	96	$118 \pm 10$	$1.50 \pm 0.28$
Er <sup>170</sup>	0.0 - 24.0	87	$201 \pm 22$	$1.47 \pm 0.32$

Measurements were also made on natural W over the range  $21.0 \leq E \leq 82,000$  eV providing the highest quality total cross sections available.

Transmission measurements for  $^{113,115}\text{In}$  and  $^{139}\text{La}$  were made up to 89 keV and self indication measurements up to 3200 eV. The resonances analysed in natural In numbered 193 (a much larger number were observed) in the range 20-2000 eV; of these, 145 were attributed to  $^{115}\text{In}$  and 48 to  $^{113}\text{In}$ . The resonances analyzed in  $^{139}\text{La}$  numbered 56 from 701.9 eV to 10217 eV yielding<sup>(1)</sup>  $\langle D \rangle = 11.7 \pm 1.2$  eV,  $S = (.34 \pm .12) \times 10^{-4}$ .

Previous available data on  $^{175}\text{Lu}$  described only 20 resonances below 42 eV. In the present work<sup>(2)</sup> 312 resonances have been observed and their resonance parameters measured, below 5000 eV.

No previous data were available on resonances of  $^{154}\text{Gd}$  and only 18 resonances were previously known below 900 eV in  $^{158}\text{Gd}$ . Analysis of the last run has produced 40 resonances in  $^{158}\text{Gd}$  below 5000 eV and 107 resonances  $^{154}\text{Gd}$  below 3200 eV.

An R-matrix analysis system has been developed and used to study  $^{23}\text{Na}$ .<sup>(3)</sup> The system utilized the EMR 6130 computer and a

---

<sup>1</sup>G. Hacken et al. "Neutron Resonance Spectroscopy III: La,  $\text{In}^{113}$ ,  $\text{In}^{115}$ ," Washington APS meeting, April, 1969 (BAPS 14.4).

<sup>2</sup>S. Wynchank et al., "Neutron Resonance Spectroscopy I:  $\text{Hf}^{177}$ ,  $\text{Gd}^{152}$ ,  $\text{Gd}^{154}$ ,  $\text{Lu}^{175}$ ," Washington APS meeting, April, 1969 (BAPS 14.4).

<sup>3</sup>M. Slagowitz et al., "Neutron Resonance Spectroscopy VI: R-matrix Analysis of Total Neutron Cross Section Data," Washington APS meeting, April, 1969 (BAPS 14.4)



computer driven 5" display in a feed back mode. A sample result which identified the 28500 eV  $^{23}\text{Na}$  resonance with  $I = 3/2$  is presented in Figure I.A.3. This method of analysis yields resonance energy, resonance widths,  $I$ , and  $\ell$  (0 or 1).

Three Ph. D. theses using the results from the last run are being completed.

## 2. System Improvements

A great many experimental changes have been made in the system for the next run. The four 11" NaI 200 m detectors had a fairly large dead time (due to self blocking effects) at high counting rates. The 200 m system now combines ten 6" NaI detectors in addition to the four 11" ones which are gated off during high counting rates, each with its own Single Channel Analyzer. The new system decreases dead time and improves statistics at lower energies where the counting rates are low. The old time of flight system (TOF) provided 6 words of buffering with an 80 nsec dead time and a minimum channel width of 25 ns. The new TOF system<sup>(1)</sup> has 8 data quantizers (with < 40 ns dead time each) feeding 16 words of buffering with a 20 ns read in (and transfer time) and minimum channel width of 20 ns. The 6130 computer provides 16,000 timing channels as well as a 775 ns read-in time or buffer

---

<sup>1</sup>M. Slagowitz, J. Hahn, J. Rainwater, W. W. Havens, Jr., Neutron Velocity Spectrometry Data Acquisition on Analysis, Skytop Conf. on Computer Systems, March 1969; J. Hahn, L. Cucancic, C. Gillman, A. Zidon, "A 16,000 Channel, 50 MHz Time-of-Flight Analyzer for High Data Rates," IEEE Trans. on Nucl. Sci. NS-17, No. 1 (Feb., 1970).



$\text{Na}^{23}$ ,  $I=3/2$

exp. + th

2850 eV peak

$J=1$ ,  $\ell=0$

$\log \sigma$  vs  $E_{\text{ev}}$

20 eV/ch

71.64 eV

10312 eV

Figure I.A.3.



emptying (compared to  $1.9 \mu$  seconds for the 6050). The 16000 channels allow for the data acquisition in one run over a range of energies that in the past required 2 runs, thus providing more information for the same amount of cyclotron time. The histogram is broken up into 32 groups (512 channels each) with independently variable widths (20 ns, 40 ns, 80 ns, etc.) provided by a pin board matrix at the TOF. The TOF also provides a switch selectable "T = 0" thus the program no longer has to do the arithmetics to handle channel widths and "T = 0". Therefore, more data can be processed for each burst.

In the past valuable cyclotron time was wasted while the necessary histogram plots and data listings were made. The new system provides for simultaneous data acquisition and CRT display. The data from previous runs are stored on a disc and the plotting and printing out of the data can be done while data are being taken. The emphasis is on taking more useful data per unit cyclotron time.

Further improvement of the single turn deflection system has been made providing a 100 kV pulse with a rise time  $< 15$  ns, a back-up system of nearly identical characteristics and an electronic feed back system that automatically adjusts deflection delays to account for the slow drifts of the hydrogen thyatron. In the past this slow drift was monitored visually (via an oscilloscope) and corrected manually when detected.

The next run will start in the near future and will entail the study of different separated isotopes as well as a restudy of



some isotopes where improved statistics might be valuable. Some of the separated isotopes to be studied are  $^{110,112,114,116}\text{Cd}$ ,  $^{140}\text{Ce}$ ,  $^{160,161,162,163,164}\text{S}$ ,  $^{158,160}\text{Gd}$  and  $^{203,205}\text{Tl}$ .

B. Radiative Capture Cross Section Measurements in the Low keV Region - J. Arbo, C. Ho, J. Felvinci, F. Rahn, E. Melkonian, W. W. Havens, Jr., and J. Rainwater

The run at the Nevis synchrocyclotron which had been planned for summer 1969 has been rescheduled for April 1970. Preparations for this run are largely complete.

The modified three-stage Moxon-Rae detectors described in the 1968 Progress Report have been calibrated up to a gamma energy of 4 MeV. The detection efficiency vs. energy curve was found to be linear over this range. A high-energy calibration of the detectors is planned using the 7.367 MeV capture gamma line from a Pb-207 target in a thermal neutron beam at the HFBR. This measurement should reliably establish the detector efficiency curve over the entire energy region of interest.

As a result of the April 1968 test of the detector system at Nevis, extensive attention has been given to preparation of a new 35-meter neutron flight path which will provide good shielding and neutron beam definition at the detector station. The design also provides a contiguous helium path from the inside face of the cyclotron shielding wall, past the capture sample, up to the beamstop.

Samples for which capture cross section measurements will be made include Rh-103, Tm-169, Mn-55, Cs-133, Np-237 and U-238. Au-197 will be used as the reference standard. An attempt will be made to

measure  $\sigma(n,\gamma)$  of Th-232 despite the anticipated high gamma background from Th-228 decay products.

Earlier limitation of the data handling rate has been relieved by use of a new 20 nsec/channel time-of-flight buffer and the addition of a magnetic disk memory to the PDP-8 computer. The entire time-of-flight system is described in the Electronics Instrument Development part of this report.

- C. Gamma Ray Spectra from Radiative Capture in the Resonance Region - M. Derengowski, J. Felvinci, C. Ho, E. Melkonian, F. Rahn and W. W. Havens, Jr.

Equipment has been set up and tested for use in the NVS run scheduled for early 1970 at the Nevis cyclotron. The experiment involves measurement of the energies of the neutron capture gamma rays emitted by a  $^{235}\text{U}$  target, as well as the time-of-flight of the captured neutrons.

In order to take advantage of the high energy resolution of the lithium drifted germanium detector, we are using an 8192 channel ADC with a built in stabilizer (Northern Scientific NS-627) for the gamma ray measurements. The ADC is interfaced to the PDP-8 computer. A program has been written to store the contents of the 8192 channels on the Digital magnetic disc, while allowing 512 channels at a time to be displayed on the oscilloscope.

The time-of-flight of the neutrons will be measured by means of a time-of-flight analyzer and buffer system described elsewhere\*. The timing pulse from the germanium detector is obtained from a time pickoff unit placed between the charge sensitive preamp and the linear

---

\* Refer to electronics group report.

amplifier. The output of the time pickoff unit is shaped and fed into one of the inputs of the buffer system.

A block diagram of the system is shown in Figure I.C.1. As was mentioned in a previous Progress Report (NYO-72-191, p. 19) the system includes two NaI detectors for operation in a pair spectrometer mode to reduce the background and simplify the spectrum.

Because of the low counting rates expected in the individual gamma peaks, it seemed impractical to stabilize the ADC on a peak in the stored spectrum. Therefore an external precision pulser was built to provide a peak for gain stabilization. The pulser for zero stabilization is internal to the stabilizer itself. The ADC was modified to prevent storage of the external pulser pulse upon reception of a tag input provided by the pulser. Another modification was made to allow the use of the stabilizer in the ADC coincidence mode. This involved taking out a tag pulse from the zero pulser circuit in the stabilizer and using it in the external coincidence circuit.

We are now taking test runs of various targets using neutrons from plutonium beryllium sources in order to check the operation of the system during long term runs.

D. Possible Determination of the Spins of Slow Neutron Resonances of Fissile Nuclei - J. Felvinci and E. Melkonian

The measurements described in the previous Progress Report (NYO 72-227) used an NaI detector to record  $\gamma$ -rays above 3 MeV as a function of neutron time-of-flight. After further study of this preliminary experiment, it was decided that the method holds enough



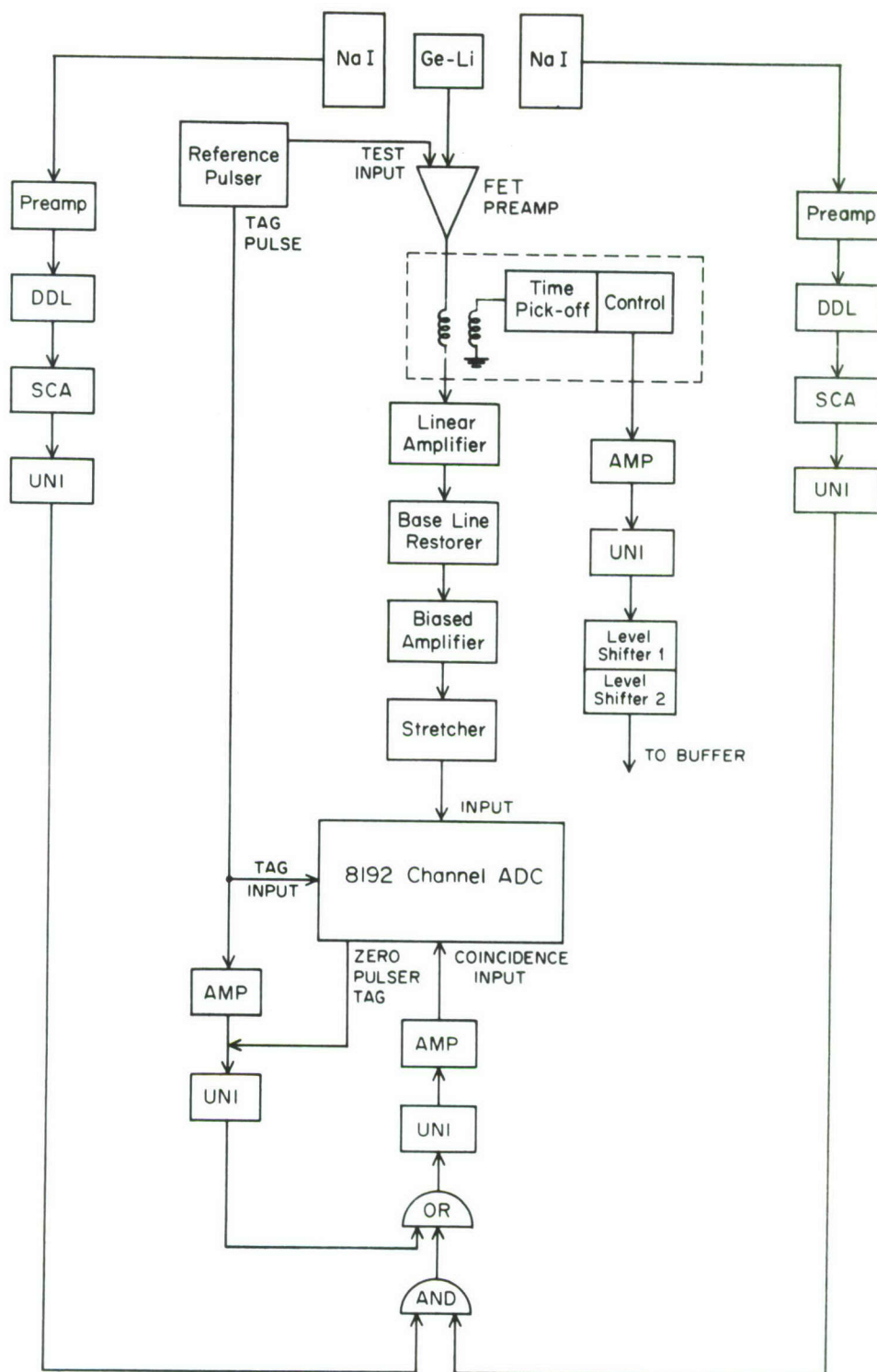


Figure I.C.1.

Na I      5-inch sodium iodide crystal  
 DDL      Double delay line amplifier  
 SCA      Single channel analyzer set on 511 keV  
 UNI      Univibrator  
 AMP      Gain - IO amplifier

promise to be included in the 1970 run, using several fissile targets ( $^{233}\text{U}$ ,  $^{235}\text{U}$ ,  $^{237}\text{Np}$ ). This time two NaI detectors will be used to allow observation of coincidences between cascade captive  $\gamma$ -rays. Great care will be taken to reduce the background, and statistics will be improved. This experiment, like the others to be performed during this run, will use the new 20 ns/channel TOF buffer built by the Pegram Electronics Group. (This system is described in the Electronics Instrument Development part of the report.) The entire system has been set up and tested in the laboratory.

It is expected that the better results to be obtained in the  $^{233}\text{U}$  measurements will enable us to assign spins to several levels and we will correlate these results with the fission fragment energy distribution. In the  $^{235}\text{U}$  experiment the many discrepancies in spin assignment between Ashgar et al.<sup>(1)</sup> and Bowman et al.<sup>(2)</sup> will hopefully be resolved. The  $^{237}\text{Np}$  spin values might give a clue to the nature of the levels excited in the subthreshold fission. The fact that in this experiment the energies of the  $\gamma$ -rays are also recorded made it possible to calculate mean energies as a function of neutron time-of-flight. The background mean energy was high due to the large amount of  $^{57}\text{Fe}$  7.76 MeV  $\gamma$ -rays from the beam stop. The mean  $\gamma$ -energies of resonances were all significantly lower than background except the 4.8, 11.5 and 10.3 eV resonances which are believed to have  $2^+$  spin.

---

<sup>1</sup>Ashgar et al., Physics Letters 26B, 664 (1968).

<sup>2</sup>Private communication.

E. Variation of Fission Fragment Kinetic Energy and Yield of Long-Range Alpha Particles in the Resonance Neutron Induced Fission of  $^{233}\text{U}$  - J. Felvinci and E. Melkonian

The analysis of the  $^{233}\text{U}$  data reported in the previous report (NYO 72-227) continued. The method of subdividing single fragment kinetic energy curve into groups was extended from four to seven groups. A statistical test (the Kolmogorov-Smirnov method) was applied at selected resonances to three different groups to ascertain whether there is significant deviation between the shape of the TOF spectrum. Definite differences were found between groups for the 22.1 eV and 22.5 eV double peak and also in the region of the 15-16 eV complex. Further significant differences between groups were evident at the low energy shoulder of the 1.78 eV resonance (there is a supposedly  $2^+$  resonance at 1.55 eV).

The fact that no appreciable difference was found in the single fragment mean kinetic energy from resonance to resonance, but the deviations were significant between different groups may indicate that the shape and not the position of the single fragment kinetic energy distribution is varying. If speculation is correct and the  $2^+$  levels have higher symmetric fission yield and wider mass distribution, this effect could cause some of the observed differences.

The preparations for the run in 1970 have been completed. We expect to measure  $^{237}\text{Np}$  subthreshold fission and compare this a.) with earlier measurements by Paya et al.<sup>(1)</sup> and b.) with the spin values obtained from the multiplicity experiment. (See Section I.D.)

---

<sup>1</sup>Paya et al., Dubna Conference, 1968, SMNF 624/68.

The method of measurement will be the same as in previous runs except we will use the new 20 ns/channel TOF buffer developed by the Pegram Electronics group. (See Section VII.B.) The events will be stored on magnetic tape event-by-event and a TOF histogram will be developed for monitoring purposes on the disk memory unit attached to the PDP-8 computer.

F. Mass Distribution of Fission Fragments by Simultaneous Energy and Time-of-Flight Measurements - M. Derengowski and E. Melkonian

Further analysis of the data subsequent to the last Progress Report (NYO-72-227) has revealed the existence of a rounding-off error in the computer calculations. The only part of the results affected by this error is the neutron number distributions at fixed mass, which had previously been reported as peaking at zero neutrons at all values of fragment mass. Upon correction of the error, we find that the peak at zero neutrons occurs only for about half the heavy masses, predominantly on the light end of the heavy mass peak. A paper covering this research has been submitted to the Physical Review. The abstract is as follows:

An experiment has been performed on the thermal neutron induced fission of  $^{235}\text{U}$ , in which the energies of complementary fission fragments and the time-of-flight of one fragment were measured. Fragment masses after neutron emission were obtained directly from this information. Pre-neutron masses and kinetic energies were deduced by means of a reflection method which simulates a double time-of-flight experiment. Subtraction of postneutron from primary



fragment masses then gave the number of neutrons emitted by single fragments in each event. Among the results presented are the distributions of the numbers of neutrons emitted by single fragments of fixed mass. This information is very difficult to obtain from other types of experiments, and there has been no previous publication of such results for any fissioning nucleus. The results also include the average number of neutrons emitted as a function of mass and total kinetic energy, as well as mass distributions in fixed kinetic energy intervals, and total kinetic energy distributions at fixed fragment masses.

G. Comparison of Mass Distributions of Fission Fragments from Spontaneous and Induced Fission of Compound Nucleus  $^{240}\text{Pu}$  - J. R. Toraskar and E. Melkonian

This experiment was performed to investigate the effects of the spin and the excitation energy of the compound nucleus on the fission process. The experiment consisted of measuring simultaneously the energies of the complimentary fission fragments and then deriving, the mass and kinetic energy distribution from these data.

A complete description of this experiment, including the experimental method, data analysis and the results has been given in a thesis entitled Mass Distributions of Fission Fragments for the Compound Nucleus  $\text{Pu}^{240}$ : Comparison between Spontaneous Fission and Fission Induced by Neutrons of Several Energies Below 1 eV by Jayashree R. Toraskar, Columbia University, 1969.

Some additional experimental work was done which further

confirmed that there was no contamination in the target used in the study of spontaneous fission of  $^{240}\text{Pu}$ .

Two papers based on the results of this experiment are now ready to be published. The titles and the abstracts follow:

1.) "Effect of  $\text{Pu}^{240}$  Compound Nucleus State on the Fission-Fragment Mass and Kinetic Energy Distributions"

Abstract:

Fission-fragment mass and kinetic energy distributions have been obtained for fission of  $^{239}\text{Pu}$  induced by neutrons filtered through beryllium and by neutrons filtered through samarium. The beryllium filter enhances the contribution of the negative energy resonance level to the fission cross-section and the samarium filter enhances the contribution of the 0.297 eV level. Surface barrier detectors were used for simultaneous measurement of both the fragment energies. Absolute fragment energies were calculated by using mass dependent pulse-height-energy relations. The average total kinetic energy of the fragments produced in the fission induced by samarium-filtered neutrons was observed to be  $0.75 \pm 0.05$  MeV greater than in the case of fission induced by beryllium-filtered neutrons. Combining this result with the results of other experiments implies  $J = 0^+$  for the negative energy level and  $J = 1^+$  for the 0.297 eV level of  $^{239}\text{Pu}$ . The two mass distributions are similar except for a difference in the symmetric fission yield. This difference again implies the same spin assignments as above. The absolute average total kinetic energies

were determined with somewhat less accuracy and are found to be  $173.0 \pm 1.5$  MeV and  $173.7 \pm 1.5$  MeV for fissions induced by beryllium-filtered and samarium-filtered neutrons respectively as directly measured, and  $175.8 \pm 1.5$  MeV and  $176.5 \pm 1.5$  MeV respectively after correction for neutron emission.

## 2.) "Spontaneous Fission of $^{240}\text{Pu}$ "

### Abstract:

Fission fragment mass and kinetic energy distributions have been obtained for the spontaneous fission of  $^{240}\text{Pu}$  and compared with those for the thermal neutron induced fission of  $^{239}\text{Pu}$ . Surface barrier detectors were used for the simultaneous measurements of both fragment energies. Absolute fragment energies were calculated by using mass dependent pulse-height-energy relations. The average total kinetic energies were measured to be  $177.25 \pm 1.56$  MeV and  $172.98 \pm 1.47$  MeV for the spontaneous and the induced fission respectively. This higher value of the total kinetic energy for the spontaneous fission is rather surprising, because in the thermal neutron induced fission of  $^{239}\text{Pu}$ , the compound nucleus  $^{240}\text{Pu}$  has about 6.3 MeV more excitation energy than in its ground state. The measured total kinetic energy and mass distributions for the spontaneous fission also appear to be significantly different in shape from those in the case of induced fission.



H. Search for Delayed Fission Following Prompt Gamma Ray Emission in Fissile Nuclei - M. Derengowski, J. Felvinci, and E. Melkonian

According to the calculations of Strutinskij,<sup>(1)</sup> the fission barrier has a secondary minimum at higher nuclear deformations. This minimum is very sensitive to the shell structure of the nucleus. Due to this secondary minimum, an isomeric fission state could be formed with relatively long half-lives ( $10^{-2}$  -  $10^{-7}$  seconds). These isomers have been observed and so were intermediate structures in the sub-threshold fission of  $^{237}\text{Np}$ ,  $^{234}\text{U}$  etc., which could be interpreted as interference effects using the same theory.

In this experiment, an attempt is being made to find correlations between the gamma-rays, emitted from the excited compound nucleus to a level corresponding to the bottom of the secondary well (2 - 3 MeV energy), and the delayed fission following it. The method to be used is to measure the times between gamma-rays and fissions with a time-to-amplitude converter in different fission resonances. We expect to see a prompt peak due to prompt fission gamma-rays, flat background from capture gammas and delayed fission gammas and a tail on the prompt peak, the slope of which would indicate the lifetime of a possible isomeric state.

Motivation for this experiment comes from the observation that in  $^{233}\text{U}$  the single fragment mean kinetic energy decreases across some of the fission resonances. This effect could be interpreted as the formation of an isomeric state with lower mean kinetic energy

---

<sup>1</sup>Strutinskij, Nuclear Physics, A95, 420 (1967).



for the fission fragments (half-life  $\sim 200$  ns,  $\sigma$  isomeric/ $\sigma$  fission 0.1 - 0.2).

Measurements presented recently at the Vienna Conference on Fission<sup>(1)</sup> show a 100 ns and a 2 ns isomeric state in  $^{233}\text{U}$ . The electronics for the search have been set up and are working with thermal neutrons from Pu-Be sources. No conclusive evidence for an isomeric state in  $^{235}\text{U}$  has been seen. Time resolution in the prompt peak is 6 ns FWHM and the background is very low. Life-times in the range of 10 - 500 ns and formation cross sections 1-10% of the fission cross section should be seen.

I. Neutron-Fission Cross Section of  $^{229}\text{Th}$  in the Resonance Region - J. Toraskar and E. Melkonian

An experiment has been planned to measure the neutron induced fission cross-section of  $^{229}\text{Th}$  in the resonance region. So far only the total neutron cross-sections of  $^{229}\text{Th}$  are available in this energy region.

The experiment will be performed at Nevis Cyclotron Laboratory. The time of flight technique will be used to measure the neutron energies. Solid state detectors will be used to detect the number of fission events and to measure the fission fragment energies. The actual run will be performed sometime in 1970.

J. Total Neutron Cross Section of  $^{16}\text{O}$  at the 2.37 MeV Anti-Resonance - J. Kalyna, I. J. Taylor, L. J. Lidofsky

1. Introduction

A minimum in the total neutron cross section of  $^{16}\text{O}$  occurs at

---

<sup>1</sup>Physics and Chemistry of Fission

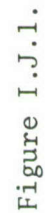
2.37 MeV. This interference dip is being measured by the transmission of neutrons through a 5 foot sample of liquid oxygen. The Van de Graaff accelerator is pulsed to produce 5 nanosecond neutron bursts via the  ${}^7\text{Li}(p,n){}^7\text{Be}$  reaction. An eight inch diameter by one inch thick liquid scintillator (NE213) together with a pulse shape discriminator, comprises the neutron time-of-flight system.

## 2. Experimental Assembly

The cryostat is a stainless steel cylinder, surrounded by a vacuum and a radiation shield kept at liquid nitrogen temperature. Figure I. J1. (reprinted with permission from Sulfran Cryogenics, Inc.) shows the design which made all walls as thin as possible to minimize inscattering. The entire assembly is held rigidly in place by stainless steel wire ropes. All peripheral equipment; the liquid oxygen and nitrogen supply tanks, and electronics is kept far enough away from the sample for negligible inscattering. A proportional gas counter filled with  ${}^3\text{He}$  and surrounded by paraffin was placed at an angle of  $120^\circ$  to the incident beam. This counter provided a monitor on the neutron yield.

Above the analyzing magnet a pick-off cylinder was inserted in the beam line to provide a timing signal for the time-of-flight system.

Neutrons are detected by observing proton recoils in a liquid organic scintillator. A 5" diameter (58AVP Amperex) photomultiplier views the 8" diameter scintillator via an optically coupled (conical shaped) lucite light pipe. Signals are derived from the anode and





dynode. The anode signal is a short duration fast pulse which is used for timing purposes and the dynode pulse is a slow pulse which is properly shaped for neutron-gamma pulse shape discrimination (this system is described in another section of this annual report).

A block diagram of the electronics arrangement is shown in Figure I.J.2. Multi-Channel Analyzer #1 monitors the neutron gamma pulse shape discrimination. Multi-Channel Analyzer #2 records the neutron, time of flight spectrum, whereas #3 shows the entire time of flight spectrum; neutrons and gammas.

### 3. Targets

Various targets and target backings were tried as the neutron source. LiH and LiF were evaporated on Ta, Mo, Pt and W backings. Thresholds for the  $\text{Li(p,n)Be}$  reaction were run to measure the target thickness and to determine long term stability. Backings also were tested for intensity of (p,n) yields and relative gamma ray background. Carbon buildup was observed, but its effect was reduced by using a copper tube at liquid nitrogen temperature in front of the target. Using the criteria of, ease of uniform evaporation, stability during long use and relative low background yield, LiH on W backing was chosen as most suitable at this particular energy.

### 4. Time of Flight

Terminal pulsing of the Van de Graaff accelerator is monitored by a pick-off cylinder above the analyzing magnetic (description of cylinder, and related circuits is in another section of this annual

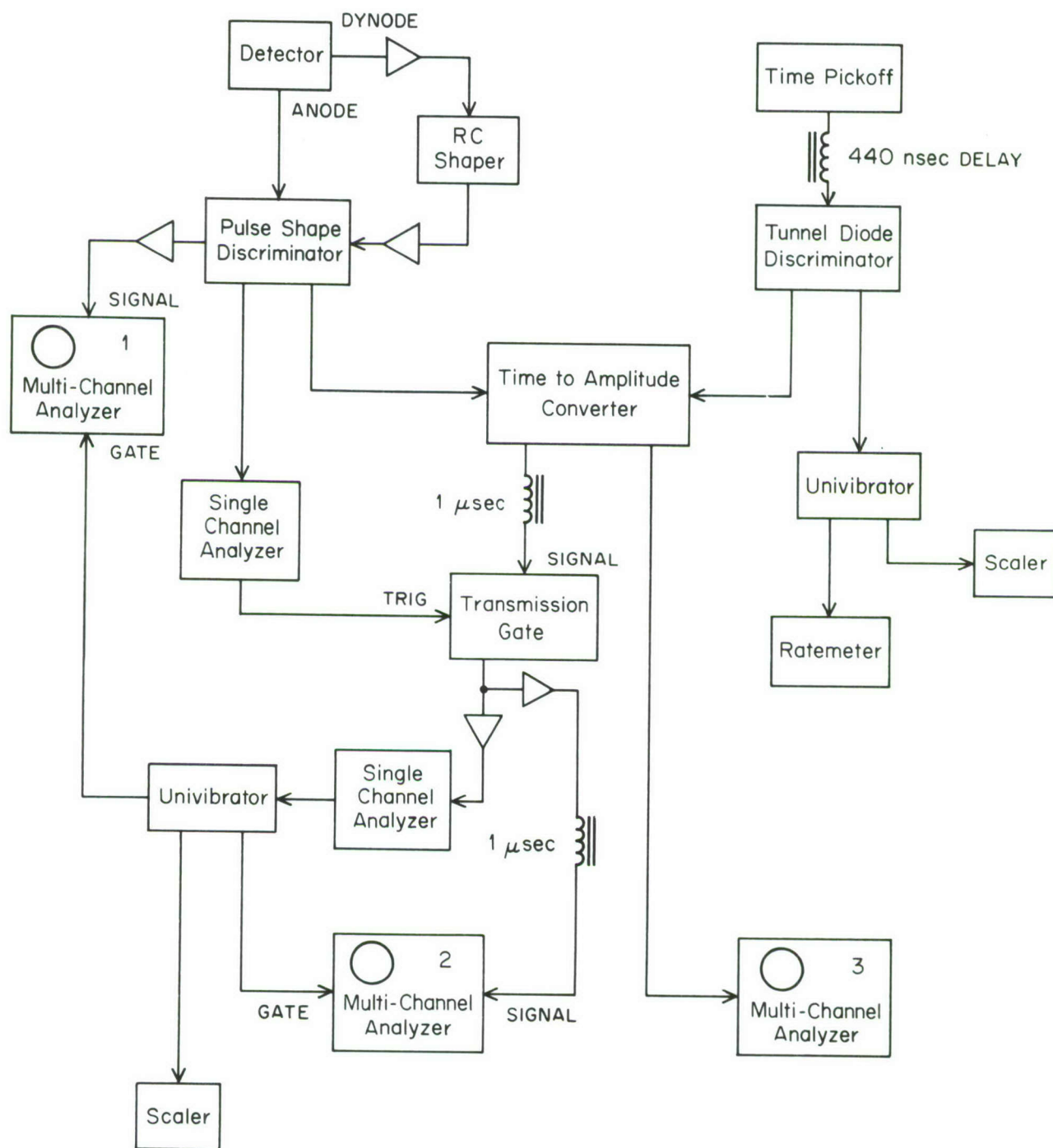


Figure I.J.2.

report). A type R561B sampling oscilloscope displays the voltage induced across a Resistor connected to the Pick-off cylinder. This pulse is bipolar and can be seen in Figure I.J.3. The terminal is tuned for minimum width of pulsed beam and the beam burst is monitored throughout the entire run.

A fast trigger pulse is generated by the zero crossover of the bipolar pulse and is used as the start pulse in a time to amplitude converter. The zero crossover is independent of pulse height, hence there is minimum time walk, and no dependence on beam intensity fluctuations.

A typical neutron time-of-flight spectrum for a 2.3 meter flight path and for 2.3 MeV neutrons produced from the  ${}^7\text{Li}(p,n){}^7\text{Be}$  reaction is shown in Figure I.J.4. As can be seen the primary neutrons are clearly resolved from the second group of neutrons which are 430 keV lower in energy, and produced from the reaction leading to the first excited state of  ${}^7\text{Be}$ .

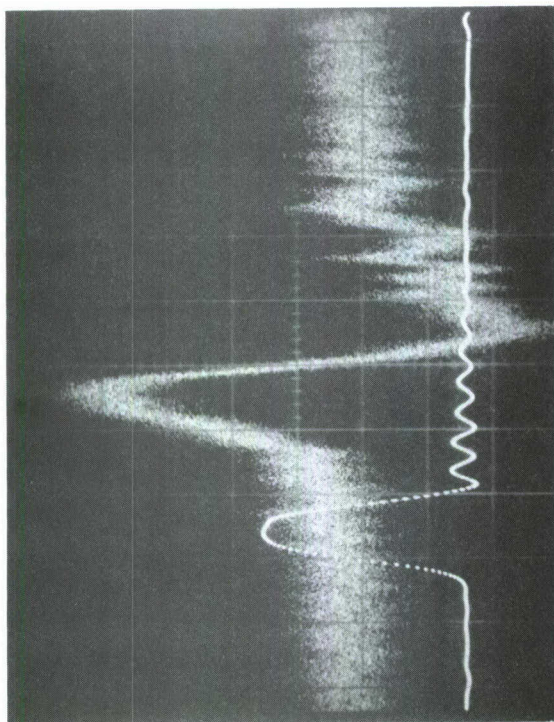
#### 5. Sample Analysis

Samples of the oxygen are now being analyzed by mass spectroscopic methods to accurately determine traces of Argon,  $\text{CO}_2$  and  ${}^{17}\text{O}$  and  ${}^{18}\text{O}$ . Using published total neutron cross sections for these elements, corrections to the measured transmission will be made to obtain as much precision as possible in the final measurement.

#### 6. Data Analysis

Data are now being taken in a series of six independent runs to check for reproducibility of results. Target thickness will





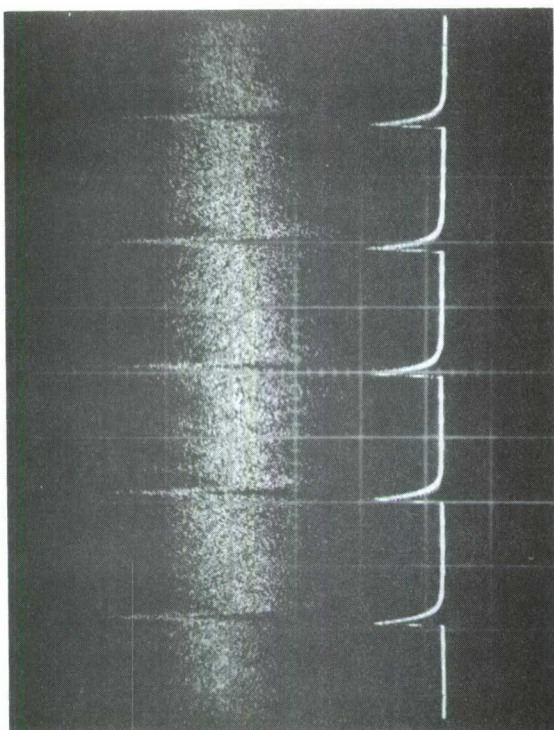
Upper Trace: Linear Signal

time scale 5 nanosec per cm

vertical scale 5 m volts per cm

Lower Trace: Time Pick-off Trigger Signal

vertical scale 200 m volts per cm



Upper Trace: Linear Signal

time scale 100 nanosec per cm

vertical scale 5 mv per cm

Lower Trace: Time Pick-off Trigger Signal

vertical scale 200 m volts per cm

Fig. I.J.3. Sampling Oscilloscope Displays of Beam Pulsing

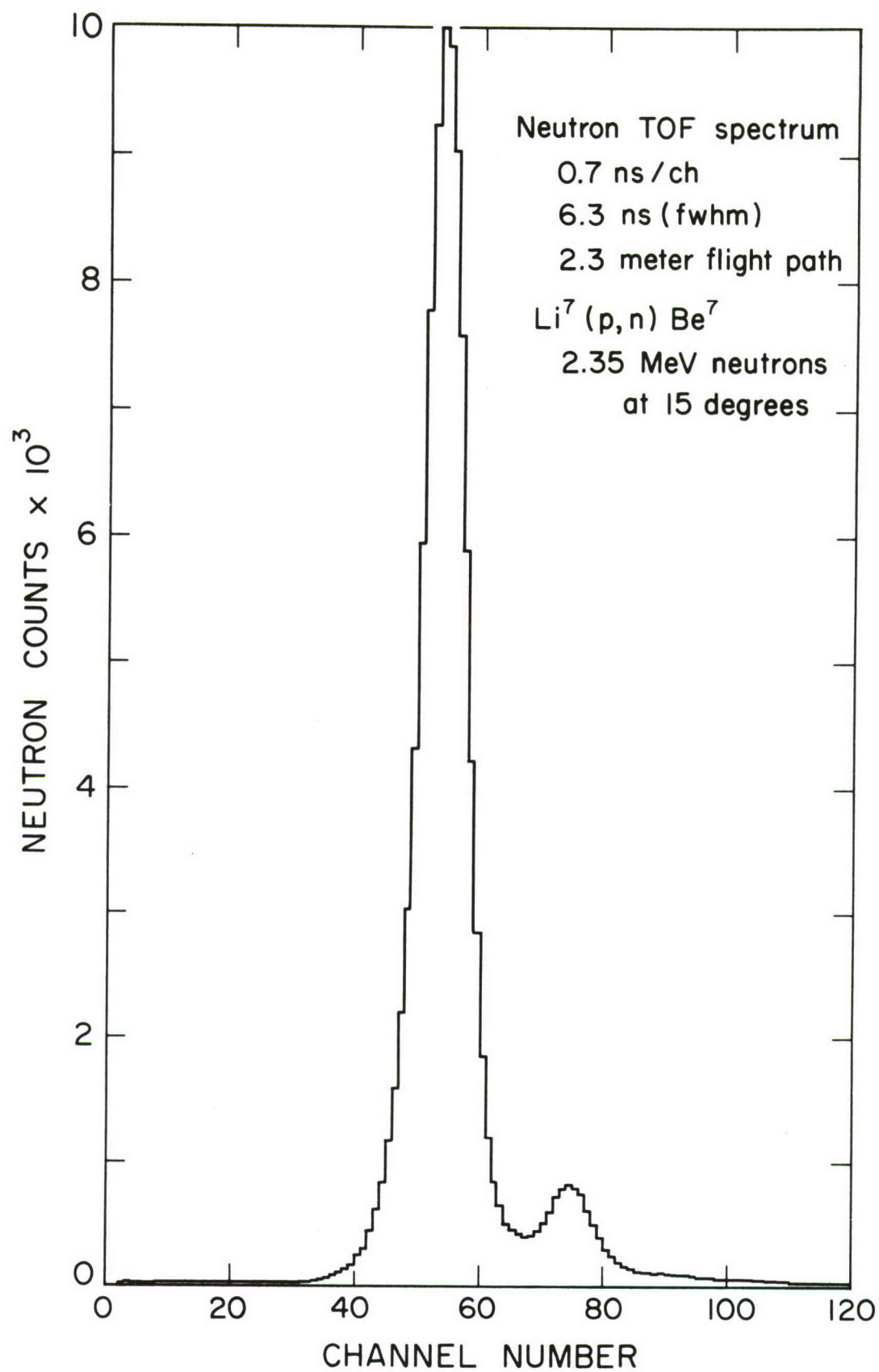


Figure I.J.4.

be made progressively smaller during each and every run and hopefully the final results can then be made independent of target thickness.

In Figure I.J.5. we present preliminary data which was the measurement of neutron yield versus the NuMar frequency. Background and inscattering corrections have not been made.

Following the series of intensive runs the data will be carefully analyzed and corrected for inscattering (using a monte carlo computer code MONCAR, described in the 1967 and 1968 annual reports).

K.  $\gamma$ -radiation from (d,n) Reactions on Nuclei in the d-s Shell - B. T. Lawergren, I. J. Taylor and M. Nessim

This project has been concluded and the results will be published in the Physical Review

L.  $K = 1/2$  and  $K = 5/2$  Components in the Ground State of  $^{27}\text{Al}$  - B. T. Lawergren (with G. C. Neilson and J. L. Honsaker, Univ. of Alberta)

The  $^{25}\text{Mg}(^3\text{He},n)^{27}\text{Si}$  and the  $^{27}\text{Al}(^3\text{He},n)^{29}\text{P}$  reactions were studied using the 6 MeV Van de Graaff and associated time-of-flight system at the University of Alberta. There are strong stripping transitions to the ground state of  $^{27}\text{Si}$  and to the second excited state of  $^{29}\text{P}$  with unambiguous  $L = 0$ . Both transitions are allowed to have  $L = 0$  by conservation of angular momentum but, if the deformed collective model is applicable in this mass region, the K-number (i.e., the particle angular momentum projected on the z-axis of the body-fixed frame of reference) should also be conserved. These stripping reactions can only transfer a proton pair with  $K = 0$ .



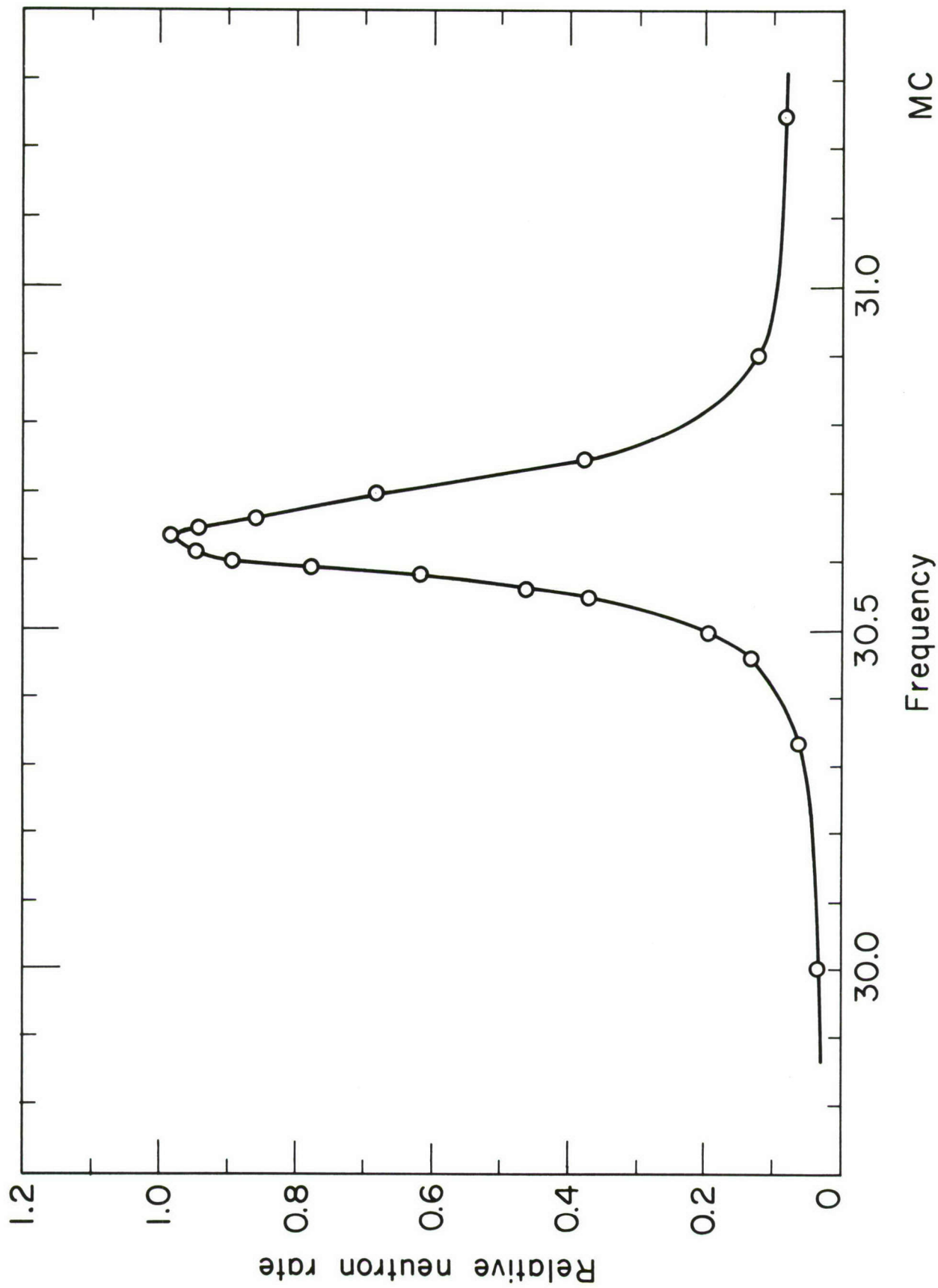


Fig. I.J.5.

The  $^{25}\text{Mg}$  ground state has  $K = 5/2$  and the second excited state of  $^{29}\text{P}$  has  $K = 1/2$ . The two  $L = 0$  transitions therefore imply that the ground states of the mirror pair  $^{27}\text{Al}$ - $^{27}\text{Si}$  have large  $K = 1/2$  and  $K = 5/2$  admixtures. This result invalidates Nilsson model calculations on  $^{27}\text{Al}$  which only accomodate orbits with  $K = 5/2$  in the ground state.

M. Pulse Shape Discrimination: An Investigation of n- $\gamma$  Discrimination with Large Diameter Size of Liquid Scintillators - J. Kalyna and I. J. Taylor

1. Introduction

In neutron time of flight work it is often necessary to discriminate against background gamma rays. This is especially true for the measurement of neutron cross sections where backgrounds must be subtracted and ideally should therefore be made very low.

The technique of n- $\gamma$  discrimination in organic scintillators depends on utilizing the differences in the decay times of the slow component of the light flash produced by different ionizing particles (electrons vs. recoil protons). Such pulse shape discrimination (p.s.d.) has been mainly limited, in the literature, to systems using scintillators whose diameters are small in comparison to the 8 inch diameter NE213 and NE 218 (Nuclear Enterprises) liquid scintillators typically required for fast neutron time of flight work on the Van de Graaff accelerator and as used in the total neutron cross section measurement of  $^{16}\text{O}$ , mentioned elsewhere in this report.

A pulse shape discrimination circuit (described later) has been constructed to enable optimum n- $\gamma$  discrimination using the double

differentiation and crossover detection technique<sup>(1)</sup> and to permit direct comparison of p.s.d performance of various scintillator and detector arrangements.

Using this circuit it was evident that p.s.d. performance worsened with the use of larger diameter scintillators, and an attempt has been made to find a satisfactory explanation for this effect and whether or not it can be corrected. This has led to the investigation of the transit time properties of several 5 inch diameter photo-multipliers.

## 2. Pulse Shape Discriminator Circuit

A block diagram of the circuit is shown in Figure I.M.1. The anode pulses were arranged to arrive in time coincidence or to be slightly delayed with respect to the bi-polar dynode pulses, which have components of different crossover times. The fast anode pulse branches into three discriminators which are used for "anti-walk" timing. The noise level discriminator (A) is set to operate at just above noise level and generates a short duration (5 to 10 nanoseconds) output pulse which is internally cable delayed by 30 nanoseconds. The lower level discriminator (B) generates a longer pulse (approximately 30 nanoseconds) delayed internally by approximately 15 nanoseconds, and the upper level discriminator (c) similarly generates a longer pulse but of opposite polarity and without delay.

The discriminator outputs are mixed at the  $A \cdot B \cdot \bar{C}$  discriminator (which generates an output on addition of A and B signals but which is inhibited during an output from the C discriminator). The  $A \cdot B \cdot \bar{C}$  discriminator output is thus generated, in effect, from the noise level

---

<sup>1</sup>Forte, Konsta and Maranzana, Proc. Nucl. Energy Conf. (Belgrade) 2, 277 (1961).



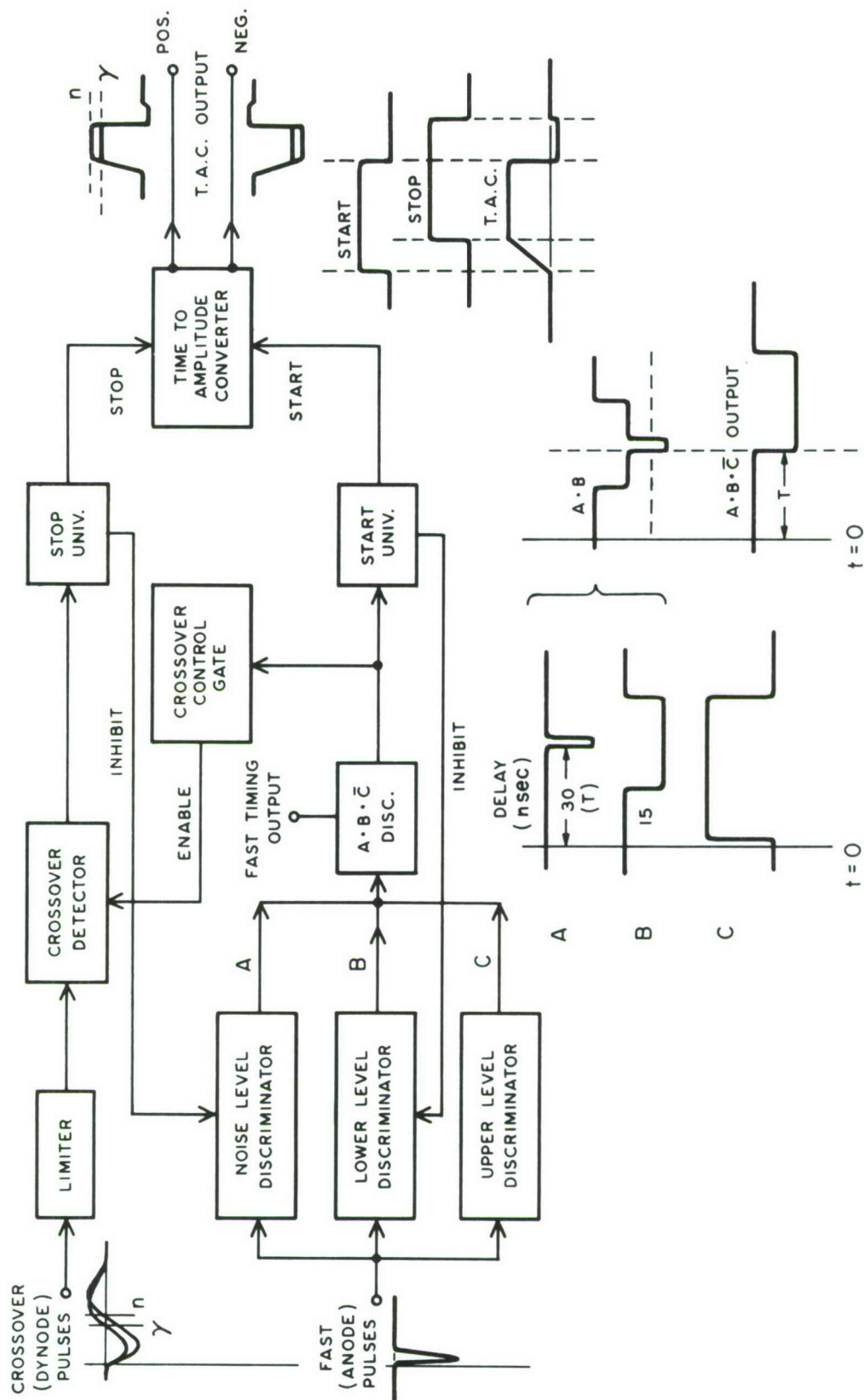


Figure I.M.1. BLOCK DIAGRAM OF PULSE SHAPE DISCRIMINATOR CIRCUIT

discriminator delayed by time  $T$  (30 nanoseconds). Timing from the noise level region in this manner reduced time walk dependence on pulse amplitude, and this type of circuit has been used for several years in the Pegram Nuclear Physics Laboratories as an "anti-walk" leading edge timing discriminator. The extension of this circuit to incorporate an anti-coincidence upper level discriminator is particularly useful for the system of  $n$ - $\gamma$  discrimination, the upper level discriminator being used to reject large pulses and thus eliminate many of the events in the scintillator due to gamma rays before the crossover timing separation is applied. The lower level discriminator is also useful in setting a threshold for neutron detection in the scintillator.

The coincidence discriminator output is used to generate a START pulse from a univibrator and to operate a crossover control gate which applies current to ENABLE the operation of a crossover detector. The coincidence discriminator also provides an output for external timing uses. The crossover detector produces an output timed from the crossover of the input bipolar pulse which is used to produce a STOP pulse from a univibrator. The START and STOP univibrator pulses are applied to a time to amplitude converter (T.A.C.) which gives a separation of crossover times in terms of pulse height. Outputs from the START and STOP univibrators are used to INHIBIT the input discriminators for the duration of the time-to-amplitude conversion, and allow the circuit to function at high data rates.

### 3. Circuit Operation

The "anti-walk" discriminators, crossover control gate and crossover detector are shown in Figure I.M.2., and the START and STOP univibrators and T.A.C. sections are shown in Figure I.M.3.

The negative anode pulse is terminated in the characteristic cable impedance (120 ohm 63/U) at the input of a back to back diode limiter in the base circuit of transistor  $Q_6$  (Figure I.M.2.). The limiter prevents overloading of the subsequent tunnel diode section (TD1) of the noise level discriminator. Emitter follower  $Q_6$  drives 30 nanoseconds of delay cable (RG 174/U) impedance terminated in the base of transistor  $Q_7$  which provides a current pulse to tunnel diode TD1. The standing current in TD1 is adjusted by multiturn potentiometer VR1, which is the noise level discriminator control. The tunnel diode TD1 is used as a univibrator in the configuration described by Whetstone<sup>(1)</sup> where the load line is set by the characteristics of diode D2 and the pulse width is determined by the series inductance. A standard pulse is generated by a second, similar, tunnel diode stage (TD2).

The anode pulse also branches to emitter follower  $Q_9$ , which provides an inspection output (TP2), and to transistor  $Q_{10}$ . Transistor  $Q_{10}$  drives a 15 nanosecond delay cable, terminated to prevent reflections, and a current pulse is presented through  $Q_{11}$  to tunnel diode TD3 whose standing bias current is adjusted by multi-turn trimmer potentiometer VR2 comprising the lower level discriminator control. Tunnel

---

<sup>1</sup>Whetstone, Rev. Sci. Instr. 34, 412 (1963).







diodes TD3 and TD4 are used as univibrators in similar manner to TD1 and TD2. Transistor  $Q_{10}$  is also used to invert the input signal and, via emitter follower  $Q_{13}$  and transistor  $Q_{14}$ , drive a similar tunnel diode arrangement TD5, TD6 comprising the upper level (rejection) discriminator, controlled by potentiometer VR3.

Transistor  $Q_8$ ,  $Q_{12}$  and  $Q_{15}$  enable high impedance mixing of the A, B and C discriminator outputs at tunnel diode TD7. The standing bias current in TD7 is adjusted, via internal potentiometer VR4, such that TD7 switches only on A·B coincidence in the absence of an output from the upper level (reject) discriminator. The width of the coincidence discriminator output pulse is determined by the series inductance (15 $\mu$ H). Test points TP3, TP4 and TP5 allow inspection of the operation of the input discriminators.

The transistor switching pair  $Q_{16}$ ,  $Q_{17}$  (of which  $Q_{17}$  is normally ON) responds to the triggering of TD7. The resulting negative-going pulse from the collector of  $Q_{17}$  is used to operate the START univibrator (described later) and also to operate transistor switching pair  $Q_{18}$ ,  $Q_{19}$  which provides circuit isolation for a discriminator output (a negative 10 mA pulse with respect to ground at the collector of  $Q_{19}$ ). This signal is used for external timing purposes, and in particular as the STOP pulse of a time to amplitude converter used in neutron time-of-flight measurements. This ensures 1:1 correspondence of time-of-flight events with the p.s.d. processing, which is used to gate the time-of-flight spectrum.

The positive signal at the collector of  $Q_{16}$  is used to operate the crossover control gate formed by the transistor pair  $Q_{20}$ ,  $Q_{21}$  used



as a monostable multivibrator. The transistor  $Q_{21}$  (normally ON) provides approximately 12 mA of reverse bias current to tunnel diode TD8. This current is thus removed for a time period determined by the cross coupling time constant in the base of  $Q_{21}$ , chosen to adequately cover the duration of the input bipolar dynode pulse. The 200 pf. capacitor at the collector of  $Q_{21}$  reduces transient fluctuations as  $Q_{21}$  cuts off, and the series resistor isolates this capacitance from TD8.

A forward biasing standing current is supplied to TD8 via  $Q_{22}$  referenced to temperature compensated zener diodes, and fine control of this current is effected by a precision multiturn potentiometer VR5 which constitutes the front panel crossover level adjustment. The current through  $Q_{22}$  is adjusted to set TD8 at its switching peak on removal of the reverse bias (from  $Q_{21}$ ). At this time the negative part of the dynode pulse is present at TD8, and triggering of TD8 occurs at the subsequent crossover of the bi-polar dynode pulse.

The dynode pulse is amplitude limited at the input to transistor  $Q_1$  by a back to back diode limiter which, however, preserves the crossover characteristics. The emitter follower  $Q_1$  feeds the signal to TD8 via grounded base transistor  $Q_3$ . The emitter follower  $Q_2$  is used to provide an output test point (TP1) for inspection of the crossover signal. Tunnel diode TD8 is thus triggered at the crossover and is reset when the reverse bias current is restored through transistor  $Q_{21}$ .

The transistor pair  $Q_4$ ,  $Q_5$  (where  $Q_4$  is normally OFF) responds

to the switching and reset of TD8. A crossover event output signal is taken from the collector of  $Q_5$  and the complementary negative pulse at  $Q_4$  is used to operate the STOP univibrator of the circuit. The START univibrator is thus operated from the coincidence fast timing discriminator and the STOP univibrator from the detection of crossover.

The START univibrator (Figure I.M.3.) is comprised of emitter follower stage  $Q_{32}$  and transistor pair  $Q_{33}$ ,  $Q_{34}$  where  $Q_{34}$  is normally conducting. The negative-going input to  $Q_{32}$  switches OFF transistor  $Q_{34}$  for a period determined by the cross-coupling time constant and which is adjusted by VR6 to be approximately 2 1/2 microseconds.

Transistor  $Q_{37}$  provides D. C. level shifting and acts as an isolating buffer stage for inspection of the START univibrator at TP7 and for operation of inhibit gate  $Q_{38}$  which is turned ON. The transistor  $Q_{38}$  then short circuits the standing bias current of tunnel diode TD2 (Inhibit line X) and hence blanks out the operation of the noise level discriminator for the duration of the START univibrator.

Transistor pair  $Q_{35}$ ,  $Q_{36}$  provides level shifting, and  $Q_{36}$  (normally OFF) is forced into saturation for the duration of the START univibrator pulse so the  $Q_{39}$  (normally ON) is turned OFF. Transistors  $Q_{36}$  and  $Q_{39}$  are type 2N 709 for fast recovery from saturation.

The STOP univibrator similarly comprises emitter follower  $Q_{23}$  and transistor pair  $Q_{24}$ ,  $Q_{25}$ . The duration of the STOP pulse is controlled by VR7 and set to be approximately 3 1/2 microseconds (i.e., of longer duration than the START pulse plus the time for crossover detection, which is approximately 350 nanoseconds). The

transistor pair  $Q_{26}$ ,  $Q_{27}$  provides D. C. level shifting and isolation through  $Q_{27}$ , for inspection of the STOP univibrator at TP6, and also operates control Gate  $Q_{28}$  which is turned ON and short circuits the standing bias current of tunnel diode TD4 (Inhibit line Y) to blank out the lower-level discriminator for the duration of the STOP univibrator pulse. Together with the previously mentioned inhibit of TD2 by the START univibrator, it is seen that the coincidence discriminator is inhibited for the complete duration of time-to-amplitude conversion. This allows the circuit to process at high input rates.

The T.A.C. circuit is of a type used extensively in the Pegram Laboratories for several years. The transistor  $Q_{31}$  is used as a current source for transistors  $Q_{29}$ ,  $Q_{30}$  and is referenced to temperature compensated zener diode IN823. Transistors  $Q_{29}$ ,  $Q_{30}$ , where  $Q_{29}$  is normally ON, form a fast switching pair. As previously mentioned, transistor  $Q_{36}$  is held in saturation for the duration of the START univibrator and  $Q_{39}$  is turned OFF so that current from  $Q_{31}$  charges capacitor C linearly, through  $Q_{29}$ . On arrival of the STOP pulse from  $Q_{26}$ , transistor  $Q_{29}$  is turned OFF and the charging of capacitor C is stopped. The capacitor remains charged until removal of the START pulse at which time  $Q_{39}$  returns to normal conduction and the capacitor discharges rapidly. Current is subsequently restored to  $Q_{29}$  on removal of the STOP pulse.

The field effect transistor  $Q_{40}$  is used to present a high impedance to capacitor C during the charging period. Emitter followers  $Q_{41}$ ,  $Q_{42}$  are used as stages for the positive output of the time to



to amplitude conversion. The inverting stage  $Q_{43}$  and emitter follower  $Q_{44}$  are used to provide a complementary (negative going) output.

#### 4. Experimental Arrangement

Figure I.M.4a shows the experimental arrangement using the p.s.d. circuit. The dynode (slow) pulse is first-differentiated at a pre-amplifier stage inside the photomultiplier "head," and second-differentiated by the external CR circuit placed between buffer stages. Differentiation time constants were chosen in accordance with the calculations of Roush, Wilson and Hornyak<sup>(1)</sup> and the bi-polar pulses entering the p.s.d. circuit have components of differing crossover times.

The ability of the p.s.d. system to provide well defined and separated peaks is generally expressed in terms of a figure of merit  $M$  (after Reid and Hummel) defined as the ratio of  $n$ - $\gamma$  peak separation to the sum of peak widths (FWHM). Figure I.M.4b. shows the  $n$ - $\gamma$  discrimination for 8 inch and 4 inch diameter liquid scintillators (NE2.3) exposed to 2.3 MeV neutrons and a background source of gamma rays. The 8 inch scintillator had an  $M$ -value of 0.81 compared to a value of 1.43 for the 4 inch diameter sample. Figure I.M.4c. shows the results of a comparison between the two sizes of scintillator over a wide energy range using a Pu-Be neutron source. The figure of merit ( $M$ ) is plotted against lower discriminator setting (L.D.) of the p.s.d. circuit, the L.D. setting of 1.0 referring

---

<sup>1</sup>Roush, Wilson and Hornyak, Nucl. Instr. and Meth. 31, 112 (1964).

<sup>2</sup>Reid and Hummel, Canad. Nucl. Tech. (1966).

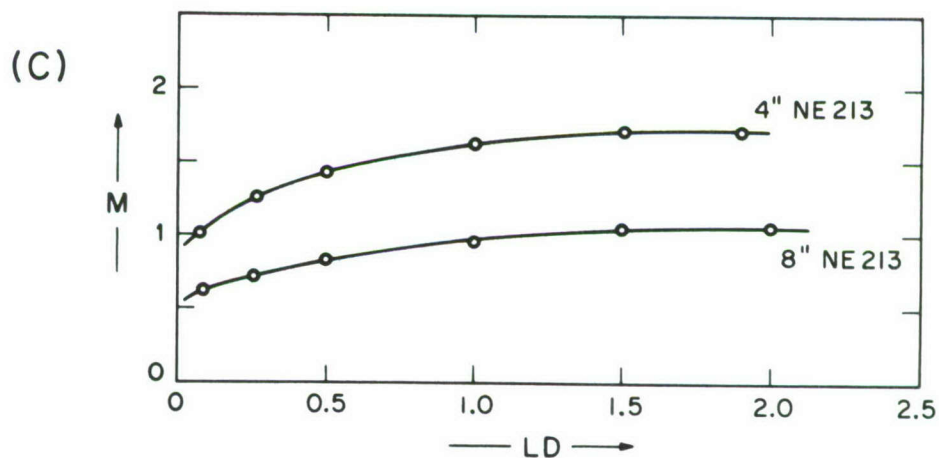
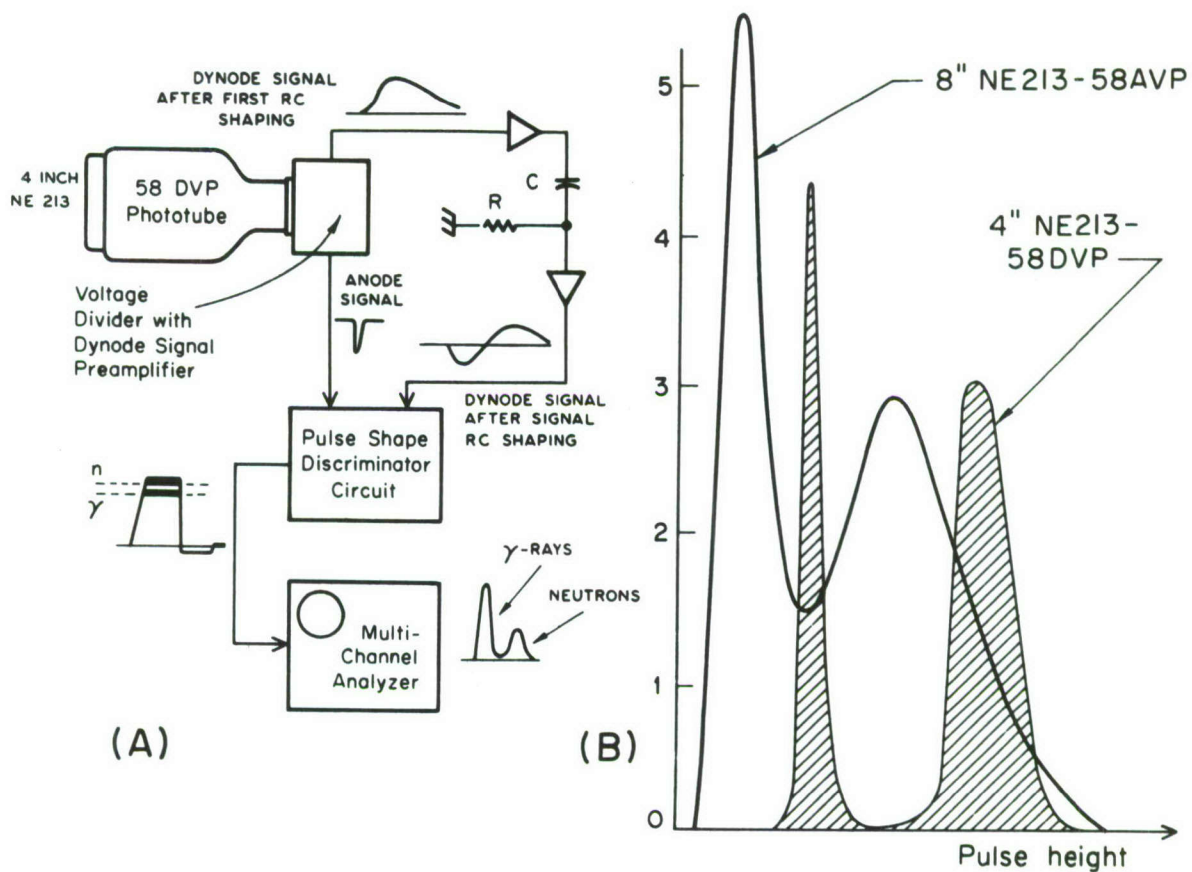


Figure I.M.4.

to maximum pulse height produced with a  $^{60}\text{Co}$  gamma ray source (1.1 MeV Compton scattered). The p.s.d. performance is seen to be markedly worse for the larger scintillator in the region from 100 keV up to 2 MeV electron energy pulse height equivalent.

Wakuta et al.,<sup>(1)</sup> using a crossover type p.s.d. system, have suggested that the poor p.s.d. results obtained with 5 inch diameter scintillators (and 5 inch phototube) were due to differences in optical path lengths and self absorption effects for larger scintillators. However, the time differences involved in multiple light reflections in the usual type of coupling system are negligible in comparison with the crossover time separation and could not drastically affect the time distribution of the light pulse quanta. We have also rejected self absorption effects as a major contributor to p.s.d. smearing.<sup>†</sup> Not only are the solute emission bands chosen to be distant from solvent absorption bands in the liquid scintillators but wave-length shifters are also added, which tend to suppress primary solvent absorption. In addition we have verified such an effect to be negligible by the use of sectorized light pipes which cut out transverse light paths and minimized variations in optical path lengths for different points on the scintillator. Such light adaptors had little effect on the p.s.d. performance. It should also be noted that, unlike n- $\gamma$  discrimination

---

<sup>1</sup>Wakuta et al. Nucl. Instr. and Meth. 71, 133 (1969).

<sup>†</sup>We are here referring to larger size in terms of increased diameters of relatively thin (1") samples, as used in fast timing applications. There are absorption effects when using larger bulk (thickness) of scintillator material. These effects, which we find to have interesting consequences with regard to photomultiplier types, are not discussed in this report.



techniques based in space charge saturation or ratio comparison of the fast (differentiated) pulse height to the integrated total charge of the linear (slow) pulse, the zero crossover detection technique is not expected to depend on pulse amplitude properties (hence on light collection efficiency) as it is based solely upon the manner in which the slow pulse is processed by passive networks.

Since the zero crossover technique depends on the analytical form of the light flash, requirements of the photomultiplier system are quite stringent and it became apparent that at full aperture these may not be met. The requirements are that photoelectron multiplication should be identical throughout the stages for events across the photocathode and also that the transit time should be constant for events across the photocathode. As there is very little information in the literature regarding transit time spreads for photomultipliers with 5 inch diameter photocathodes, such measurements were made for several Amperex photomultipliers.

The arrangement, shown in Figure I.M.5a., used a miniature Gallium Phosphide electro-luminescent diode (XP-22, Ferranti Ltd., England) which has a light flash rise and fall time of less than 500 picoseconds. A Tektronix 110 relay pulse generator and trigger take-off system provided short current bursts (approximately 3 nanoseconds) to operate the diode and trigger a sampling oscilloscope (Tektronix 564). The trigger signal was used to provide a reference timing pulse for dual trace operation and photographs were taken to determine the time shift of the photomultiplier anode pulse as the light emitting diode traversed the photocathode. Figure I.M.5b. shows

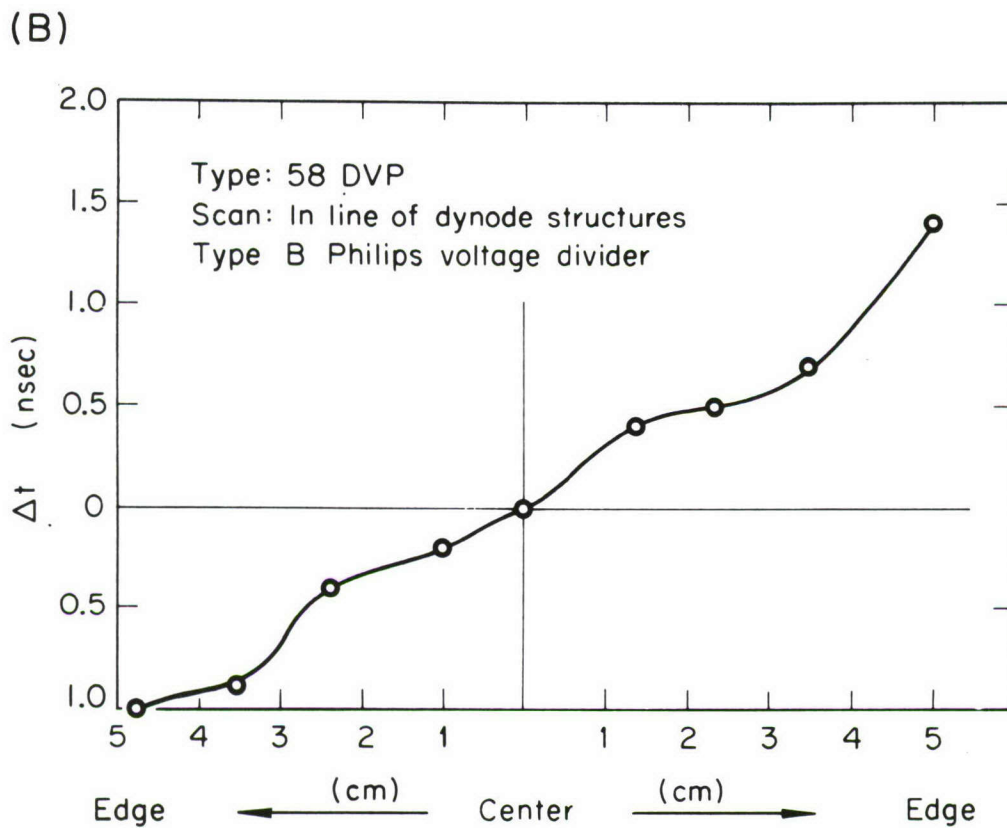
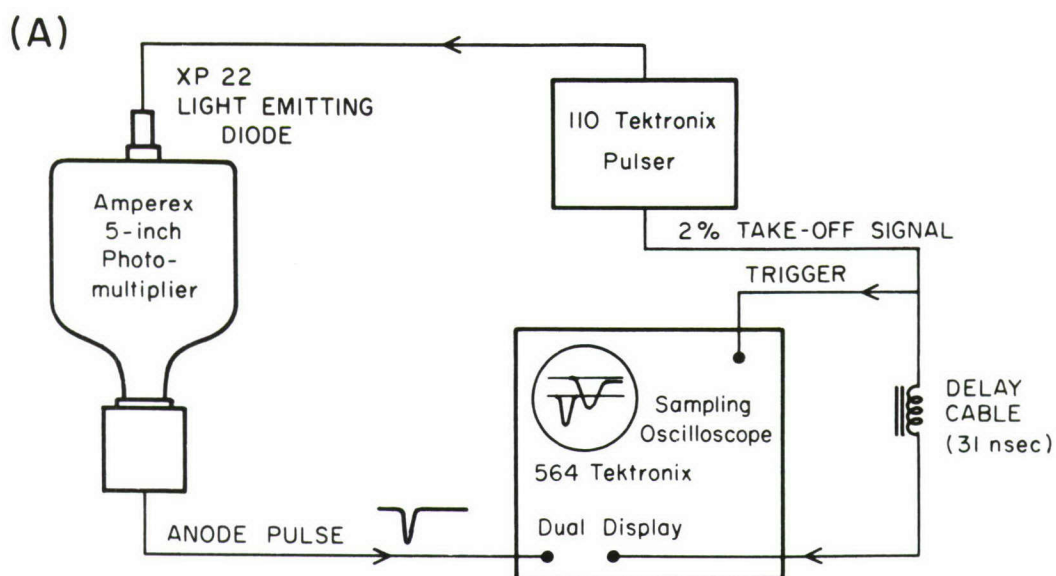


Figure I.M.5.

an example of the results with a 58 DVP (bi-alkali) phototube for measurements taken in the plane of the dynode structures and using a Philips type 'B' voltage divider arrangement. The difference in transit times between edges is approximately 2.4 nanoseconds, which is a significant effect. Since at full aperture the majority of photoelectron events are generated in the outer zones, it is concluded that the major factor limiting the performance of crossover detection p.s.d. systems using single large aperture phototubes is merely the existing non-uniform transit time across the photocathode, not the scintillator size. Deviations from the manufacturer's Type A and Type B voltage divider arrangements remain to be investigated to see if changes in the photocathode to first dynode focussing fields can generate a more uniform transit time distribution. Bellettini et al.<sup>(1)</sup> have shown that the standard voltage divider arrangements do not yield optimum photomultiplier performance in many cases.

To date the 5 inch diameter Amperex 58 AVP, XP 1040, and bi-alkali type 58 DVP photomultipliers, with type A and type B standard voltage dividers, have been used with 4 inch and 8 inch diameter NE213 and NE218 liquid scintillators to study the overall performance of a zero crossover p.s.d. system in obtaining maximum suppression of  $\gamma$ -rays for an experiment measuring a fast neutron total cross section.

The extent of gamma ray suppression achieved with 8 inch diameter NE213 using the p.s.d. circuit described earlier is illustrated in Figure I.M.6. which shows a neutron time-of-flight spectrum in the

---

<sup>1</sup>Bellettini et al., Nucl. Instr. and Meth. 21, 106 (1963).



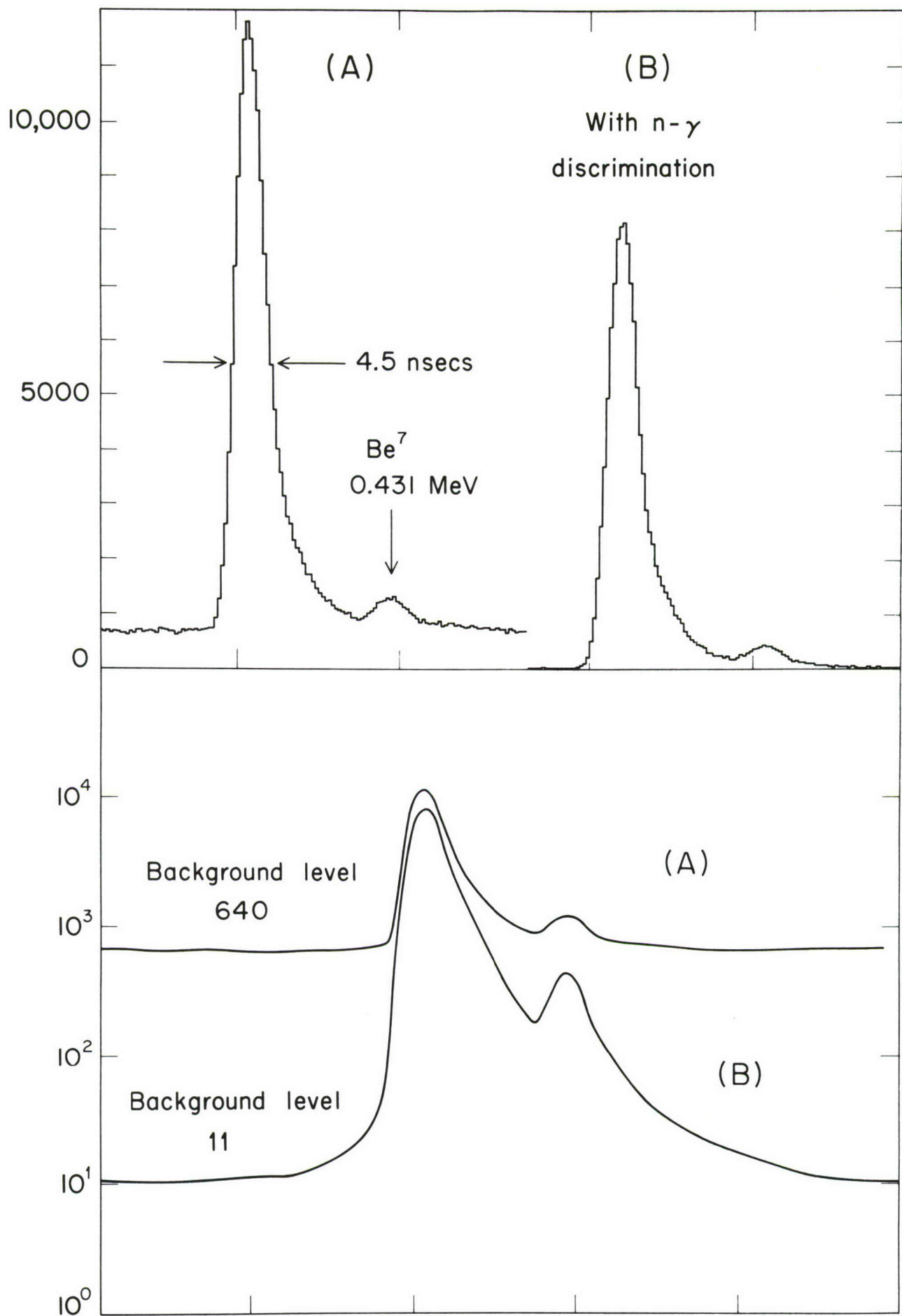


Figure I.M.6.

above mentioned experiment. The primary group corresponds to 2.37 MeV neutrons from the  ${}^7\text{Li}(\text{p},\text{n}){}^7\text{Be}$  reaction and the secondary group to neutrons from the reaction leading to the first excited state of  ${}^7\text{Be}$  at 431 keV. The effect of background suppression is seen more clearly in the logarithmic plot of the data. The peak to background ratio is improved by a factor of 44 on application of the n- $\gamma$  discrimination.

A paper describing the work presented above is being submitted for publication.

## II. NUCLEAR REACTIONS WITH CHARGED PARTICLES

### A. Van de Graaff Accelerator - L. Rothman, G. Carranza and C. Miller

#### 1. Accelerator Performance

There have been no significant operational problems with the Van de Graaff accelerator during the past year. Accelerator operation has been recorded with regard to progressive elimination of component failures and in an effort to obtain maximum running reliability. Thus, accelerator openings recorded as being caused by extractor power supply failures (which predominated over other component breakdowns in 1968) were completely eliminated in 1969 by redesign of the circuit. The three accelerator openings up to May 29th were all caused by supply failures to the R.F. power oscillator, and these supply circuits were then also rebuilt around another choice of power tube (5 by 5) allowing parallel full wave rectifier construction. There have been no accelerator openings since May 29th as a result of terminal component failures. Accelerator openings for such failures were necessary only 3 times during the past year, compared to 10 times in 1968, and the accelerator has been 'opened' only 15 times in the past year (as compared to 23 in 1968). The 12 openings, caused by routine replacement of gases and replacement of ion source bottles to meet particular experimental needs, were also utilized for routine maintenance.

Total "down time" comprised 48 days (compared to 46 in 1968) averaging again at 4 days per month. However, in the last year the



"down time" has largely been due to major installation changes to up-date the accelerator. Now that this phase is completed future "down time" should be extremely low. Machine running time totalled 5995 hours which corresponds to 18.9 hours per running day, including weekends and all holiday periods.

## 2. New Pumping System

During May, 1969, 15 days of "down time" were scheduled for the complete replacement of the pumping system of the accelerator. The large mercury pumps of the original installation were replaced by high speed oil pumps of a new type (NRC model VHS-6) noted for their pumping speed and extremely low backstreaming rates. Closed system Freon-12 refrigerator units (Tecumseh 1/3 H.P.) were used to feed refrigerated baffles on the pumps, and effluent from the baffles was used to cool baffled oil traps in the forepump lines. Pneumatically driven butterfly valves (Edwards model PQV-6) inserted between the pumps and the accelerator tubes are controlled through a detailed interlock system to fully protect the accelerator in the event of vacuum failure. The butterfly valves close and the accelerator shuts down at a vacuum worse than  $10^{-5}$  Torr, and in addition the oil pumps turn off at a pump vacuum worse than  $10^{-3}$  Torr. Complete shut down occurs for failure of electrical power water or compressed air and for other faults such as:

- a) refrigeration failure (using upper and lower limits for refrigerant pressure)
- b) diffusion pump overheating (using thermostatic sensors)

- c) failure of diffusion pump heaters (using a current transformer coupled to the heater lines)
- d) belt breakage on the mechanical (backing) pumps (using belt tension switches)

Indicator lights at the control desk give fault indication and the interlocks have to be sequentially cleared for re-starting. The new pumping system has been trouble free and completely maintenance free since its installation and there has been a significant reduction in running costs by the complete elimination of the liquid nitrogen and dry ice needed with the old system. The accelerator vacuum, as expected, has noticeably improved. The vacuum at the base of the Differential and Accelerator tubes is now  $5 \times 10^{-7}$  and  $1 \times 10^{-6}$  Torr respectively, and where the Accelerator tube system also includes the analysing magnet and sections of beam pipe, whose separate mercury pump was found to be limiting, not assisting, the ultimate vacuum level. Beam focusing through the accelerator has also unquestionably improved, together with beam loading characteristics.

As a result of the very satisfactory performance of this installation we are considering an improvement program for the supporting vacuum stations in the experimental areas. The present mercury pumps, combined with dry ice traps, are only capable of producing a vacuum of the order of  $5 \times 10^{-5}$  Torr directly at the pumps, and the use of dry ice traps with mercury is not particularly satisfactory as the "freeze-out" of mercury vapor on the traps often seriously reduces the pumping speed. There is little gain in

improving the vacuum of the accelerator to reduce gas scattering and increase beam output if relatively poor vacuum conditions exist in the beam pipes of the experimental areas.

A system is being designed to replace the mercury pumps by smaller high speed oil pumps and using a closed circuit arrangement of refrigerated water/glycol mixture at  $-10^{\circ}\text{F}$  to supply refrigerated baffles to be fabricated in the workshop and which will replace the dry ice traps. Conversion to this system will entirely eliminate the use of dry ice and liquid nitrogen by the accelerator facility.

### 3. Beam Pulsing

The installation of a time pick-off and signal display system as outlined in the last report was undertaken early in the year. The mechanical assembly consists of two "pick-off" cylinders, a time delay shift tube and a series of grounded field tubes mounted inside a cylindrical tank and installed above the analysing magnet. The beam burst entering a "pick-off" cylinder induces a small voltage pulse which is detected by an electronic circuit described elsewhere in this report. The capacitance of the cylinders is required to be as low as possible to generate a detectable signal, and the arrangement shown in Figure II.A.1., using a spider frame assembly, had a measured capacitance of 5 pf at the output terminals of the two cylinders. The beam burst entering the upper cylinder generates a signal for timing purposes and for external triggering of a sampling oscilloscope. The flight time through a grounded shift tube (center section)





provides a time delay before a second signal is generated in the lower cylinder. This signal is amplified and fed to the oscilloscope to illustrate the form of the beam burst. As mentioned in the last report, the pulsing performance of the Van de Graaff is very sensitive to the terminal control settings, especially focusing and steering controls. The time and signal pick off system enables continuous monitoring of the pulsing and display of the beam burst at the control desk so that the sharpest beam burst can be obtained. The time pick-off triggering signal is also counted by a high speed scaler gated by a crystal controlled time base so that the beam burst detection efficiency can be determined (the Van de Graaff pulses at 5 MHz repetition rate, crystal controlled). The monitoring system indicates that the Van de Graaff can produce beam bursts of 4 to 5 nanoseconds and this is confirmed by time resolutions obtained in several experiments. The system is now a permanent part of the Van de Graaff installation.

The terminal pulsing circuits also have been recently modified to include remote control (motor driven) fine tuning of the retrace oscillator which was found to be the most critical section as regards adjustment. Adjustment and tuning with the machine open were not reproduced with the machine closed and operating with the tank pressurized, probably due to temperature and/or pressure effects on circuit components. The remote control fine tuning is performed by minimizing circuit current drain as observed on the terminal metering through the telescopes and, to date, the arrangement seems to be working very satisfactorily.

The Van de Graaff has been increasingly used in pulsed beam experiments in the last year to the extent of approximately 20% of total running time, and fast beam pulsing is now a routine capability of the accelerator.

#### 4. Other Accelerator Improvements

As part of the program of up-dating the accelerator facility, a revision of the control room and the interfacing of cables to the experimental areas is in progress. Each of five experimental areas is being equipped with a minimum of 16 cables in unbroken runs to a main cable rack in the control room. In an effort to eliminate some existing problems of noise pick-up (presemably due to ground loops) the cables are being grounded only at the control room, and directly to the building structure via heavy copper rail. Out-dated electronic tube equipment has been removed from the control room. Existing R.I.D.L. transistorized 6 decade scalers have been modified, register counter circuits added to provide 10 decade storage capacity, and driver circuits added to enable operation from the logic levels of the newer NIM standard electronics modules of the laboratory. As the R.I.D.L. scales are only reliably useful at rates up to  $10^5$  c.p.s., five high speed ( $10^7$  c.p.s.) T.R.I. scalers have recently been added together with a T.R.I. Model 1510 time base (which enables the scalers to be time gated and used as frequency counters) to provide for high speed counting requirements (e.g. for use in pulsed beam experiments). Other supporting electronics have been constructed and a further 256 channel transistorized RCL analyser has been added



to supplement the existing 512 channel RCL analyser in the control room. Together with the on-line PDP-4 computer facility, a relatively complete system for data acquisition is now provided for all groups using the accelerator.

#### 5. Computer Services - W. Patton

During the past year several programs have been written for data handling. One such program was written for the angular correlation group so that the Columbia University IBM 360/91 computer could form a large number of gamma-ray spectra from the raw data on magnetic tapes produced by the PDP-4 on-line computer of the Van de Graaff. Programs were then written to allow the PDP-4 to inspect and analyse the "made-up" spectra (using the oscilloscope display system) and to add them together and fit gaussian peak shapes.

A program has also been written for the Mössbauer group using the Van de Graaff to enable the fitting of multiple Lorentzian peaks to Mössbauer spectra.

Several codes originally written for other computers have been adapted for use on the IBM 360/91 facility; these include a peak finding program and several DWBA codes, such as SCATT-4, ABACUS, DWUCK and TWOPAR.

A new data-taking program for the PDP-4 computer has been written to store pulser data in assigned locations in addition to two parameter (twin A.D.C.) data. This is used by the group studying lifetimes by doppler shift of gamma rays produced from proton capture reactions using twin target/backing arrangements on a rotating wheel

assembly to provide comparison of doppler shifts (centroid shifts) in the same geometry. Peak shifts in the pulser data are used to correct for rate dependent gain shifts in assessing centroid shifts between the twin targets.

A data taking program for the PDP-8 and PDP-9 computer system of the muonic X-ray group has been revised. A program has also been written to allow a PDP-8 computer (Nuclear Engineering) to read data from paper tape and write it on a magnetic tape in a form acceptable to direct processing on the IBM 360 computer. A similar data handling program has also been written for the Mössbauer group investigating Mössbauer effect in hemoglobin, so that multichannel analyser (paper tape) output can be written onto magnetic tape by the PDP-4 computer, eliminating the previous manual card punching of the data for processing by the IBM 360.

The FORTRAN systems program for the SEL 810-B computer (Nuclear Engineering) has also been modified to correct existing faults.

B. Particle - Gamma Ray Angular Correlations - S. B. Friedlander and I. J. Taylor

The investigation of levels in  $^{53}\text{Cr}$  using the  $^{52}\text{Cr}(\text{d},\text{p})^{53}\text{Cr}$  reaction has been completed.

Angular correlations between protons emitted at  $180^\circ$  and coincident gamma rays (utilizing the so-called "method II geometry" of Litherland and Ferguson) have yielded information on the spins of the first 9 excited states of  $^{53}\text{Cr}$  and on the gamma decay branching ratios and the multipole admixtures in the gamma decays.

Considerable time was spent this last year in unfolding the bulk of data obtained from the 3-parameter angular correlation system described in previous reports.

IBM 360 computer programs were developed to "make-up" gamma ray spectra from the on-line data which contained all gamma rays in coincidence with all protons for three simultaneous angles of the gamma ray detectors and for 'true' and 'accidental' coincidence timing.

Essentially, repeated passes through the data were required to construct particular  $\gamma$ -ray spectra (at a specified angle) for a specified proton group under conditions of 'true' time coincidence then to subtract out the background spectra obtained for 'accidental' time coincidence. The sorting was done through direct data storage in computer memory. Thereafter the "made up" spectra were separately processed to determine areas, etc. and to unfold  $\gamma$ -rays.

The analysis was further complicated by the presence of gain shifts observed in some parts of the data. The cause of this is still not established, but some intermittent instability in the Victoreen twin 4096 channel ADC's on line with the Van de Graaff's PDP-4 computer has been observed on other occasions, and since the correlation experiment involved had been run continuously for only one week on the Van de Graaff Accelerator, such effects may have excited during that period.

The data, therefore, were "blocked" to isolate the effect of gain drift (as the original data were taken in 'sub-runs,' this was fairly easy to do). Then the gains were renormalized by fitting to



prominent peaks and the spectra recombined again.

The final (p- $\gamma$ ) angular correlation results were then analyzed using the existing code in the laboratory developed several years ago by D. Church for angular correlation studies in several geometries.

We find spins of  $1/2^-$ ,  $5/2^-$ ,  $3/2^-$ ,  $1/2^-$  for the excited states of  $^{53}\text{Cr}$  at 560, 1010, 2320 and 3620, respectively. These results agree with tentative assignments reached on the basis of the neutron angular momentum transfer,  $l_n$ , deduced from (d,p) stripping angular distributions. They also agree with branching ratio data.

We have assigned a spin of  $5/2^-$  to the excited state at 1970 KeV. Since this level is not strongly excited in the (d,p) reaction, no  $l_n$  value has (to our knowledge) ever been quoted for it. This new assignment undoubtedly corresponds to a level having a  $5/2^-$  spin assignment which was calculated from the unified mode to occur at 1890 KeV.<sup>(1)</sup>

We have determined the E2/M1 multipole mixing ratios for the transitions from 1010, 1970 and 2320 KeV to the  $3/2^-$  ground state to be, respectively,  $S = -14^{+5}_{-22}$ ;  $S = -4.6^{+0.5}_{-0.7}$ ; and  $-5.7 < S < +0.09$ ,  $+0.47 < S < 5.7$  (both giving acceptable chi-squared values).

We expect to determine assignments for three other states at 1290, 2690 and 3700 KeV. The results for these states are more difficult to assemble than those for the other above mentioned states

---

<sup>1</sup>K. Ramavataram, Phys. Rev. 132, 2255 (1965).

because the 1290 KeV state is quite weakly excited by the (d,p) reaction, the 2690 KeV state is part of a triplet which our particle detector does not resolve, and the 3700 KeV state is only partially resolved from the 3620 KeV state by the particle detector. In addition, the 1290, 2690 and 3700 KeV states have strong branches to states other than the ground state so that their gamma-ray spectra are more complicated than the ones mentioned earlier (which have very strong ground state branches).

We are still involved in the data analysis for these three states, and it is expected that internally consistent assignments will be arrived at shortly.

The above work is now being written up as part of a thesis presentation (S. B. F.) and for submission for publication in the near future.

C. ( $^3\text{He},p$ ) Reactions on  $^{24}\text{Mg}$ ,  $^{26}\text{Mg}$ ,  $^{28}\text{Si}$  - B. Lawergren, J. B. Beyea and D. J. Chruch

Spectra and angular distributions were obtained from the  $^{24}\text{Mg}(^3\text{He},p)^{26}\text{Al}$ , the  $^{26}\text{Mg}(^3\text{He},p)^{26}\text{Al}$  and the  $^{28}\text{Si}(^3\text{He},p)^{30}\text{P}$  reactions. The bombarding energy was 10 MeV. Thick Ta absorbers were used in front of a solid state charged particle detector. Useful proton spectra were obtained at detector angles  $\geq 4^\circ$  with a resolution of  $\sim 100$  keV. The "absolute" efficiency calibration was obtained vis-a-vis the elastically scattered  $^3\text{He}$  groups which previously had been measured at other laboratories. Many proton groups leading to levels below 3 MeV excitation show two-nucleon stripping patterns

characteristic for  $L = 0$  and  $L = 2$  transfer. These have been analyzed with two DWBA codes written by Yates and by Zayman. The angular distributions can be fitted with reasonable wavefunctions for the initial and final states. In order to fit the absolute cross section the spectroscopic factors have to be estimated. It is hoped that these factors will reveal the changes in deformation between masses 24, 26, 28 and 30.

D. Levels in  $^{28}\text{Al}$  - J. Beyea, F. S. Rosenthal, B. T. Lawergren, L. J. Lidofsky

Levels up to 4 MeV in  $^{28}\text{Al}$  have been populated using the  $^{27}\text{Al}(d,p)^{28}\text{Al}$  reaction at 2 MeV. Gamma-proton coincidences have been accumulated with the proton counter at  $90^\circ$  and the gamma detector at  $57^\circ$ ,  $90^\circ$  and  $135^\circ$ . The close level spacing in  $^{28}\text{Al}$  and the 30 keV first excited state have made analysis using NaI crystals difficult. The superior resolution of germanium detectors, however, makes it possible to untangle the spectra.

The raw data, consisting of multidimensioned events, have been sorted into 30 gamma spectra, each of which corresponds to decay from one or two excited states in  $^{28}\text{Al}$ . The  $57^\circ$  data has been fit with peak finding routines and preliminary branching ratios established. Of particular interest is the fact that there appears to be two levels at 1.62 MeV, rather than one. A doublet is necessary to explain conflicting branches ratios and energies for the 1.62 when populated differently. The low energy state of the doublet has branches consistent with the  $1^+$  1.620 MeV level recently discovered



by Alburger and Harris<sup>(1)</sup>. The energy levels are  $3 \pm 1$  keV apart. This spacing is in essential agreement with unpublished work from Gronigen.<sup>(2)</sup>

E. Proton Bremsstrahlung from Carbon - J. Beyea and D. J. Church

A search has been made for inelastic proton scattering events from carbon which cannot be ascribed to well-studied nuclear processes. By eliminating false events which do not originate in the target, it is hoped to accurately measure the inelastic proton spectrum due to Bremsstrahlung gamma radiation. Equivalent measurements have been advocated to test various assumptions in nuclear scattering theory.<sup>(3)</sup>

For 3.5 to 5 MeV protons incident upon a 2 Mg/cm carbon target and scattered at an angle of  $135^\circ$ , we find an inelastic spectrum from 1 to 3 MeV which is typically a factor of 3 to 6 times greater than expected on the basis of simple calculations. Although it seems clear that the inelastic events we observe originate in the target, the rate is too high to be attributable to Bremsstrahlung. It is perhaps possible that the observed spectrum results from the sum of many inelastic peaks due to contaminant nuclei in the target, and efforts are being made to obtain purer targets. Other possible sources of false events originating in the target are also being

---

<sup>1</sup>Alburger and Harris, Physical Review 195, 1495 (1969).

<sup>2</sup>D. O. Boerma, private communication.

<sup>3</sup>R. Eisberg, D. Yennie, D. Wilkinson, Nucl. Phys. 18, 338 (1960); H. Fesbach, D. Yennie, Nucl. Phys. 37, 150 (1962).

investigated.

The energy of the scattered particles was measured in a silicon semiconductor detector colimated with scintillating CsI annular crystals operated in anti-coincidence. Thus, false events due to inelastic scattering in the colimators were rejected. The time of flight of the scattered particles was also measured to insure that the energy loss took place in the target, and not at the Van de Graaff slits, the chamber walls, etc. These experimental details are discussed in the next section.

F. Reduction of Background in Charged Particle Spectra -  
J. Beyea

Even when monoenergetic proton or Alpha particles are detected in a silicon detector, there is present an associated low energy tail which can be troublesome in certain kinds of experiments. In order to look for weak inelastic processes  $10^{-7}$  down from elastic scattering in the search for Bremsstrahlung events (previous section, it was necessary to reduce the low energy tail by a factor of a thousand.

Preliminary investigations indicated that certain simple precautions had to be taken to obtain reproducible results. The experimental setup was designed so that the detector could only "see" a small portion of the target and not the target frame. The incident beam itself was not colimated except at the Van de Graaff slits some 20 feet from the scattering chamber. Instead, a set of focusing quadrupole lenses were used to keep the beam spot small at the target.

In order to discover the source of the low energy tail,

time of flight studies were undertaken, requiring that the detector be far from the target. The detector was placed 60 cms. away at the end of a 3.5" diameter tube.

The flight tube was wide enough so that the beam spot could not "see" the tube walls. Thus in-scattering contributions to the background were removed and all multiple scattering effects thereby localized in the entrance and detector colimators. (It is necessary to colimate the detector to eliminate edge effects.)

In this set-up the background was reduced to a reproducible limit independent of machine focusing and other machine conditions. The background was essentially flat with the total number of counts adding up to approximately 1% of the elastic scattering peak independent of beam energy. (This corresponds to a peak-to-background ratio of roughly  $10^4$  to 1 for 5 meV protons detected with 50 keV resolution.)

The time of flight studies (operating the accelerator in pulsed mode and using the beam pick-off pulse as the start signal) showed that there were many different sources of background and that a time of flight measurement could be used to reject false events. Some of the background was due to particles losing energy back at the Van de Graaff slits, but by far the dominant contribution came from energy losses in the vicinity of the detector.

Subsequent studies showed that this was due to inelastic scattering in the detector colimator.

Because the time of flight condition was only capable of rejecting 95% of these false events, it was necessary to find a supplemental rejection system. It was decided to make the colimator



itself a particle detector so as to know when an inelastic scattering had taken place in the colimator. A CsI crystal was machined into a ring colimator and viewed from the edges with two phototubes. (Two phototubes were necessary to gain good light collection in this ring geometry.) The CsI colimator was operated in anti-coincidence with the main detector. In this way, the background due to colimator scattering was reduced by a factor of 50 to 100 across most of the spectrum. The dramatic effect of the rejection system is shown in Figure II.F.1. The residual false-events which escaped such rejection were eliminated by the time of flight condition. The time of flight condition also rejected false events from the Van de Graaff slits.

A second CsI colimator was used at the entrance to the flight tube. This colimator was particularly important in principle since the time of flight measurement could not distinguish between inelastic events in it and in the target. However, the number of such scatterings was too small to detect.

The combined system of CsI colimators and time of flight requirements resulted in a peak-to-false-background ratio of better than  $10^7$  to 1 for the lower two-thirds of the spectrum. For carbon, aluminum and nickel targets, the "real" background was always greater than this.

The subject of background tails in proton and alpha particle spectra at low energies has not received complete examination in the literature, no doubt due to the wide variety of effects which can contribute to it. The methods of rejection used here were designed for a particular experiment, but may prove useful in other applications.

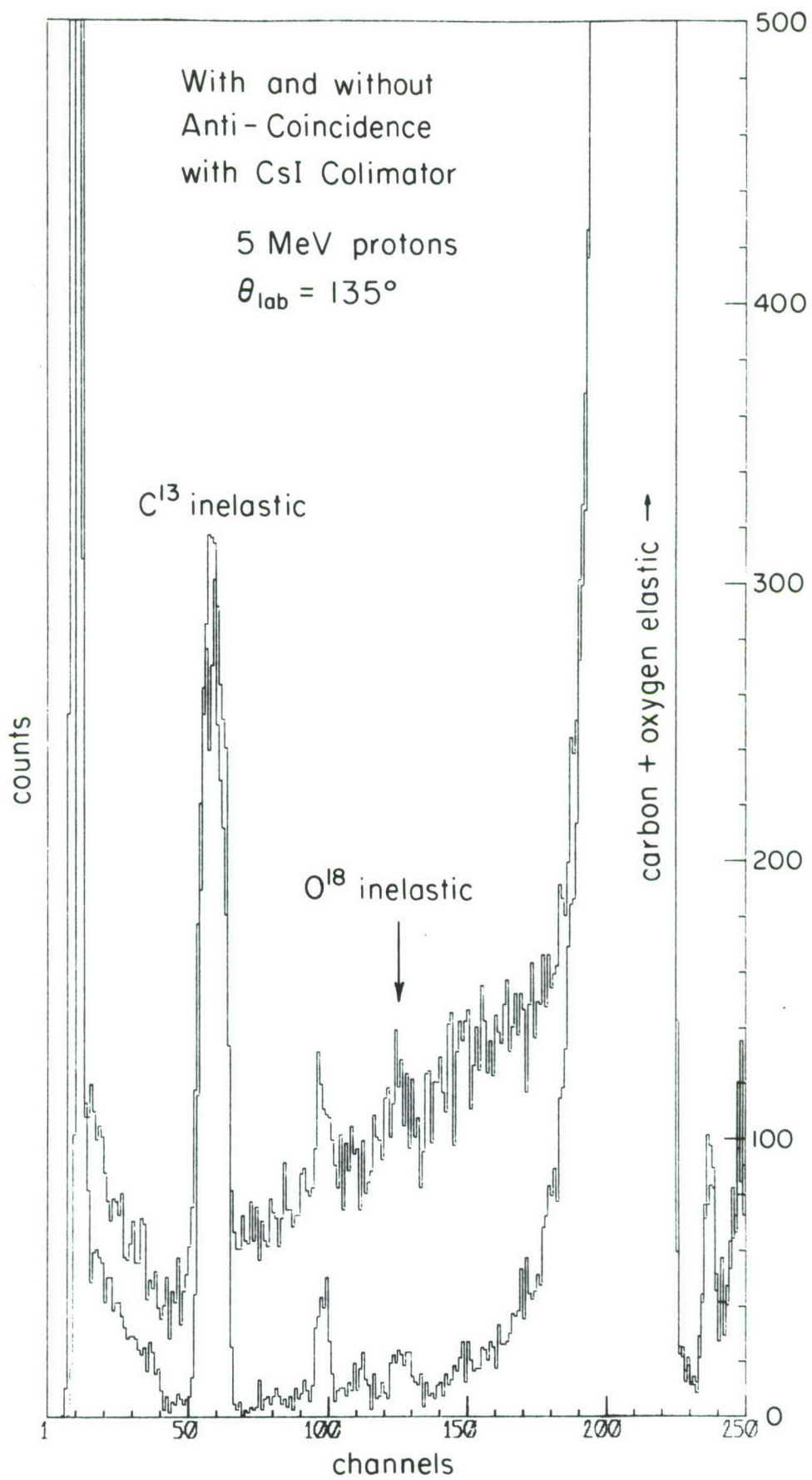


Figure II.F.1.

### III. BETA AND GAMMA SPECTROSCOPY AND ITS APPLICATION TO THE STUDY OF NUCLEAR STRUCTURE AND WEAK INTERACTIONS

#### A. The Double Beta Decay Experiment - J. Ostrowski, J. D. Ullman and C. S. Wu

##### 1. Recovery of the $^{48}\text{Ca}$ from the source

Last year we expected to chemically remove the Ra contamination in the  $^{48}\text{Ca}$  source which had limited the sensitivity of the experiment. The  $^{48}\text{Ca}$  was in the form of  $\text{CaF}_2$  powder held between two aluminum-foil sheets by an epoxy binder. The first thing that had to be done was to remove the epoxy and convert the calcium from fluoride to some more soluble compound.

Practice runs with natural calcium samples last year had shown that the epoxy could be removed by heating, and the  $\text{CaF}_2$  converted to  $\text{CaCO}_3$ , with a loss of about 2% of the Ca. It is extremely important to minimize this loss, since 1% of the  $^{48}\text{Ca}$  in the source is worth \$250.00. However, a dress rehearsal on one of the natural calcium "dummy" sources we had made as practice for the real source, yielded a loss of nearly 10%. This was unacceptable. Furthermore, the recovered material was obviously impure, having a deep red-grey color.

The impurity was identified as iron by spectroscopic analysis. The "dummy" source differed from the samples used for earlier practice runs in that its  $\text{CaF}_2$  had been ground fine in a ball mill, like the  $^{48}\text{Ca}$  in the real source. The iron came from the balls. The fineness of the powder apparently was the reason for the calcium loss: the very fine  $\text{CaF}_2$  powder was carried away by air currents when it was heated to drive off the epoxy.



The iron impurity could be removed by careful control of the Ph during one of the precipitations involved in the conversion from flouride to nitrate. The burning of the epoxy was done in a closed vessel. With these improvements, the loss on recovery of finely-ground  $\text{CaF}_2$  mixed with epoxy and deposited on a source was reduced to an acceptable level, with very little iron impurity present. Only after three successive complete rehearsals on natural calcium, involving grinding the  $\text{CaF}_2$ , mixing with epoxy and pouring it on an Al sheet, stripping of the Al sheet, burning off the epoxy in the closed system, and converting the  $\text{CaF}_2$  to  $\text{CaCO}_3$ , had given losses of less than 2%, did we attempt to recover the  $^{48}\text{Ca}$ .

The recovery of the  $^{48}\text{Ca}$  has been completed with the following results:

Weight of $\text{CaCO}_3$ originally received:	23.752 gm.
Weight of $\text{CaCO}_3$ after recovery:	<u>23.523 gm.</u>
Loss:	.229 gm.

The loss was thus less than 1%. This result stands as a tribute to the skill and patience of John Ostrowsky, who did not live to see it. He worked out all the chemical techniques used, went through seven complete rehearsals, and then personally conducted the recovery of the  $^{48}\text{Ca}$  until it was nearly complete, although he was mortally ill.

## 2. Experimental program for 1970

Since John Ostrowsky's skill and experience are no longer available to us, it appears unadvisable to go ahead with the many

chemical manipulations involved in purifying, re-depositing and again recovering the extremely expensive  $^{48}\text{Ca}$ . However, the importance of this experiment is greater than ever. Some explanations of the observed CP-violation in  $\text{K}_0$ -decay also predict a slight nonconservation of leptons. Also, mass-spectrometer experiments on minerals show definite evidence for double beta decay. There has been considerable speculation that these results may indicate such a slight lepton nonconservation.

Only an experiment such as ours can clear up this question. The nuclide  $^{82}\text{S1}$  has been shown by a mass-spectrometer experiment to double beta decay, with a half-life of  $1.4 \times 10^{20}$  years. Since this is at the lower limit of the range of lifetimes predicted for lepton-conserving double beta decay, there is speculation that it might indicate lepton nonconservation. If this is so, the double beta decay will take place without emission of neutrons. Our apparatus could easily detect neutrinoless double beta decay with a half-life of the order of  $10^{20}$  years.

Oak Ridge National Laboratory has an amount of  $^{82}\text{S1}$  sufficient for this experiment. We already have working apparatus for doing this experiment, and it is very important. We therefore intend to make a run with  $^{82}\text{S1}$  in the apparatus as soon as is practicable. The S1 is much less expensive than the  $^{48}\text{Ca}$  and can be used in the form received (metallic S1) so there should be none of the delays associated with doing chemistry on an extremely valuable isotope.

B. Experiment on the Einstein-Podolsky-Rosen Paradox -

L. Kasday, J. Ullman, C. S. Wu

1. Introduction

Einstein, Podolsky and Rosen (EPR) concluded in 1935 that observables associated with two distant non-interacting systems have definite values before they are measured, in contrast to the usual interpretation of quantum mechanics.<sup>(1)</sup> The recent work of Bohm and Aharonov, and Bell, leads us to expect a deviation from the prediction of quantum mechanics for the angular correlation of Compton-scattered positron annihilation radiation, if the conclusion of EPR is correct.<sup>(2)</sup> We have completed our measurement of this correlation.

We measured  $N$ , the rate of events in which both gamma rays from positron annihilation were scattered on plastic scintillators  $S_1$  and  $S_2$  (See Figure III.B.1a.) and were detected by NaI scintillators  $D_1$  and  $D_2$ . Quantum mechanics predicts  $N$  to vary as  $\cos 2(\phi_2 - \phi_1)$ .

We normalized  $N$  to the rates  $n_1$ ,  $n_2$  of events in which both photons scattered on  $S_1$  and  $S_2$  and one entered either  $D_1$  or  $D_2$  respectively\* (Figures III.B.1b,c.) More precisely, we measured

$$R(\Delta E_1, \Delta E_2, \phi_1 \phi_2) \equiv \left[ \frac{N \cdot (SS)}{n_1 n_2} \right]_{\Delta E_1 \Delta E_2 \phi} \quad (1)$$

\*Also, an  $N$  event counts as an  $n_1$  and an  $n_2$  event.

---

<sup>1</sup>A. Einstein, B. Podolsky, N. Rosen, Phys. Rev. 47, 777 (1935).

<sup>2</sup>D. Bohm and Y. Aharonov, Phys. Rev. 108, 1070 (1957); J. S. Bell, Physics 1, 195 (1964).



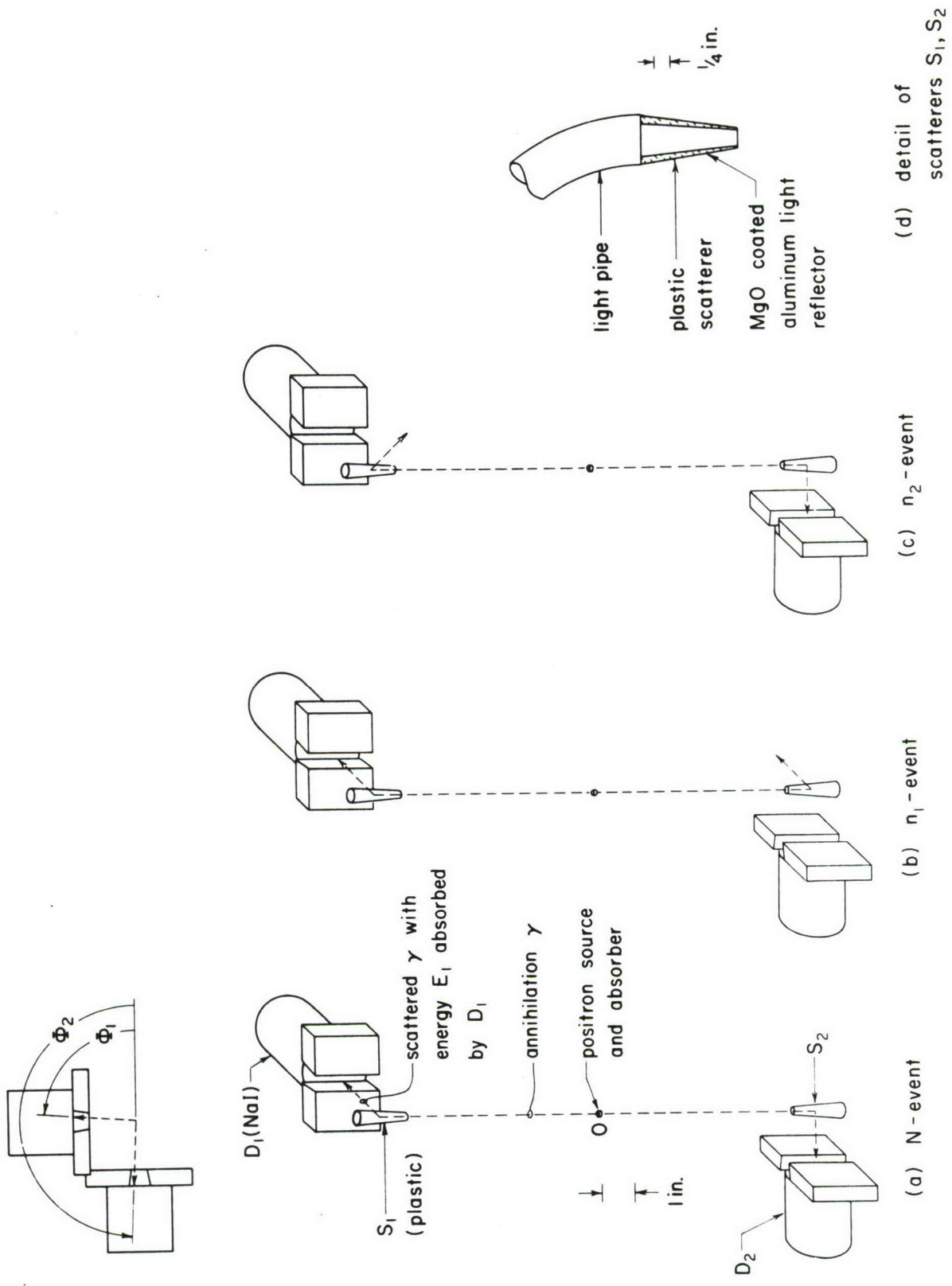


Figure III.B.1. Schematic view, to scale, of the experimental arrangement. The lead collimator is omitted.

where the slits defining the aximuthal angles were positioned at  $\phi_1$  and  $\phi_2$ , and we required that the scattered photons had energies in the intervals  $\Delta E_1, \Delta E_2$ .  $SS$  = the total rate of photons scattering simultaneously on both  $S_1$  and  $S_2$  (for all energies and angles).

We used this normalization because theory predicts a simple form for  $R$ , viz.

$$R = 1 - m(E_1, E_2) \cos 2(\phi_1 - \phi_2)$$

independent of the energies of the scattered photons, and largely independent of the details of our apparatus. The effect of the finite energy and angular resolution, and energy efficiency of the apparatus was to change  $m$  by a constant factor.

We made a number of runs at different settings of  $\phi_1$ . During the run,  $E_1$  and/or  $E_2$  was recorded for each valid event, and we summed over various  $\Delta E_1, \Delta E_2$  energy regions afterwards.

## 2. Apparatus

Since the last report, a suitable scatterer design was found (Figure III.B.1d.) and lead slits 1/2 inch thick were fashioned to select the aximuthal angle  $(\phi_1 - \phi_2)$ .

Also, electronic logic (Figure III.B.2.) was assembled to identify and record the  $N, n_1, n_2$  and  $SS$  events defined above.

### a. $n_1$ -events

The logic required that  $n_1$ -events satisfy a threefold time coincidence between  $S_1$ - $S_2$ - $D_1$ ; and that the total energy deposited in  $S_1$  and  $D_1$  lie in a window centered on  $\sim 511$  keV (= energy of annihilation

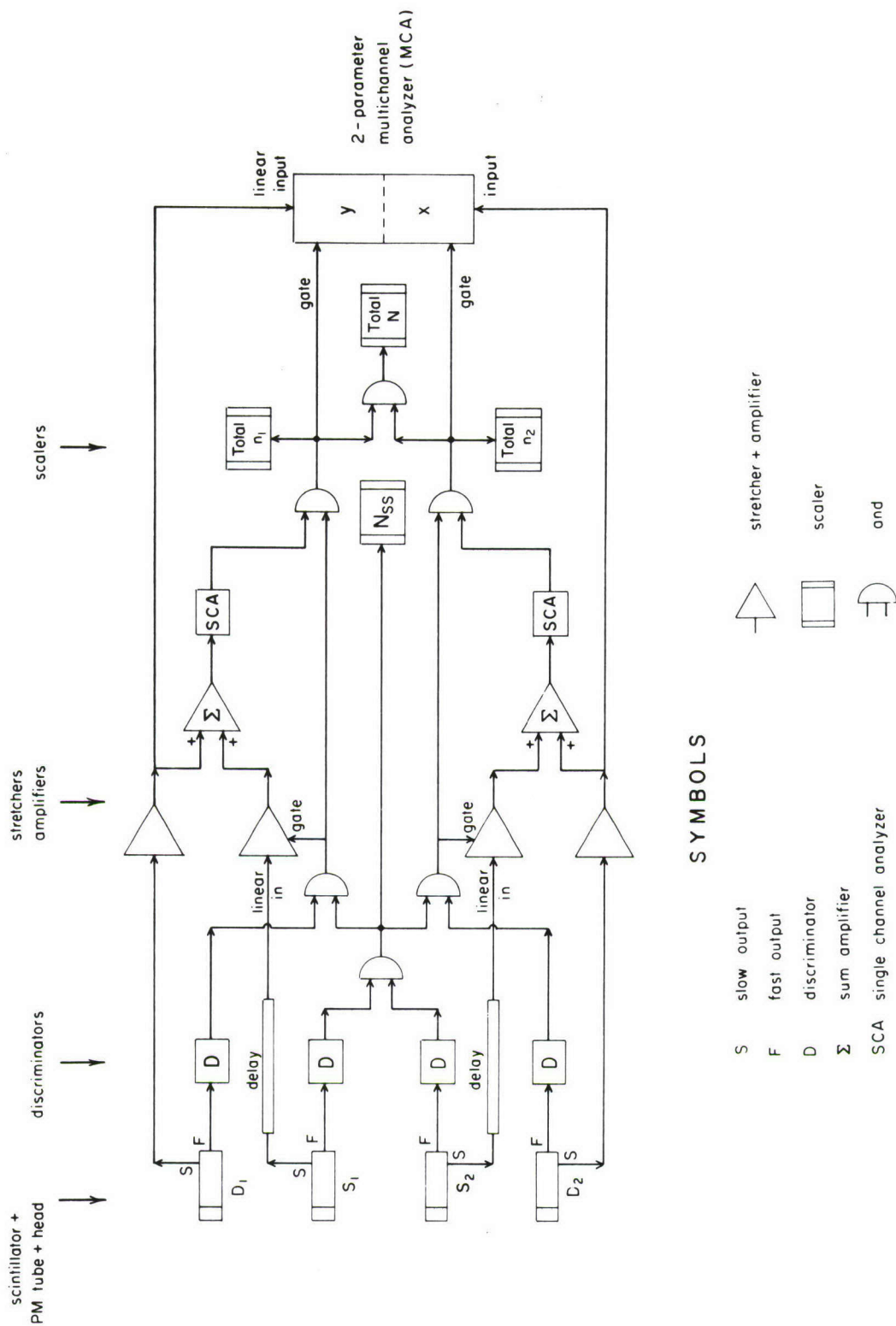


Figure III.B.2. Block diagram of the electronics.



$\gamma$  ray). The multichannel analyzer (MCA) collected a spectrum of  $E_1$  for the events.

b.  $n_2$ -events

Same as  $n_1$ -events except  $n_1 \neq n_2$ . The  $E_2$  spectrum was collected.

c. N-events

An event satisfying both the  $n_1$  and  $n_2$  requirements qualifies as an N-event also. The MCA collected a 2 parameter ( $E_1, E_2$ ) spectrum of these events. A scaler counted the total SS events. Also the total  $n_1, n_2, N$  events were counted for troubleshooting. The stretchers for the slow pulses from  $S_1, S_2$  had to be gated because of high count rates; gating signals were  $(S_1 S_2 D_1), (S_1 S_2 D_2)$ , respectively.

We used standard Pegram modules for slow logic and amplifiers, LeCroy modules for fast logic (and the gated stretchers), and a Nuclear Data 50/50 multichannel analyzer (with interfaced computer) for data collection and subsequent analysis.

### 3. Results

The data, summed over all energies accepted by the detectors, is shown in Figure III.B.3., with  $1\sigma$  error bars. Superimposed is a least  $\chi^2$  fit of the form  $A + B \cos 2(\phi_1 - \phi_2)$  [ $A = 1.007 \pm 0.003$ ].

Agreement with the expected  $1 + B \cos (\phi_1 - \phi_2)$  behavior is excellent. Theoretical values of  $B$  for this data, and data in small energy regions, are now being calculated. A thesis based on this work is being written by Leonard Kasday.

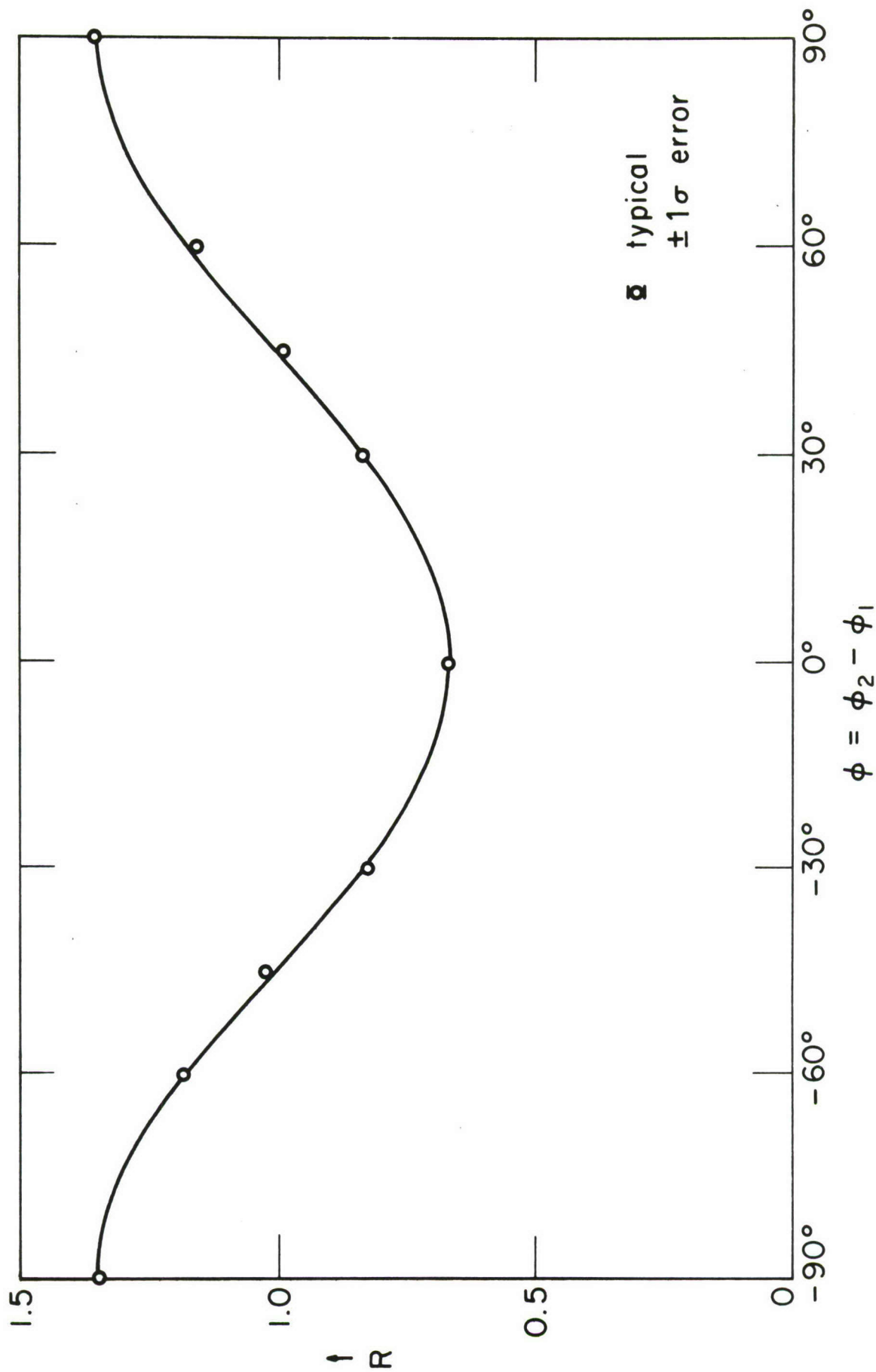


Figure III.B.3. Data summed over all energies of the scattered photons, with  $1\sigma$  error bars and least  $\chi^2$  fit of the form  $A + B \cos 2\phi$ . Data includes corrections for accidental coincidences.

C. Mössbauer Effect Following Coulomb Excitation: Tungsten -  
C. S. Wu, Y. W. Chow, E. Greenbaum, R. Howes, P. H.  
Swerdlow, C. Yen

Studies of hyperfine interactions in the first excited  $2^+$  states of the tungsten isotopes 182, 184, 186 have been completed. The electric quadrupole hyperfine interactions have enabled us to determine the ratios of the quadrupole moments as a function of neutron number. The results are  $Q(182):Q(184):Q(186) = 1:.930 \pm 0.16:.908 \pm 0.024$ . The quadrupole interactions have been studied in the ionic compound  $WS_2$ . Powder  $WS_2$ , as well as single crystals of  $WS_2$  (C-axis oriented both parallel and perpendicular to the direction of observation) were used as absorbers. The use of single crystals in this experiment reduced the number of lines in the absorption spectrum.

The motivation for studying these quadrupole ratios was to compare the experimental results with the theoretical predictions of the rotational model and the pairing-plus-quadrupole model calculations of Kumar and Baranger. All of these results are tabulated in Table III.C.1. To report on these results, a paper entitled "Mössbauer Effect Following Coulomb Excitations in Tungsten" has been published in Physics Letters, 30B 171 (1969).

The magnetic hyperfine interactions in the first excited  $2^+$  state were studied in an absorber composed of a tungsten-iron alloy (5%/95% by weight). The variation of magnetic dipole moment ratio with neutron number was observed to be  $\mu(182):\mu(184):\mu(186) = 1:1.09 \pm 0.3:1.15 \pm 0.04$ . These results are to be compared with the calculation of



Quadrupole Interaction Energies for $2^+$ States of $^{182,4,6}\text{W}$							
	$E_\gamma$ (keV)	$eQV_{zz} \times \frac{C}{E_\gamma}$ (mm/sec)				$WSe_2$ powder	$WSe_2$ II (neglect $\Delta E_{I.s.}$ )
		$WS_2 \perp$	$WS_2$ powder	$WS_2$ II (neglect $\Delta E_{I.s.}$ )	$WSe_2$ powder		
$W^{182}$	100.1	$10.08 \pm 0.08$	$10.03 \pm 0.11$	$10.19 \pm 0.06$	—	—	$0.015 \pm 0.067$
$W^{184}$	111.1	$8.36 \pm 0.11$	$8.42 \pm 0.12$	$8.38 \pm 0.09$	—	—	$0.01 \pm 0.07$
$W^{186}$	122.5	$7.47 \pm 0.17$	$7.49 \pm 0.19$	$7.22 \pm 0.13$	—	—	$0.03 \pm 0.09$
$Ta^{182}$	100.1	$10.25 \pm 0.10$	$10.11 \pm 0.11$	$10.06 \pm 0.06$	$9.19 \pm 0.10$	$9.26 \pm 0.15$	$0.013 \pm 0.060$
$Re^{186}$	122.5	$7.32 \pm 0.18$	$7.33 \pm 0.20$	$7.25 \pm 0.15$	$6.88 \pm 0.18$	$6.74 \pm 0.23$	$0.02 \pm 0.08$
		$Q_{22}^{184} : Q_{22}^{182}$		$Q_{22}^{186} : Q_{22}^{182}$		$\frac{Q_{22}^{182}(184)}{Q_{02}} : \frac{Q_{22}^{182}(182)}{Q_{02}}$	
RESULTS OF PRESENT EXPERIMENT		$0.930 \pm 0.016$		$0.908 \pm 0.024$		$0.983 \pm 0.020$	
KUMAR AND BARANGER		0.946		0.862		0.981	
ROTATIONAL MODEL		$0.946 \pm 0.009$		$0.902 \pm 0.009$		1.00	
						$1.007 \pm 0.028$	
						0.925	
						1.00	

Table III C.1

S. G. Nilsson, O. Prior, and F. Boehm, who included pairing connections in evaluation of the g factors. All of these results are tabulated in Table III.C.2. Both the Mössbauer effect following Coulomb excitation in Hafnium and the Mössbauer effect in sickle cell anemia are now in progress.

D. Mössbauer Effect Following Coulomb Excitation: Hafnium -  
C. S. Wu, Y. W. Chow, E. Greenbaum, R. Howes, P. H.  
Swerdlow, C. Yen

In order to test the validity of microscopic nuclear models such as the pairing plus quadrupole forces of Kumar and Barringer, it is necessary to have increasingly accurate measurements of such macroscopic nuclear properties as g-factors and electric quadrupole moments. One hopes to observe trends due to the addition of neutrons in a series of consecutive isotopes. We have performed such a measurement of quadrupole ratios of the  $2^+$  states of  $^{182}\text{W}$ ,  $^{184}\text{W}$ , and  $^{186}\text{W}^{(1)}$ , and found support the simple rotational model of Bohr and Mottleson in disagreement with the results of Kumar and Barringer. The even isotopes of hafnium, 176, 178 and 180, offer another opportunity to test detailed nuclear calculations by a measurement of the ratios of quadrupole moments of excited nuclear states using the Mössbauer effect following Coulomb excitation.  $^{176}\text{Hf}$ ,  $^{178}\text{Hf}$  and  $^{180}\text{Hf}$  have half lives of  $2.05 \times 10^{-9}$  sec.,  $2.23 \times 10^{-9}$  sec.  $2.25 \times 10^{-9}$  sec., respectively, and B(E2) values 0.299, 0.273 and 0.269 with low internal conversion coefficients (5.85, 4.72 and 4.68). The energies of the  $2^+$  states are 88.3 keV for  $^{176}\text{Hf}$ , 93.1 keV for  $^{178}\text{Hf}$  and 93.3 keV for  $^{180}\text{Hf}$  while all ground states are  $0^+$  and therefore

---

<sup>1</sup>Y. W. Chow et al., Physics Letters, 30B, 171 (1969).

	$(c/E_\gamma) \text{ g } \mu_N \text{ H}_{\text{int}}$ mm/sec	$g_A : g_{182}$	Theory (I) $g_A : g_{182}$	Theory (II) $g_A : g_{182}$
$^{182}\text{W}$	$1.556 \pm .014$	1	1	1
$^{184}\text{W}$	$1.531 \pm .031$	$1.09 \pm .03$	1.08	1.13
$^{186}\text{W}$	$1.469 \pm .039$	$1.15 \pm .04$	1.12	1.17

Table III C.2



have no quadrupole moment.<sup>(1)</sup> Consequently they are easily Coulomb excited by the 8 meV alpha beam of the Columbia Van de Graaff accelerator.

Although R. E. Snyder et al.<sup>(2)</sup> have studied quadrupole splitting in these isotopes using radioactive sources, we will improve their experiment in several respects. Firstly the only available sources for  $^{176}\text{Hf}$  ( $^{176\text{m}}\text{Lu}$ ) and  $^{180}\text{Hf}$  ( $^{180\text{m}}\text{Hf}$ ) have very short half lives of 3.7 hours and 5.5 hours respectively. Secondly the  $^{180\text{m}}\text{Hf}$  was prepared in the form of  $\text{HfO}_2$  which has a monoclinic crystal structure and emits a gamma split by the interaction of the internal electric field gradient and the quadrupole moment of the excited nuclear state. The method of Coulomb excitation can provide a Hf source from a single crystal of hafnium metal and give a simplified Mössbauer spectrum. Through the use of separated isotopes to resolve the gamma lines of  $^{178}\text{Hf}$  and  $^{180}\text{Hf}$ , data can be taken simultaneously for  $^{176}\text{Hf}$  and  $^{178}\text{Hf}$  and for  $^{176}\text{Hf}$  and  $^{180}\text{Hf}$ . This eliminates discrepancies due to fluctuations in our driving system, or the temperature of the system. and to slight changes in the crystalline structure of the target or absorber material.

Using cubic  $\text{HfC}$  as a target and absorber should yield a Mössbauer spectrum of only one line; however we observed an obvious splitting due to radiation damage in the target.

---

<sup>1</sup>Stelson and Grodzins, Nuclear Data, A1, 21 (1965-66).

<sup>2</sup>R. E. Snyder et al., Proc. of the Phys. Soc. of London, 1, 1662 (1968).

Our result is confirmed by the recently published work of C. G. Jacobs et al.<sup>(1)</sup> We have found that hafnium metal exhibits negligible radiation damage when used as a target under 150 nanoamperes of the alpha beam but yields a gamma line split by the interaction of the quadrupole moment of the  $2^+$  state with the electric field gradient of the hexagonal metal. Therefore, we plan to use a metallic hafnium target and an isotopically enriched HfC absorber and have procured a single crystal of Hf metal. By orienting this crystal along its axes, we will be able to observe the Mössbauer effect in the crystal with its axis of symmetry either perpendicular or parallel to the direction of observation and obtain Mössbauer spectra of one or two components respectively. These simple spectra can be fit very precisely and should yield a more accurate measurement of the ratio of the quadrupole moments of the  $2^+$  states of  $^{176}\text{Hf}$ ,  $^{178}\text{Hf}$  and  $^{180}\text{Hf}$ .

E. The Mössbauer Effect as a Technique of Medical Research -  
C. S. Wu, Y. W. Chow, E. Greenbaum, R. Howes, P. H.  
Swerdlow, C. Yen

Sickle cell anemia is a fatal, hereditary hemoglobin disease that has been variously determined to afflict 0.03 to 0.13 percent of Americans - about 600,000 people.<sup>(2)</sup> Red blood cells containing a predominance of abnormal sickle cell hemoglobin are distorted into sickle-like shapes because the hemoglobin molecules bond together into chains, distending the cell walls. Shock and sudden death often result from clogging of small capillaries by the elongated red blood

---

<sup>1</sup>C. G. Jacobs et al., Physics Letters 29A, 498 (1969).

<sup>2</sup>A. Cantarow and B. Schepartz, Biochemistry, W. B. Saunders Co., Philadelphia (1962).

cells. At present, only palliative treatment is possible--symptoms may sometimes be soothed, but they cannot be cured.\* Many afflicted individuals die before they are ten; even with care, few live to forty.

Research in this disease, however, has been minimal; and knowledge of the exact nature of the fatal hemoglobin-hemoglobin bonding, which is presently lacking, is considered to be essential before a method of treatment can be devised. Because this bonding must change the electromagnetic fields in its vicinity, there will be changed nuclear hyperfine interactions--for nuclei near the molecular change. In appropriate nuclei this can be detected by the Mössbauer effect, which measures a product of nuclear properties times local electromagnetic field values. In conventional Mössbauer experiments, the nuclei to be studied are put in a lattice with a "known" electromagnetic field, and thus the Mössbauer parameters give information about nuclear properties. In our sickle cell anemia experiment, however, this is reversed. We are using an extensively studied Mössbauer nuclide ( $^{57}\text{Fe}$ ), and are observing the electromagnetic fields in its immediate vicinity.\*\* One can detect extremely small variations in

---

\*The increased fragility and distortion of these red blood cells causes symptoms of anemia (reduced oxygen carrying capacity of the blood), hemolysis (increased blood destruction), and thrombosis (obstruction of vascular channels due to the formation of blood clots).

\*\*If one measures no change in the Mössbauer spectrum, one knows that any change in molecular structure could not have occurred in that region.



molecular structure when the Mössbauer nucleus is situated nearby.\*

Since oxidation of sickle cell anemia hemoglobin prevents sickling, the hemoglobin-hemoglobin bond is suspected to occur near an iron atom in one or both molecules. We have therefore begun by making a careful comparison of the iron Mössbauer spectra made with normal hemoglobin (Hb-A) and sickle cell anemia hemoglobin (Hb-S) absorbers.

In hemoglobin, the iron atom is located at the center of a ring formed by four nitrogen atoms (called a central porphyrin ring), and thus to a first approximation the iron is in an axially symmetric location with respect to its nearest neighbors. The combination of iron with porphyrin is called haem. To make hemoglobin, a globin (a large protein) is attached to the ring in the "down" position.\*\* The attachment of the globin destroys the symmetry about the iron, and thus there is an electric field gradient at the iron site. This causes the hyperfine splitting we have observed. The "up" position to the iron in haem is available for bonding to a ligand (a complex-forming negative ion). This is where an oxygen molecule is attached as the blood circulates through the lungs. Clearly, if any ligand is

---

\* Knowledge about the relative populations at different sites in the molecule, the ionic or covalent state of the Mössbauer atom, and the strengths and types of chemical bonds helps one to choose among possible molecular structures in that region.

\*\* There are two slightly different forms of globin called  $\alpha$ - and  $\beta$ -globins. The complete hemoglobin molecule consists of four globins, two of each kind, each having a haem ring. The differences in the amino acid sequences between the  $\alpha$ - and  $\beta$ - globins occur far from the iron sites, and thus all four iron nuclei in a hemoglobin molecule are in the same electro-magnetic field.

attached to the iron, the electron density and thus the electromagnetic field will change at the iron site, and there will be a corresponding change in the iron Mössbauer spectrum.

We have recorded Mössbauer spectra made with oxygenated and deoxygenated Hb-A absorbers. The large difference confirms that one may indeed detect altered chemical structure by studying nuclear structure. As expected (because oxidation prevents sickling), we have recorded a much larger difference between deoxygenated than between oxygenated Hb-A and Hb-S spectra. Calculations are in progress to relate our measured Mössbauer parameters to changes in hemoglobin structure, and more detailed measurements are being made.

We will extend the scope of this study by attaching other Mössbauer nuclides (especially  $^{129}\text{I}$ ) to hemoglobin and using the nuclei of these atoms as probes to study other regions of the molecule. We will also examine the Mössbauer spectra of atoms in other forms of abnormal hemoglobin. Additional experiments are contemplated with Mössbauer nuclides other than iron--such as zinc and iodine in insulin, iodine in thyroxine, potassium in nerve tissue, and tungsten in viruses.

Most biochemical techniques measure macroscopic quantities determined by average molecular properties. In many medical experiments it is simpler (though not as useful) to determine the chemical formula of a biological macromolecule than to study the three-dimensional structure

at its active regions.\* We expect that our technique, which uses nuclear structure to examine localized three-dimensional molecular structure, may be the first important medical application of the actual knowledge of nuclear physics. Up to now nuclear physics has found widespread use in medicine only because of the tagging and tissue-destroying properties of nuclear radiation.

We are confident that the results of this experiment will illustrate the importance of cooperation and communication among different scientific fields. In a relatively inexpensive experiment we expect to confirm, in terms of human welfare, the usefulness of basic nuclear research. For without preceding studies of nuclear structure one could not think of examining molecular abnormalities by detecting changes in nuclear structure.

F. Proposed Investigations Using Oriented Nuclei in  $^3\text{He}|^4\text{He}$  Dilution Refrigerator - C. S. Wu, Y. W. Chow, E. Greenbaum, R. Howes, P. H. Swerdlow, C. Yen

The satisfactory operation of  $^3\text{He}|^4\text{He}$  dilution refrigerator at a temperature as low as 10 m°K makes many important and interesting experiments possible. The following three types of experiments are under consideration:

1. Tests of important invariance principles in physics.
2. Studies of Fermi and Gamow-Teller interactions in beta transitions.

---

\* Evidence is growing that biological systems operate on the molecular level through a three-dimensional "lock and key" mechanism of recognition. Important examples are the recognition of antigens by antibodies and the replication of DNA. Therefore, the determination of three-dimensional molecular structure is increasingly important for the effort to transplant organs without tissue rejection and to treat hereditary diseases.



3. Studies of nuclear moments of high excited states with lifetimes in the region of nanoseconds to picoseconds.

1. Test of the invariance of electromagnetic interaction under time reversal.

In 1964, careful investigations of decay of the  $K_2$  mesons indicated strongly that the cp invariance is violated in weak interaction by less than 1%. According to T. D. Lee, the  $K_2$  results can be interpreted as arising from violation of C invariance in the electromagnetic interaction of hadrons. Conservation of p in strong and in electromagnetic interactions, together with PCT, leads one to expect violation of T in electromagnetic interaction.

The lack of time-reversal violations found in various tests up to this moment indicates that any interaction which violates T invariance is probably weaker than  $\sim 3 \times 10^{-3}$  of the hadronic force strength. All the existing results do not favor the proposal that the electromagnetic interactions of the hadrons are responsible for CP violation. However, the experiments are not yet sufficiently accurate to rule out this proposal. Therefore, more accurate tests of T invariance in nuclear physics will become imperative. The present experiment under consideration is expected to give more accurate test of T by another order of magnitude.

In the proposed experiment, one measures the angular correlations of two successive gamma rays emitted in a  $2(E2 + M1)2(E2)0$  cascade from oriented nuclei in a  $^3\text{He}|^4\text{He}$  refrigerator with magnetic field in positive and negative directions. The angular correlation function

can be written in the following expression.

$$W(k_1 \cdot k_2) = (1 + |\delta|^2) + [.25 + .732|\delta| \cos \eta - .0765|\delta|^2] \cdot P_2(\hat{k}_1 \cdot \hat{k}_2) \\ + 3.27|\delta|^2 P_4(\hat{k}_1 \cdot \hat{k}_2) - .368\rho|\delta| \sin \eta [(\hat{k}_1 \cdot \hat{k}_2) \vec{J} \cdot (\hat{k}_1 \times \hat{k}_2)]$$

where  $k_1, k_2$  are unit vectors of the two gamma rays, and the mixing parameters  $|\delta|$  and  $\eta$  for the first gamma ray are related to the reduced matrix elements by the following relation:

$$\frac{E2}{M1} \equiv \delta \equiv |\delta| e^{i\eta}$$

$p$ , the polarization is equal to  $10^{-8} \frac{H}{T} g \frac{j'+1}{j'}$ .

With a magnetic field in negative  $J$  direction, the angular correlation function is the same, except that the term  $[(\hat{k}_1 \cdot \hat{k}_2) \vec{J} \cdot (\hat{k}_1 \times \hat{k}_2)]$  changes sign. The asymmetry under the reversal of the magnetic field direction is just the asymmetry under time reversal and it can be expressed as

$$A = \frac{W_{\uparrow\downarrow} - W_{\downarrow\uparrow}}{W_{\uparrow\uparrow} + W_{\downarrow\downarrow}} \approx .368\rho|\delta| \sin \eta [(\hat{k}_1 \cdot \hat{k}_2) \vec{J} \cdot (\hat{k}_1 \times \hat{k}_2)]$$

By considering the following: geometry of two gamma ray detectors at  $45^\circ$ ; temperature of  $10 \sim 30$  m°K; magnetic field of 100 Kgauss; and a source of 30 mC; one has to do the experiment for 10 days in order to get a more accurate test of  $T$  than the existing results.

The experimental arrangement is as shown in Figure III.F.1.

## 2. Studies of Fermi and Gamow-Teller interactions in beta transition

When nuclei are oriented, the angular distributions of the radiation intensity of gamma rays depends on the angle between the radiation and the direction of orientation of the nucleus. On the other

hand, angular distribution of the radiation of gamma rays depends on the spin, the nuclear matrix elements, etc. Therefore, experimental measurement of angular distributions of radiation from oriented nuclei gives insights into nuclear structure.

Consider the beta decay of a nucleus with the subsequent emission of a gamma ray. For the example of a  $2^+ \xrightarrow{\beta} 2^+ \xrightarrow{\gamma} 0$  transition, the angular distribution of the gamma (with respect to nuclear orientation axis) is given by:

$$W(\theta) = 1 - \frac{15}{14}(1 + \lambda)N_2 f_2 P_2(\cos\theta) - 5/3(5\lambda - 2)N_4 f_4 P_4(\cos\theta)$$

where  $f_2$  and  $f_4$  are the orientation parameters which describe the degree of orientation, and  $\lambda$  is a parameter which describes the beta interaction in the decay of nuclei.

$$\frac{1}{\lambda} = 1 + \frac{C_A^2 \langle \sigma \rangle^2}{C_V^2 \langle 1 \rangle^2}$$

$\langle \sigma \rangle$  and  $\langle 1 \rangle$  are the nuclear matrix elements for the Gamow-Teller and Fermi interactions respectively. By measuring the angular distribution of gamma rays, one can determine the nuclear matrix elements  $\langle \sigma \rangle$  and  $\langle 1 \rangle^2$ .



IV. MUONIC ATOMS AND NUCLEAR STRUCTURE - S. Bernow, B. Budick\*,  
M. Y. Chen, S. Cheng, S. Devons, D. Hitlin†, J. W. Kast, W. Y.  
Lee, E. R. Macagno, J. R. Rainwater, A. M. Rushton and C. S. Wu

#### Introduction

In this report we briefly summarize the essential findings concerning nuclear structure which we obtained from a detailed analysis of our measurements of muonic atoms. In the past year, beside improving our experimental facilities and carrying out several new investigations, we have devoted a considerable amount of time to analyzing our data from previous experiments and to interpreting them in terms of nuclear structure. By properly applying the nuclear polarization to the dynamic h.f.s spectra of deformed nuclei, we now have some sensible understanding of the charge distributions of these deformed nuclei. The isotope shifts have yielded a tremendous amount of information on the nuclear charge distribution vs. the number of neutrons, shell closure effects and the well known staggering effect. Moreover, the muonic isotope shifts provide a way to extract the specific mass effects in the optical isotope shift. The muonic magnetic h.f.s. spectra in  $^{115}\text{In}$ ,  $^{113}\text{Cs}$ ,  $^{127}\text{I}$  and  $^{141}\text{Pr}$  have been studied and compared favorably with the theoretical calculations of the Bohr-Weisskopf effect with configuration mixing models. The riddle of the intensity anomaly in  $^{127}\text{I}$  can be interpreted by a resonance excitation process. New investigations on isotone effects and fission processes induced by pions and muons have been successfully carried out in the past year. It is quite clear that

---

\* Permanent address: New York University, New York, New York

† Now at SLAC, Stanford University, Stanford, California

the investigation of muonic atoms gives us a most sensitive tool for probing into not only the static properties of the nuclear structure but its dynamic effects as well.

A. Charge Distribution of the Nd Isotopes (Reported to the Third International Conference on High Energy Physics and Nuclear Structure, Columbia University, September 8-12, 1969).

It is well established that the optical isotope shifts for pairs of isotopes with 88 and 90 neutrons in  ${}_{60}\text{Nd}$ ,  ${}_{62}\text{Sm}$  and  ${}_{63}\text{Eu}$  are anomalously large.<sup>(1)</sup> This is directly related to a change in the neutron-shell configuration. The sudden onset of permanent deformation occurs at a neutron number of 90, as predicted by the nuclear model of Nilsson. It is the increase in nuclear deformation, coupled with the usual increase in nuclear volume, that gives origin to such anomalous isotope shifts.

To explore the variation of the nuclear charge distribution in this interesting transition region, we have made precise measurements of the energies and isotope shifts of the muonic K and L lines in the Nd isotopes ( $A = 142, 143, 144, 145, 146, 148, 150$ ). The results have been partially reported elsewhere.<sup>(2-3)</sup> We wish in this note to

---

<sup>1</sup>D. N. Stacey, Rep. Progr. Phys. 29, 171 (1966).

<sup>2</sup>E. R. Macagno et al., Proceedings of the International Conference on Electromagnetic Sizes of Nuclei, Ottawa (1967); C. S. Wu, Proceedings of the International Symposium on the Physics of One and Two Electron Atoms, 1968, North Holland Publishing Company.

<sup>3</sup>E. R. Macagno, S. Bernow, M. Y. Chen, S. C. Cheng, S. Devons, I. Duerdoth, D. Hitlin, J. W. Kast, W. Y. Lee, and J. Rainwater, C. S. Wu and R. C. Barrett, to be published.

present a recent determination of the isotopic variation of parameters of the nuclear charge distribution from our measurements of the even isotopes.

We have analyzed the muonic (2p - 1s) and (3d - 2p) transition energies in terms of the parameters  $c$  and  $t$  of the Fermi distribution

$$\rho(r) = \rho_0 [1 + \exp(\frac{r-c}{0.228t})]^{-1} \quad (1)$$

and in terms of the parameters  $c$ ,  $t$  and  $\beta$  ( $\beta$  fixed to values derived from  $B(E2)$  measurements<sup>(1)</sup>) of the "deformed" Fermi distribution

$$\rho(r) = \rho_0 \{1 + \exp(\frac{r - c[1 + \beta Y_{20}(\theta, \phi)]}{0.228t})\}^{-1} \quad (2)$$

The analysis included dynamic hyperfine effects, which are very pronounced in  $^{150}\text{Nd}$ , as well as nuclear polarization and Lamb shift<sup>(2)</sup> corrections. The measured energies and the values of the parameters of the charge distributions are presented in Table IV.A.1. The errors quoted for the parameters include uncertainties in the various corrections mentioned above. Plots of the parameters versus mass number  $A$  are shown in Figures IV.A.1. and IV.A.2.

It is of great interest to note that even for these isotopes in the transition region, where the shape of nuclei changes from spherical to spheroidal, the skin thickness  $t$  does not vary a great

<sup>1</sup>P. H. Stelson and L. Grodzins, Nuclear Data 1A, 21 (1965);  
P. A. Crowley et al., Bull. Am. Phys. Soc. 13, 79 (1968).

<sup>2</sup>R. C. Barrett, Phys. Letters 28B, 93 (1968).



TABLE IV.A.1.

Isotope	Line	Measured Energy	Fermi Distribution		Deformed Fermi Distribution	
			c (fm)	t (fm)	c (fm)	t (fm)
$^{142}\text{Nd}$	$K_{\alpha 1}$	$4352.06 \pm 0.40$	$5.75 \pm 0.03$	$2.38 \pm 0.08$	$5.80 \pm 0.03$	$2.32 \pm 0.08$
	$K_{\alpha 2}$	$4270.44 \pm 0.50$				$0.104$
	$L_{\alpha 1}$	$1402.97 \pm 0.25$				
	$L_{\alpha 2}$	$1472.32 \pm 0.25$				
$^{144}\text{Nd}$	$K_{\alpha 1}$	$4336.38 \pm 0.45$	$5.80 \pm 0.03$	$2.37 \pm 0.08$	$5.85 \pm 0.03$	$2.27 \pm 0.08$
	$K_{\alpha 2}$	$4254.88 \pm 0.55$				$0.123$
	$L_{\alpha 1}$	$1402.59 \pm 0.25$				
	$L_{\alpha 2}$	$1471.82 \pm 0.25$				
$^{146}\text{Nd}$	$K_{\alpha 1}$	$4321.18 \pm 0.40$	$5.77 \pm 0.03$	$2.45 \pm 0.08$	$5.82 \pm 0.03$	$2.42 \pm 0.08$
	$K_{\alpha 2}$	$4240.50 \pm 0.50$				$0.151$
	$L_{\alpha 1}$	$1402.58 \pm 0.20$				
	$L_{\alpha 2}$	$1470.99 \pm 0.25$				
$^{148}\text{Nd}$	$K_{\alpha 1}$	$4303.46 \pm 0.45$	$5.80 \pm 0.03$	$2.46 \pm 0.08$	$5.84 \pm 0.03$	$2.40 \pm 0.08$
	$K_{\alpha 2}$	$4223.76 \pm 0.50$				$0.197$
	$L_{\alpha 1}$	$1403.54 \pm 0.25$				
	$L_{\alpha 2}$	$1470.97 \pm 0.25$				
$^{150}\text{Nd}$	$K_{\alpha 1}$	$4266.37 \pm 0.40$	$5.90 \pm 0.03$	$2.42 \pm 0.08$	$5.86 \pm 0.03$	$2.35 \pm 0.08$
	$K_{\alpha 2}$	$4198.30 \pm 0.50$				$0.279$
	$L_{\alpha 1}$	$1419.08 \pm 0.25$				
	$L_{\alpha 2}$	$1474.88 \pm 0.25$				

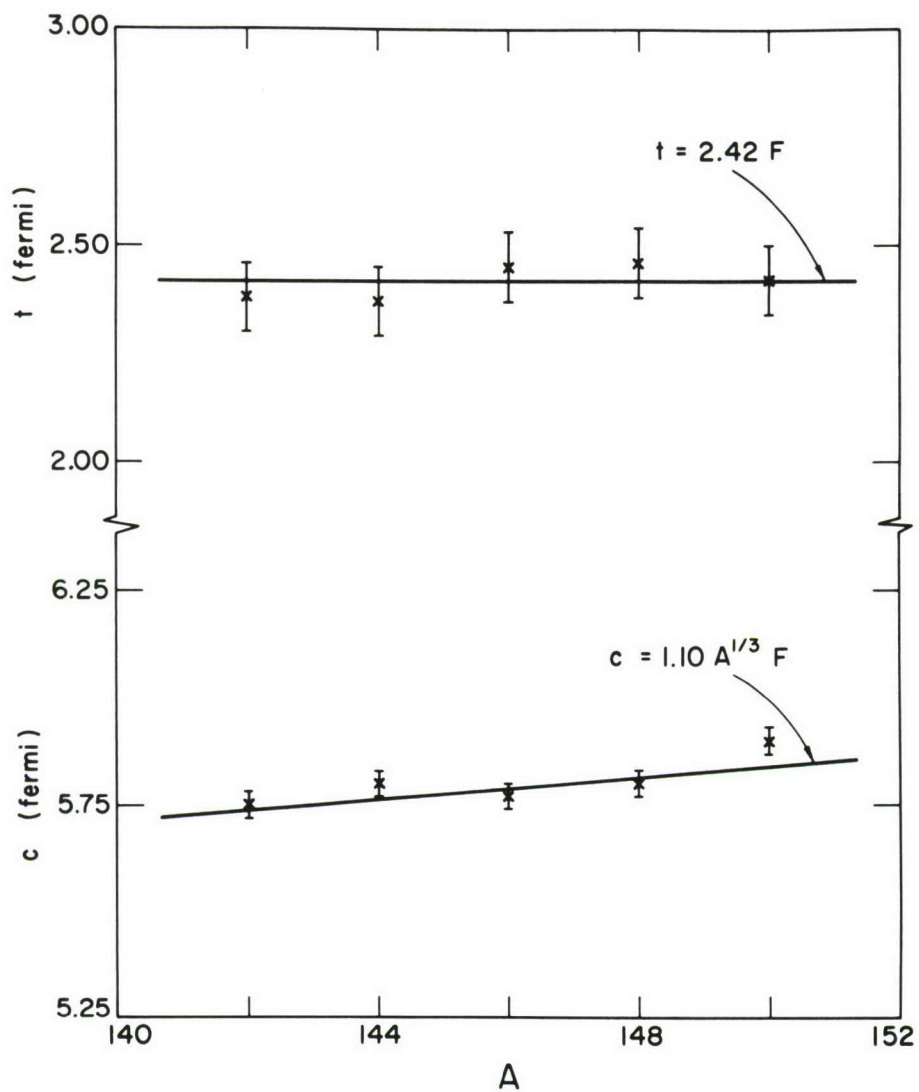


Figure IV.A.1.

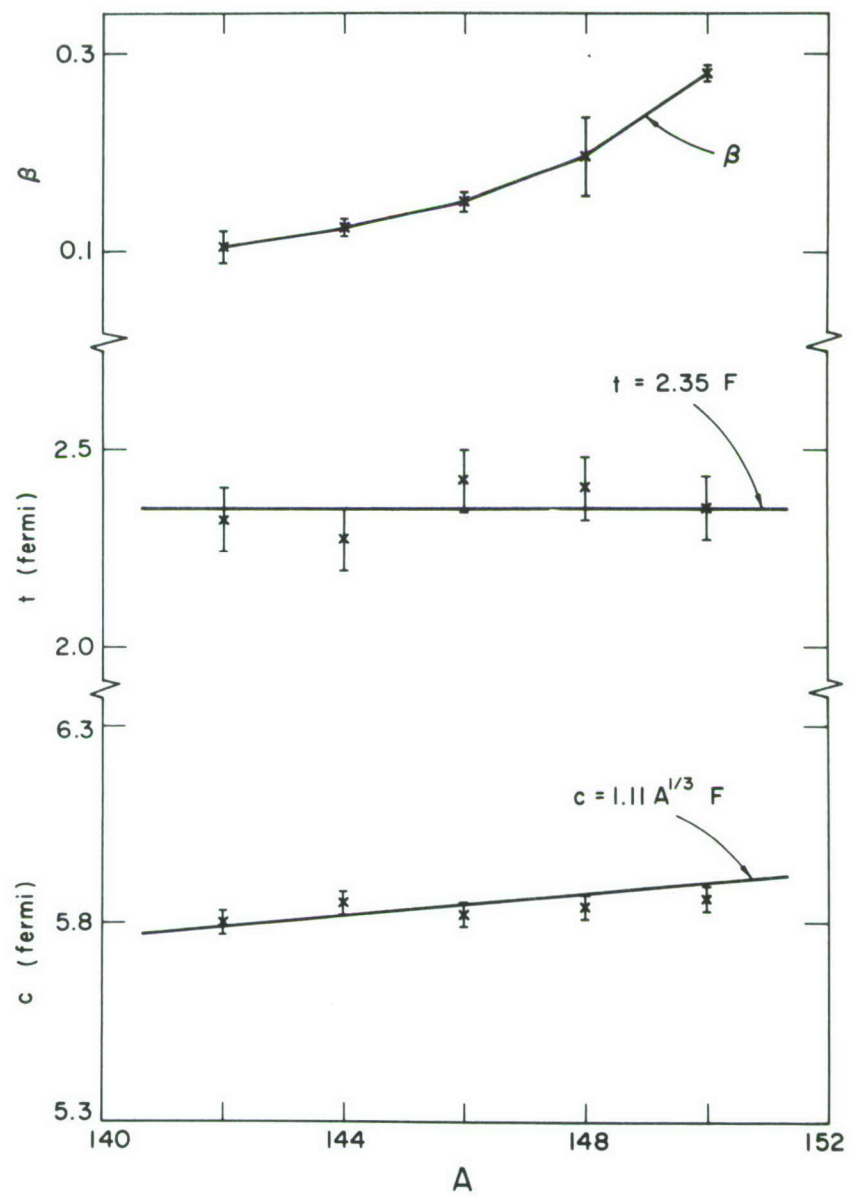


Figure IV.A.2.



deal. As a matter of fact, our results indicate that within the quoted uncertainties, we can consider the skin thickness as constant for the even Nd isotopes. For the deformed model, the skin thickness is generally smaller by a few percent than the corresponding values for the spherical model, as would be expected.

Since the skin thickness  $t$  is reasonably constant for the even Nd isotopes, it is possible, as shown in reference 1 below, to compare the muonic results with corresponding optical measurements, and to thus extract from the measured optical isotope shifts the optical lines, and the specific mass effects determined; these results appear in reference 3, page

B. Isotope Shifts in Tin; Comparison of Muonic and Optical Measurements (Reported at the Boulder Meeting of the Nuclear Physics Division, American Physical Society).

The isotope shifts between seven muonic tin isotopes ( $A = 116, 117, 118, 119, 120, \text{ and } 122 \text{ and } 124$ ) were remeasured to high precision. The observed shifts are listed in Table IV.B.1. We have obtained from the observed shifts the shifts due to the field effect, i.e., variations of the nuclear charge distribution from isotope to isotope, by subtracting the reduced mass contribution; the differences of nuclear polarization or Lamb shift between the isotopes are negligible. For purposes of reference, we have evaluated the ratio of the field effect shift to the standard shift which is calculated under the assumption of a uniform nuclear charge distribution with radius  $R = 1.2 A^{1/3} \text{ fm}$ . The values of this ratio (also shown in

---

<sup>1</sup>C. S. Wu and L. Wilets, Annual Review of Nuclear Science, 1969.

TABLE IV.B.1.

Isotope Pair	Observed Shift (keV)	Field Shift (keV)	Standard Shift (keV)	[ $\delta E_{\text{field}}/\delta E_{\text{std}}$ ]	
				This Experiment	Other Determinations
$^{116}\text{Sn} - ^{117}\text{Sn}$	$2.35 \pm 0.10$	2.38	5.15	$0.46 \pm 0.02$	$0.45 \pm 0.03^{(1)}$
$^{116}\text{Sn} - ^{118}\text{Sn}$	$6.10 \pm 0.10$	6.16	10.25	$0.60 \pm 0.01$	$0.630 \pm 0.023$
$^{118}\text{Sn} - ^{119}\text{Sn}$	$1.84 \pm 0.16$	1.87	5.10	$0.37 \pm 0.03$	$0.35 \pm 0.04$
$^{118}\text{Sn} - ^{120}\text{Sn}$	$5.23 \pm 0.08$	5.29	10.08	$0.52 \pm 0.01$	$0.521 \pm 0.014$
$^{120}\text{Sn} - ^{122}\text{Sn}$	$4.44 \pm 0.05$	4.49	9.93	$0.45 \pm 0.02$	$0.508 \pm 0.016$
$^{122}\text{Sn} - ^{124}\text{Sn}$	$4.39 \pm 0.10$	4.44	9.80	$0.45 \pm 0.01$	
$^{116}\text{Sn} - ^{124}\text{Sn}$	$20.16 \pm 0.20$	20.38	40.06	$0.503 \pm 0.005$	$0.457 \pm 0.015^{(3)}$

Table IV.B.1) are all about 0.5. The odd-even isotope shifts exhibit the well known staggering effect.

Ehrlich's<sup>(1)</sup> recent results are also listed in Table IV.B.1. for comparison purposes. The isotope shifts studied by both groups (116-117, 116-118, 118-119, 118-120, 120-122) are in good agreement except that for the pair (120-122), for which a difference in the shifts of  $(0.5 \pm 0.23)$  keV is observed. The (122-124) shift was not measured by Ehrlich. The K X-ray spectra for the two isotopes  $^{122}\text{Sn}$  and  $^{124}\text{Sn}$  are shown in Figure IV.B.1.

Several measurements of optical isotope shifts of tin have been made, the most precise and extensive ones are by Stacey.<sup>(2)</sup> The electron X-ray isotope shift of tin has been reported only for the pair  $^{116}\text{Sn} - ^{124}\text{Sn}$ .<sup>(3)</sup> To obtain the field effects in the optical results, the specific mass correction (due to correlations in the motions of all the electrons<sup>(4)</sup>) must be first extracted. By using the method of King,<sup>(5)</sup> Stacey was able to put a limit on the value of the specific mass correction of not less

---

<sup>1</sup>R. D. Ehrlich, Phys. Rev. 173, 1088 (1968).

<sup>2</sup>D. N. Stacey, Proc. Roy. Soc. A, 280, 439 (.964).

<sup>3</sup>R. B. Chesler and F. Boehm, Phys. Rev. 166, 1206 (1968).

<sup>4</sup>D. N. Stacey, Rep. Progr. Phys. 29, 171 (1966).

<sup>5</sup>W. H. King, Proc. Roy. Soc- A, 280, 430 (1964).

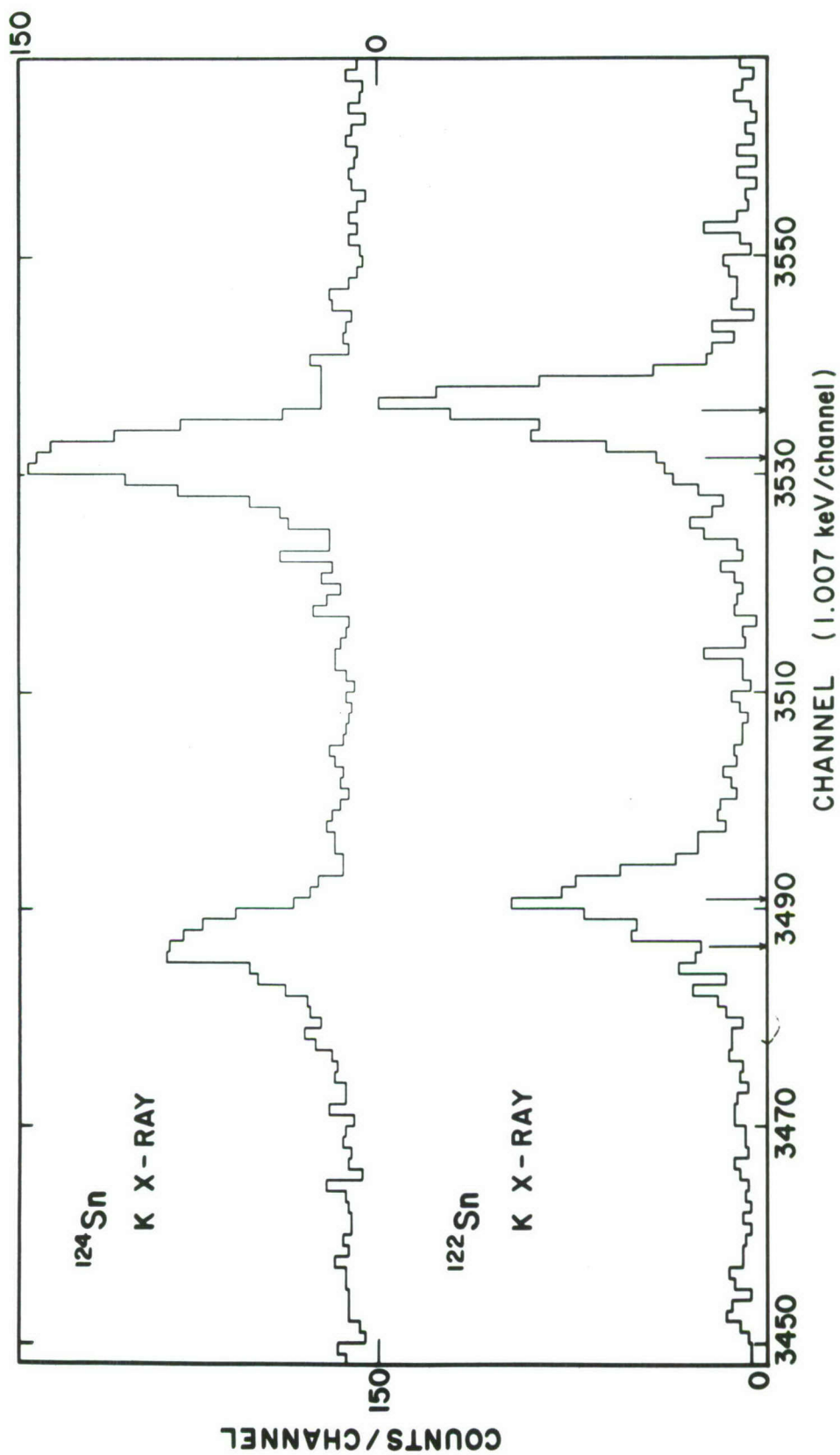


Figure IV.B.1.



than 4 mK ( $1 \text{ mK} = 10^{-3} \text{ cm}$ ). By comparing the optical and electronic X-ray results between the pair (116-124), a value equal to  $-3.13 \pm 0.25 \text{ mK}$  was obtained.<sup>(1)</sup> By directly comparing the optical and muonic X-ray results of even isotopes of tin, Ehrlich<sup>(2)</sup> obtained a value of  $-3.3 \pm 0.6 \text{ mK}$  which is in agreement with the other results quoted above. In this type of extraction of the specific mass correction in optical shifts by normalizing to the muonic isotope shifts, the effect of the higher moments of the nuclear charge distribution is negligible because only the ratios of the shifts enter into the normalization. As shown by Wu and Wilets<sup>(3)</sup>, when variations of the skin thickness ( $\delta t$ ) are only a few per cent, the ratios of energy shifts are approximately equal to the ratios of the variations of the second moments,  $\delta \langle r^2 \rangle$ . However, in a careful examination, the variations of the muonic isotope shifts in even tin isotopes are seen not to be in close agreement with the optical shifts, as shown in Figure IV.B.2a. Particularly, our measurement of the isotope shift between  $^{122}\text{Sn}$  and  $^{124}\text{Sn}$  showed a marked deviation from the optical shift. In the optical results, after the specific mass correction ( $m = -3 \text{ mK}$ ) is made, the shift between  $^{122}\text{Sn}$  and  $^{124}\text{Sn}$  is less than 60 per cent of the shift between  $^{120}\text{Sn}$  and  $^{122}\text{Sn}$ . In our muonic results, these two shifts are both equal to 4.5 keV. Figure IV.B.1 is a direct

---

<sup>1</sup>R. B. Chesler and F. Boehm, Phys. Rev. 166, 1206 (1968).

<sup>2</sup>R. D. Ehrlich, Phys. Rev. 173, 1088 (1968).

<sup>3</sup>C. S. Wu and L. Wilets, Annual Review of Nuclear Science, 1969.

comparison of the K lines of  $^{122}\text{Sn}$  and  $^{124}\text{Sn}$ ; a shift of 4.5 keV is clearly evident.

There are two possible ways to explain this discrepancy. One is that the optical or muonic measurements of  $^{122}\text{Sn} - ^{124}\text{Sn}$  are in error. In view of the agreement between our results and Ehrlich's in five pairs of the Sn isotopes, the error in the shift in  $^{122}\text{Sn} - ^{124}\text{Sn}$  would be expected to be no more than  $\pm 0.6$  keV. Moreover, Hindmarsh and Kuhn,<sup>(1)</sup> in an earlier and considerably less precise measurement in a different optical line, found the 120-122 and 122-124 shifts to be equal. The other explanation is that the nuclear configurations undergo an abrupt change from  $^{122}\text{Sn}$  to  $^{124}\text{Sn}$  which is somehow manifested by a sudden drop in the optical isotope shift but not in the muonic results. This is possible, but it is hard to understand. The even tin isotopes are very similar: the nuclei are spherical, with low energy level schemes that are very much alike and change smoothly from  $^{116}\text{Sn}$  to  $^{124}\text{Sn}$ . This is also evident in the prediction of several theoretical calculations of the optical isotope shifts based upon different nuclear models. Uher and Sorensen,<sup>(2)</sup> using the pairing plus quadrupole model, have predicted a value of  $\delta E/(\delta E)_{\text{std}} \sim 0.5$  for all isotope pairs. In a calculation based on the theory of finite Fermi systems, Krainov and Milulinskii<sup>(3)</sup> found a value of  $\delta E/(\delta E)_{\text{std}} \approx 0.89$  for the (116-118) and (118-120) pairs and a value

---

<sup>1</sup>W. H. Hindmarsh and H. G. Kuhn, Proc. Phys. Soc. 68A, 433 (1955).

<sup>2</sup>R. A. Uher and R. A. Sorensen, Nucl. Phys. 86, 1 (1966).

<sup>3</sup>V. P. Krainov and M. A. Mikulinskii, Sov. J. Nucl. Phys. 4, 665 (1967).

equal to 0.61 for the (120-122) and (122-124) pairs. (We have used calculated values of  $(\delta E)_{\text{std}}$  of Babushkin<sup>(1)</sup> in order to obtain the quoted values of this ratio.) The results of a similar calculation by Bunatyan<sup>(2)</sup> are listed below (also obtained with  $(\delta E)_{\text{std}}$  values from reference (1) below).

Isotope Pair	$(\delta E)/(\delta E)_{\text{std}}$
(116-118)	0.49
(118-120)	0.41
(120-122)	0.33
(122-124)	0.26

(It should be noted that Krainov and Mikulinskii assume that the extra neutron pairs between  $^{118}\text{Sn}$  and  $^{116}\text{Sn}$  and between  $^{120}\text{Sn}$  and  $^{118}\text{Sn}$  are  $(1g_{7/2})^2$  pairs, whereas the extra neutron pairs between  $^{122}\text{Sn}$  and  $^{120}\text{Sn}$  and between  $^{124}\text{Sn}$  and  $^{122}\text{Sn}$  are  $(1h_{11/2})^2$  pairs. Bunatyan, on the other hand, takes all these neutron pairs as  $(1h_{11/2})^2$  pairs.)

None of these three calculations would explain a sudden drop in the optical isotope shift for  $^{122}\text{Sn} - ^{124}\text{Sn}$ . The variation of the observed muonic isotope shifts in tin is in quite good agreement with the theoretical predictions, as shown in Figure IV.B.2b.

---

<sup>1</sup>F. A. Babushkin, Sov. Phys. JETP 17, 1118 (1963).

<sup>2</sup>G. G. Bunatyan, Sov. J. Nucl. Phys. 4, 502 (1967).

# Isotope Shifts in Even $_{50}\text{Sn}$ Isotopes

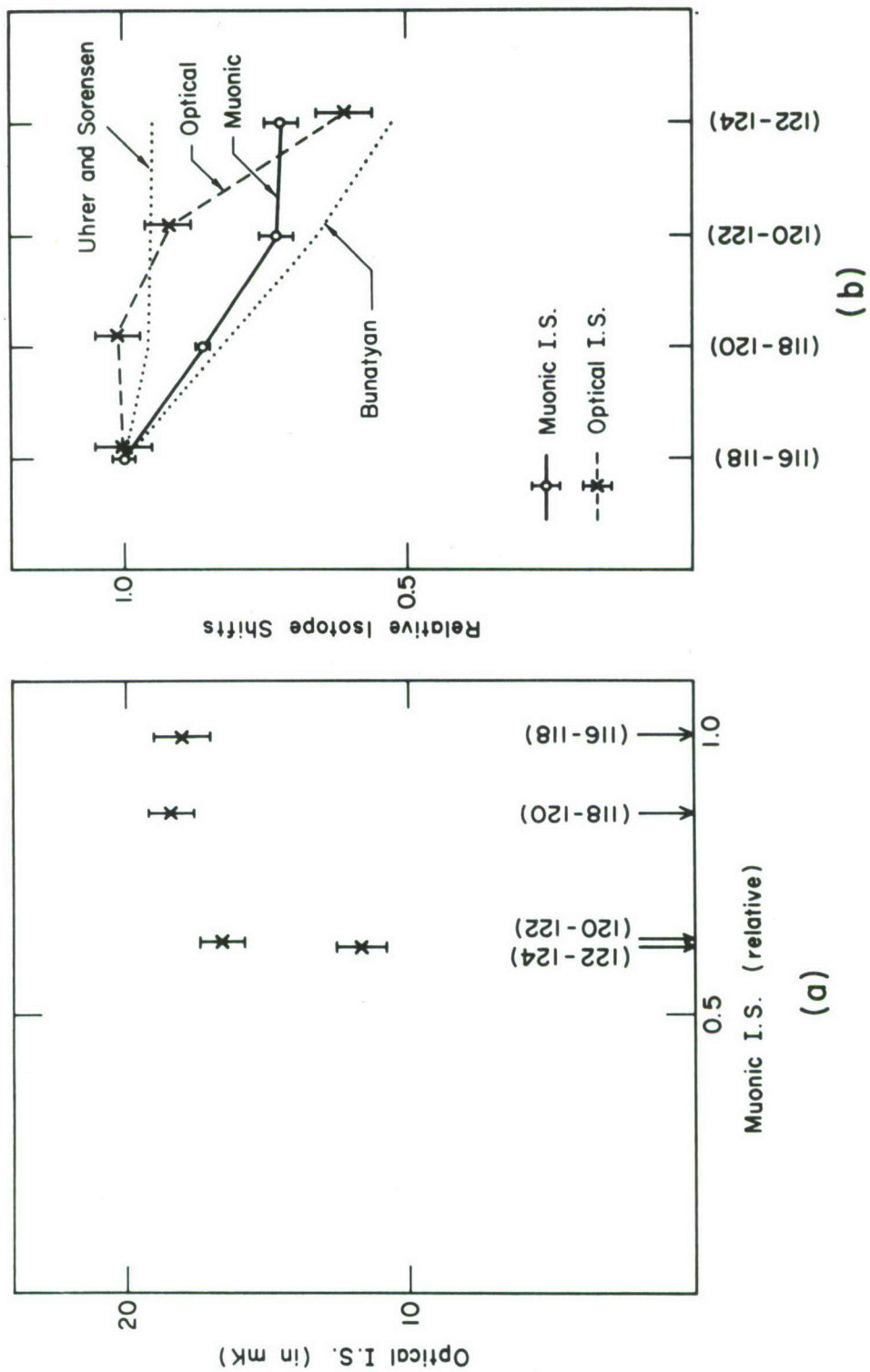


Figure IV.B.2.



### C. Isotope Shifts in Barium

We have measured isotope shifts in the muonic K lines of  $^{136}\text{Ba}$ ,  $^{137}\text{Ba}$  and  $^{138}\text{Ba}$ . The barium isotopes are especially interesting because shell closure effects are expected at  $N = 82$  ( $^{138}_{56}\text{Ba}$ ). Such effects have been observed by our group at  $N = 28$  in the chromium isotopes (see Progress Report NYO-72-191) and by the Chicago group at  $N = 50$  in the strontium isotopes.

Due to a slightly asymmetrical line shape, the analysis was carried out by fitting a modified gaussian function to the X-ray lines. In the case of  $^{137}\text{Ba}$ , the E2 and M1 interactions are strong enough to broaden the lines. In order to determine the center of gravity of these lines the hfs was calculated in the manner explained in a subsequent section, E. The M1 hfs constant  $A_1$  of the  $2p_{1/2}$  and  $2p_{3/2}$  levels has small values (0.10 keV and 0.08 keV, respectively). These values were fixed in our analysis, whereas the  $A_1$  value for the  $1s_{1/2}$  level and the value of the E2 hfs constant  $A_2$  for the  $2p_{3/2}$  level were determined from the best fit to the muonic data.

The isotope shifts were determined with the following considerations:

1. The reduced mass effect (0.02 keV/neutron) has been subtracted.
2. Differences in the Lamb shift and vacuum polarization between isotopes are small and assumed to be negligible.

3. Differences in nuclear polarization between isotopes may be of the order of 0.1 keV per neutron pair. However, there is no reliable way to determine this term, which has therefore been neglected.

4. Corrections have been made for isotopic impurities.

Our results are presented in Table IV.C.1. We have calculated the ratio of the measured isotope shift to the standard shift (the shift calculated for a uniform nuclear charge distribution with radius  $R = 1.2A^{1/3}$  fm). The small values of this ratio indicate a large shell closure effect; in effect, the nuclear size increases much less upon addition of two neutrons to fill the  $N = 82$  shell than beyond the shell. Moreover, the odd-even staggering effect is very large; the odd-even staggering parameter

$$\gamma_N = \frac{\delta E(136,137)}{1/2 \delta E(136,138)}$$

is almost zero,

$$\gamma_N = -0.02 \pm 0.40$$

D. Isotone Shift in Muonic X-Rays in the Tin Region (Reported at the Boulder Meeting of the Nuclear Physics Division, American Physical Society)

Section IV.C. described the isotope shift in muonic X-rays, that is, the change in the K X-ray energy due to a change in nuclear size from one isotope to the next. Similarly, the change in K X-ray energy between two isotones, which we might call the isotone shift,

Table IV.C.1.

Isotope Pair	$\delta E_{\text{field}}$	$\delta E_{\text{field}}/\delta E_{\text{std}}$			
		This Paper	Ref. a	Ref. b	Ref. c
136 - 138	$3.17 \pm 0.40$	$0.27 \pm 0.04$	$0.26 \pm 0.06$	$0.15 \pm 0.05$ $0.69 \pm 0.14$	$0.276 \pm 0.018$
136 - 137	$-1.01 \pm 0.70$	$-0.15 \pm 0.10$	$-0.01 \pm 0.12$	$-0.36$	$0.00 \pm 0.05$

a. O. I. Sumbaev, Prov. Of Dubna Symposium on Nuclear Structure (1968).

b. Kalitjesky, Fradkin, Izv. Akad. Nauk., SSSR Ser. Fiz. 25, 1178 (1961) (Optical Isotope Shifts).

c. A. C. Thompson, Thesis (1969) Carnegie-Mellon University (muonic X-ray Isotope Shifts).

will give us information on the change in nuclear size when protons are added to the nucleus.

Isotope shift studies have shown that in general, as neutrons are added to the nucleus, the increase in the nuclear charge radius is less than that predicted by the  $A^{1/3}$  law. Furthermore there are pronounced shell closure and deformation effects as shown on the Brix Kopfermann diagram. It is thus interesting to study the change in nuclear size produced by the addition of protons rather than neutrons.

The isotone shift,  $\Delta E_{\text{isotone}}$ , is defined as the change in the K X-ray energy when one or two protons are added to the nucleus:

$$\Delta E_{\text{isotone}} = E_k(Z + Z, N) - E_k(Z, N)$$

However, more than 90% of this shift is due not to a change in size, but merely to the change in  $Z$ . In order to obtain a model independent quantity which is directly related to the change in size, we calculate  $\Delta E_Z$  which is the change in energy when the second isotone has exactly the same size as the first, that is, for example, for a Fermi distribution, if the second isotone has the same  $c$  and  $t$ . The difference  $\Delta E_{\text{field}}$  between the experimentally observed shift and  $\Delta E_Z$  is then the change in energy due to the change in size:  $\Delta E_{\text{field}} = \Delta E_{\text{isotope}} - \Delta E_Z$ .

The quantity  $\Delta E_Z$  is quite sensitive to the size of the initial charge distribution; however, by fitting a Fermi distribution to the K and L X-rays of the first isotone one can calculate  $\Delta E_Z$  quite accurately, probably to about  $\pm 0.3$  keV out of 200 keV. The main



uncertainty in  $\Delta E_Z$  is probably due to nuclear polarization corrections.

The fact that the isotone shift must be measured over a much larger energy region than the isotope shift serves to increase the error in its measurement. Combined with the error in  $\Delta E_Z$ , this results in an error for  $\Delta E_{\text{field}}$  of several times what one would get for the isotope effect where there is no shift due to  $Z$ .

Table IV.D.1. lists our results for four isotone pairs in the tin region.  $Z = 50$  is a magic number and we expect to see shell closure effects as have been observed in the isotope shift for  $N = 50$ .

The measured isotone shifts are listed in the first row. Note that due to the variation of fine structure splitting with  $Z$  different shifts are observed in the  $K_{\alpha 1}$  and  $K_{\alpha 2}$  lines. The shifts are the averages of the differences in the full energy and double escape peaks. We used our standard computer controlled, stabilized data taking system, recording muonic data and calibration gamma rays simultaneously. Energies were determined by fitting a quadratic calibration curve to the 6 or 7 gamma lines of the calibration spectrum. For the even-even isotone pairs, both targets were run together and recorded in the same spectrum to avoid systematic errors.

For the two even-even pairs  $^{114}\text{Cd}$  to  $^{116}\text{Sn}$  where  $Z$  goes from 48 to 50 and  $^{124}\text{Sn}$  to  $^{126}\text{Te}$  where  $Z$  goes from 50 to 52 we notice immediately a large difference in the measured shift.

The  $Z$  dependent shift  $\Delta E_Z$  was calculated for a Fermi distribution

Table IV.D.1.

	$^{114}_{48}\text{Cd} - ^{115}_{49}\text{In}$		$^{114}_{48}\text{Cd} - ^{116}_{50}\text{Sn}$		$^{124}_{50}\text{Sn} - ^{126}_{52}\text{Te}$		$^{126}_{52}\text{Te} - ^{127}_{53}\text{I}$	
	$K_{\alpha 1}$	$K_{\alpha 2}$	$K_{\alpha 1}$	$K_{\alpha 2}$	$K_{\alpha 1}$	$K_{\alpha 2}$	$K_{\alpha 1}$	$K_{\alpha 2}$
Measured Isotone Shift $\Delta E_{\text{exp}}$	102.4 $\pm$ 0.5	99.0 $\pm$ 0.6	200.7 $\pm$ 0.4	195.2 $\pm$ 0.5	184.8 $\pm$ 0.4	178.6 $\pm$ 0.5	93.7 $\pm$ 0.4	89.3 $\pm$ 0.6
Z Dependent Shift $\Delta E_z$	103.4	100.4	207.3	201.2	206.5	199.9	102.4	98.5
Field Effect $\Delta E_{\text{field}}$ $E_{\text{field}} = \Delta E_{\text{exp}} - \Delta E_z$	-1.0	-1.4	-6.6	-6.0	-21.8	-21.3	-8.7	-9.2
Standard $A^{1/3}$ Size Effect $\Delta E_{\text{std}}$	-4.2	-4.2	-8.9	-8.7	-9.0	-8.9	-4.7	-4.6
$\Delta E_{\text{field}}/\Delta E_{\text{std}}$	0.24	0.33	0.74	0.69	2.42	2.39	1.85	2.00

All energies in keV

fitted to the isotone of lower  $Z$ . It includes vacuum polarization, Lamb shift, and an estimate of the nuclear polarization.

The shift due to change in size  $\Delta E_{\text{field}}$  is listed in the third row, and the standard shift, based on a Fermi distribution in which  $c = r_0 A^{1/3}$  is in the fourth row. The ratio of the measured field effect shift to the standard shift is given in the last row.

Fig. IV.D.1. is a plot of this ratio  $\Delta E_{\text{field}}/\Delta E_{\text{std}}$  as a function of  $A$  for the isotone shifts measured and also a few sample isotope shifts. The error bars take into account only experimental errors and not the error in  $\Delta E_Z$ .

We notice immediately the substantial difference as we compare closing the shell at  $Z = 50$  ( $^{114}\text{Cd} - ^{116}\text{Sn}$ ) with adding two protons beyond the shell ( $^{124}\text{Sn} - ^{126}\text{Te}$ ). Since the isotope shift averages about half of the expected value and yet we know that along the line of stability the radius does follow the  $A^{1/3}$  law, we might expect the average isotone shift to be about 1.6 times the standard. It is less than half this value for closing the shell and about 50% greater when protons are added outside the closed shell.

The isotope shift ratios here all lie below 1.0 and average to about 0.5.

The shifts involving odd-even isotones are subject to greater uncertainties because there may be substantial differences between the nuclear polarization corrections for the two isotones. The values used were interpolated from values for only a few isotopes and did not

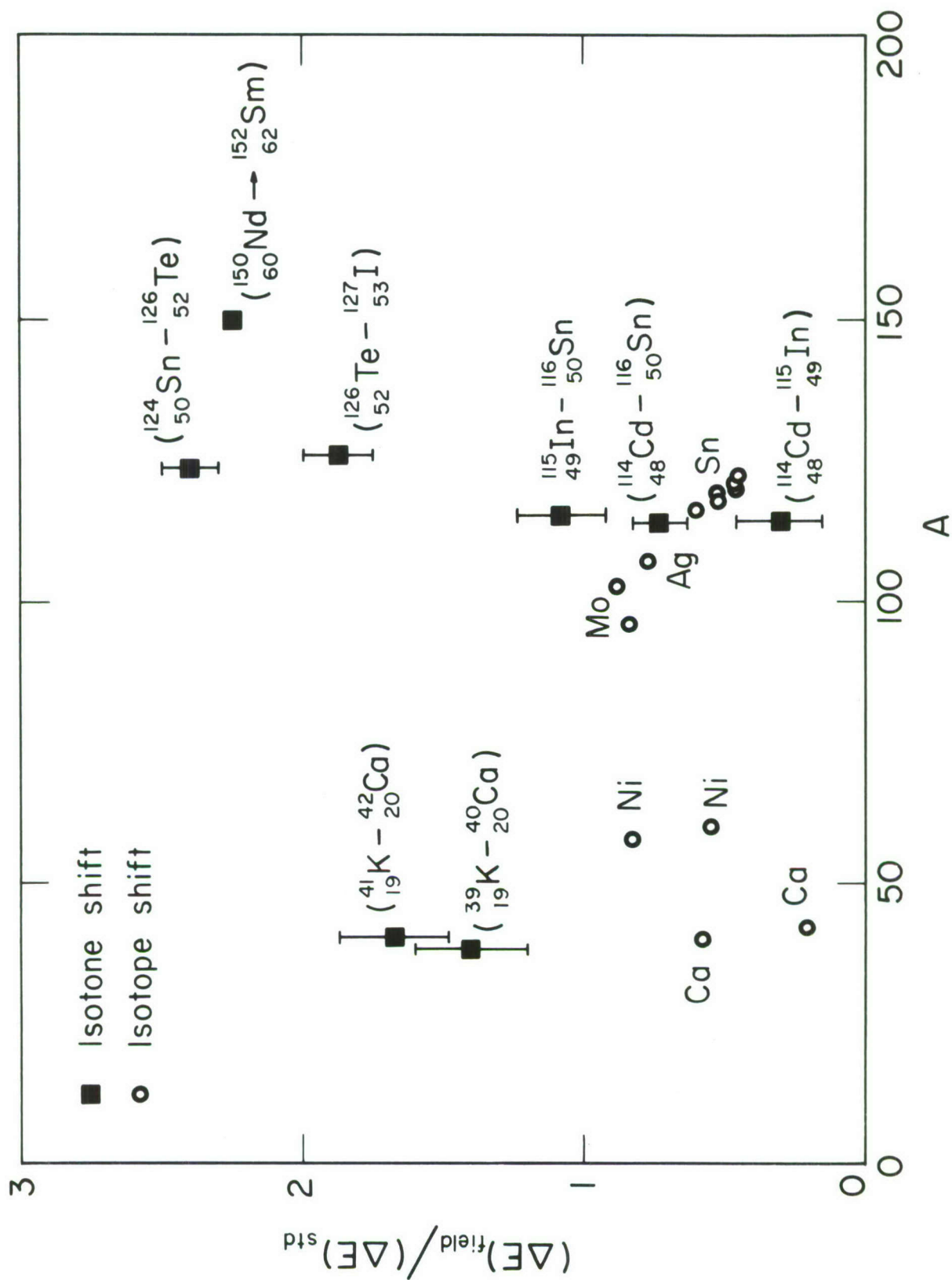


Figure IV.D.1.1.



take into account specific differences in the nuclear levels of the isotones. The difference between isotones amounted to only about 0.07 keV per proton out of a total correction of about 2.5 keV.

It is interesting to note, though, that while the shift from  $^{114}\text{Cd}$  to  $^{115}\text{In}$  is very small, if we use instead the shift from  $^{115}\text{In}$  to  $^{116}\text{Sn}$  where we are adding a proton to close the shell this is considerably larger, though still smaller than the average of 1.6 times the standard that we might expect if there were no differences in structure. Now the Chicago group looked at the isotone shift in closing the shell at  $Z = 20$  as shown in the K to Ca shift and did not see any effect of the shell closure. If a similar effect occurs there, the shift from  $Z = 18$  to  $Z = 19$  might be small. It would be interesting to investigate this region more closely and also the region around  $Z = 28$ .

E. Finite Distribution of Nuclear M1 and E2 Moments in Muonic  $^{115}\text{In}$ ,  $^{133}\text{Cs}$  and  $^{141}\text{Pr}$  (Phys. Rev. Letters 23, 648 (1969))

The distribution of nuclear M1 and E2 moments in the nuclei  $^{115}\text{In}$ ,  $^{133}\text{Cs}$  and  $^{141}\text{Pr}$  have been investigated by observing the hfs of their muonic X-ray spectra. As pointed out by Johnson and Sorenson<sup>(1)</sup>, the nuclear magnetism arising from the orbital motions is concentrated closer to the center of the nucleus, while the spin magnetism is more highly localized at the positions of the individual

---

<sup>1</sup>J. Johnson and R. A. Sorenson, Phys. Letters 26B, 700 (1968).

nucleons and tends to be more uniform. Our results are listed in Table IV.E.1. The reductions of the values of  $A_1(1s_{1/2})$  from their point-dipole values for all three nuclei studied are apparent.

We note that in all cases the configuration mixing model represents a substantial improvement over the point-dipole and the single particle models. This results mostly from the admixture of configurations whose magnetism is concentrated closer to the surface of the nucleus, i.e., spin magnetism. The theoretical values in Table IV.E.1. are quoted from Johnson and Sorenson.<sup>(1)</sup>

Only in the  $2p_{3/2}$  state of indium is the E2 hfs constant large enough to be measured with precision. The experimental value  $A_2(2p_{3/2}) = 2.55$  keV is in fair agreement with the theoretical value  $A_2 = 2.79$  keV computed using a surface quadrupole distribution, provided the spectroscopic quadrupole moment is taken as  $Q_{\text{spec}} = 0.834$  barns. We chose this value in preference to the value 1.16 barns found in the Table of Isotopes<sup>(2)</sup>, since the measured atomic beam value<sup>(3)</sup> is subject to corrections due to mixing of electronic configurations.<sup>(4)</sup> Such polarization corrections, of which

---

<sup>1</sup>J. Johnson and R. A. Sorenson, Phys. Letters 29B, 420 (1969) and Bull. Am. Soc. 14, 539 (1969).

<sup>2</sup>C. M. Lederer, J. M. Hollander and I. Perlman, Table of Isotopes, Wiley, 1967.

<sup>3</sup>A. K. Mann and P. Kusch, Phys. Rev. 78, 615 (1950).

<sup>4</sup>G. Koster, Phys. Rev. 86, 148 (1952); H. L. Acker et al., Nucl. Phys. 87, 1 (1966).

TABLE IV.E.1.1.

Isotope	State	hfs Constant	(Nuclear Moment Value)	Experimental Value of hfs Constant (keV)	Point-dipole or Surface Quadrupole Model (keV)	Single Particle Model (keV)	Configuration Mixing Model (keV)	BCS Model (keV)
<sup>115</sup> In	1s <sub>1/2</sub>	A <sub>1</sub>	(μ=5.535 nm)	1.65 ± 0.07	2.53	1.88	1.56	1.56
	2p <sub>1/2</sub>	A <sub>1</sub>		0.55 ± 0.13	0.64	0.56	0.46	0.46
	2p <sub>3/2</sub>	A <sub>2</sub>	(Q=0.834 b)	2.55 ± 0.10	2.79			
<sup>133</sup> Cs	1s <sub>1/2</sub>	A <sub>1</sub>	(μ=2.579 nm)	1.11 ± 0.18	1.34	0.91	1.21	1.15
	2p <sub>1/2</sub>	A <sub>1</sub>		0.50 ± 0.20	0.41	0.28	0.38	0.36
	2p <sub>3/2</sub>	A <sub>2</sub>	(Q=0.003 b)		0.01			
<sup>141</sup> Pr	1s <sub>1/2</sub>	A <sub>1</sub>	(μ=4.28 nm)	1.53 ± 0.15 (1.52 ± 0.07) <sup>(a)</sup>	2.38	1.62	1.47	1.47
	2p <sub>1/2</sub>	A <sub>1</sub>		0.62 ± 0.20	0.80	0.60	0.54	0.54
	2p <sub>3/2</sub>	A <sub>2</sub>	(Q=-0.06 b)		-0.45			

(a) See reference 9.

Sternheimer<sup>(1)</sup> corrections are an example, considerably decrease the confidence and precision with which nuclear quadrupole moments are known. The muon, in this case the  $2p_{3/2}$  muon is sensitive to the details of the distribution of the E2 moment, and its interaction with this distribution can be accurately calculated. This suggests that muonic atoms may provide a means of testing Sternheimer as well as other types of electronic polarization corrections for nuclear quadrupole moments.

F. The Resonance Process and the Intensity Anomaly in Muonic  $^{127}\text{I}$  (Reported at the Boulder Meeting of the Nuclear Physics Division, American Physical Society)

It has been known for some time that the intensity ratio between the  $(2p_{3/2} - 1s_{1/2})$  and  $(2p_{1/2} - 1s_{1/2})$  muonic X-rays for  $^{127}\text{I}$  is anomalously smaller than the theoretical value 1.95. Several theorists<sup>(2)</sup> have suggested that this may be explained by nuclear resonance excitation. We have observed the muonic N, M, L and K X-rays from  $^{127}\text{I}$ , and have calculated a theoretical spectrum within the framework of a resonance process. The resonance is between the 2p fine structure splitting and the nuclear ground and the first excited states. A satisfactory fit to the experimental data has

---

<sup>1</sup>R. M. Sternheimer, Phys. Rev. 105, 158 (1957 and earlier papers).

<sup>2</sup>H. L. Acker, G. Backenstoss, C. Daum, J. C. Sens and S. A. De Wit, Nucl. Phys. 87, 1 (1966); W. B. Rolnick, Phys. Rev. 132, 110 (1963); J. Hufner, Phys. Letters 25B, 189 (1967).



been obtained (see Figure IV.F.1.). From this fit we have determined the M1 and E2 hfs constants for the 1s and 2p states, and have obtained a quantitative interpretation of the observed intensity ratios.

The theoretical spectrum was calculated for an initial choice of the values of the parameters: the 3d and 2p fine structure splittings, the E2 and M1 transition moments, and the hfs constants  $A_1$  and  $A_2$  of the 2p and 3d states. These parameters were varied until a best fit (minimum  $\chi^2$ ) to the data was obtained. We have assumed that the 3d states were statistically populated, and have not taken into account the effect of excitation to nuclear states higher than the first. The analysis of our data including the "nuclear polarization" effect is in progress.

The hfs constants determined are listed in Table IV.F.1. The values of  $A_1(1s_{1/2})$  and  $A_1(2p_{1/2})$  are noticeably smaller than the values calculated for a point-dipole and a single particle model. Also the  $A_2(2p_{3/2})$  value is smaller than that calculated for a surface distribution of the quadrupole moment. The predictions of various nuclear models are quoted from Johnson and Sorenson<sup>(1)</sup>

The intensity ratios are given in Table IV.F.2. The theoretical values (with the resonance) were calculated from the set of parameters which gave the best fit to our data. We see that the intensity anomaly can be quantitatively interpreted.

---

<sup>1</sup>J. Johnson and R. A. Sorenson, Phys. Letters 29B, 420 (1969) and Bull. Am. Phys. Soc. 14, 538 (1969).

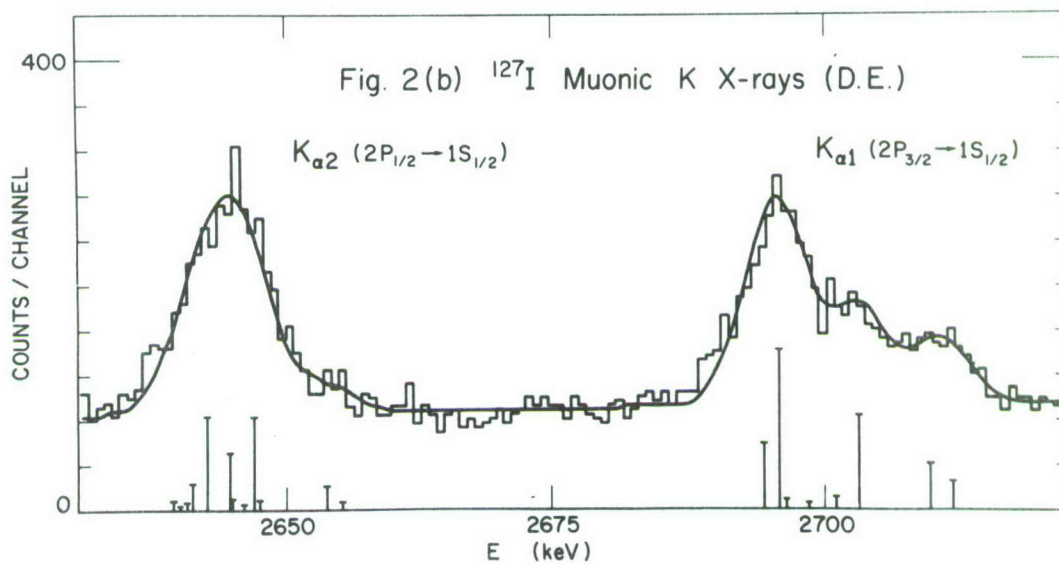
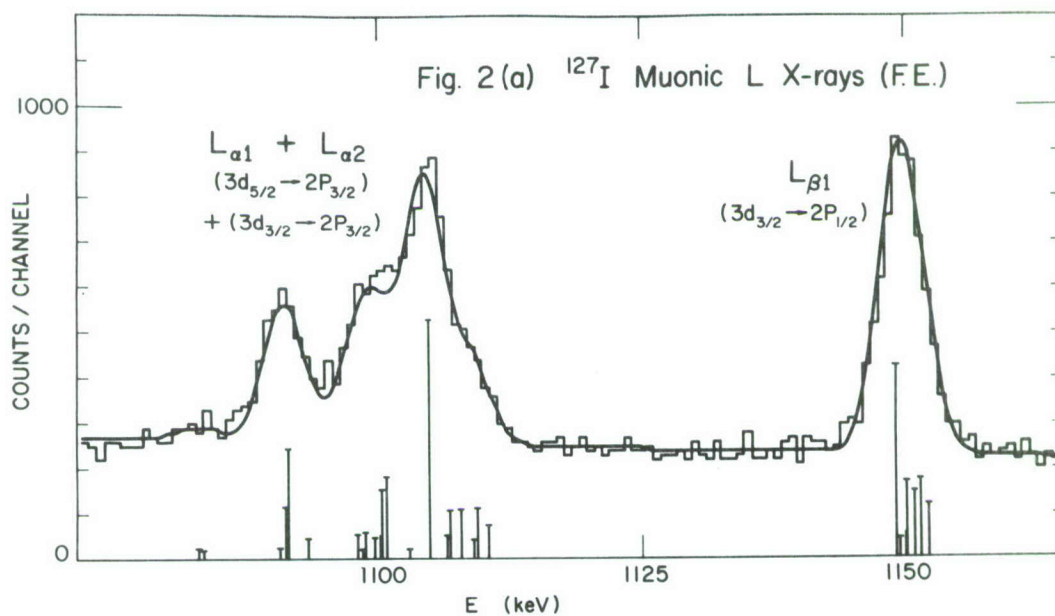


Figure IV.F.1.

TABLE IV.F.1.

hfs Constants	Experimental Columbia 1969	Point Dipole	Surface Quadrupole	Arima Horie	BCS + $\delta$	BCS + $\delta$ + phonon	BCS + $\delta$ + phonon, GR+Z/A	Single particle
$A_1(S_{1/2})$	$0.87 \pm .09$	1.40	-	0.95	0.94	(GR = 0) 0.928	1.11	1.50
$A_1(P_{1/2})$	$0.33 \pm .08$	0.40	-	0.298	0.296	0.293	0.354	0.48
$A_1(P_{3/2})$	$0.18 \pm .05$	0.22	-					
$A_1(D_{3/2})$	$0.045 \pm .005$	0.045	-					
$A_1(D_{5/2})$	$0.030 \pm .005$	0.031	-					
$A_2(P_{3/2})$	$-2.87 \pm .01$	-	-3.15					
$A_2(D_{3/2})$	$-0.251 \pm .008$	-	-0.255					
$A_2(D_{5/2})$	$-0.377 \pm .010$	-	-0.383					

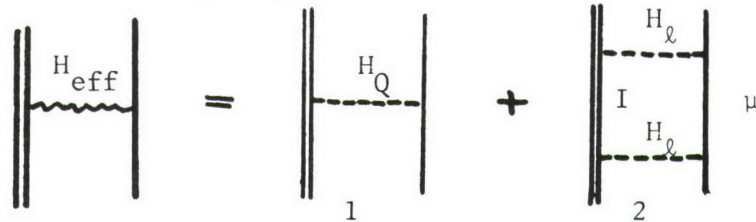
TABLE IV.F.2. Intensity Ratios

Ratio	Experimental		Theoretical	
	Columbia '69	CERN '66	With resonance	Without Resonance
$\frac{(2p_{3/2}-1s_{1/2})}{(2p_{1/2}-1s_{1/2})}$	1.10±0.08	1.06±0.08	1.18±0.10	1.95
$\frac{(3d_{5/2}-2p_{3/2})+(3d_{3/2}-2p_{3/2})}{(3d_{3/2}-2p_{1/2})}$	1.93±.09	3.0±0.50	1.83±0.10	1.95



G. Nuclear Polarization in Deformed Nuclei (Reported to the Third International Conference on High Energy Physics and Nuclear Structure, Columbia University, Sept. 8-12, 1969, and to the Boulder Meeting of the Nuclear Physics Division, American Physical Society)

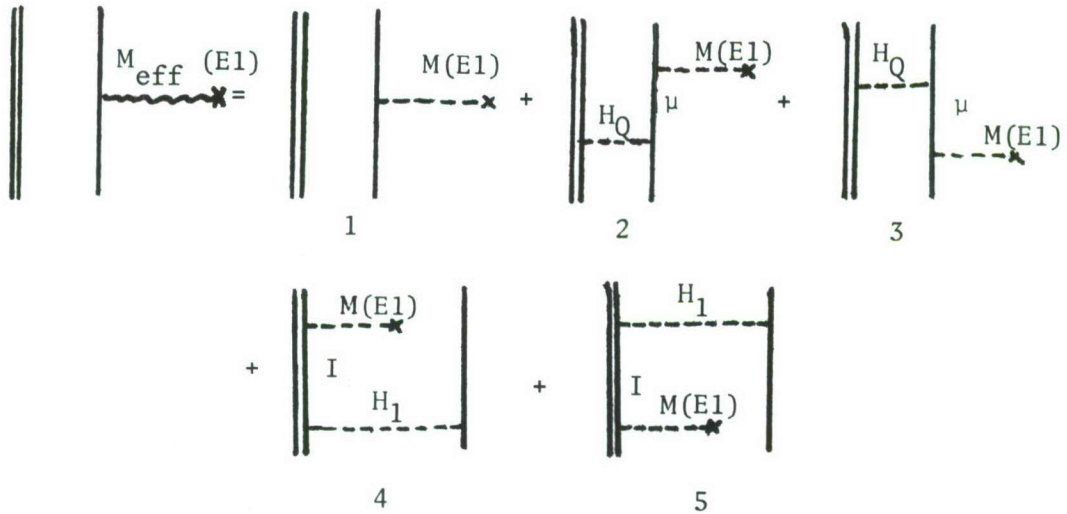
The analysis of muonic X-ray spectra in heavy deformed nuclei has been carried out in the past by diagonalizing the electric quadrupole interaction  $H_Q$  between the muonic spin doublets  $(2p_{3/2}, 2p_{1/2})$ ,  $(3d_{5/2}, 3d_{3/2})$  and the ground state rotational band of the nucleus. To take into account the muonic and nuclear states not included in the diagonalization, we introduce the effective quadrupole interaction  $H_{\text{eff}}$  by virtual excitations into those states, as shown in the following diagram:



where  $I$ ,  $\mu$  are nuclear and muonic intermediate states respectively, and  $H_\ell$  is the electrostatic interaction. Graph IV.G.1. represents the quadrupole interaction which has been taken into consideration in the past, and Graph IV.G.2. represents the corrections. We find the off-diagonal matrix elements of Graph IV.G.2. are always proportional to the corresponding elements of Graph IV.G.1.; therefore, the inclusion of those elements is equivalent to a renormalization of the intrinsic quadrupole moment of the nucleus. The renormalization constant is calculated to be 1.03 - 1.05. The diagonal matrix

elements of Graph IV.G.2. are always negative, which increases the binding of the 1s and 2p states.

In calculating the intensity ratios of the hyperfine multiplats, we introduce the effective E1 transition element  $M_{\text{eff}}(E1)$  by the following diagram



Graph IV.G.1. represents the E1 transition matrix elements which have been used in the past. Graphs IV.G.2. and IV.G.3. take into account the higher muonic levels which have previously been neglected. Graphs IV.G.4. and IV.G.5. represent the mixing of the giant dipole states. The inclusion of the above corrections in the analysis of the experimental spectra has a profound influence on the results. The above theoretical calculations have been applied to our analysis of the h.f.s. of the muonic X-rays from deformed nuclei (see section IV.H.)

H. Parameters of the Charge Distribution of Deformed Nuclei  
(Reported to the Third International Conference on High  
Energy Physics and Nuclear Structure, Columbia University,  
Sept. 8-12, 1969)

Precise measurements, using a stable high resolution Ge(Li) spectrometer have been made of the K (2p - 1s) and L (3d - 2p) muonic X-ray spectra of eight even-even rare-earth nuclei:  $^{150}\text{Nd}$ ,  $^{152}\text{Sm}$ ,  $^{162}\text{Dy}$ ,  $^{164}\text{Dy}$ ,  $^{168}\text{Er}$ ,  $^{170}\text{Er}$ ,  $^{182}\text{W}$ ,  $^{184}\text{W}$  and  $^{186}\text{W}$ .<sup>(1)</sup> From these measurements values of the parameters of the nuclear charge density

$$\rho(r) = \rho_0 \left[ 1 + \exp \frac{r - c[1 + \beta Y_{20}(\theta)]}{a} \right]^{-1}$$

have been determined.

In several different attempts to interpret our experimental results, we have come to appreciate how sensitive the conclusions are to the precision of the theoretical corrections. These include the Lamb Shift and, more important, the nuclear polarization corrections. Nuclear polarization is the effect of all interactions which induce mixing of different muon and nuclear states. The dynamic E2 hyperfine spectra<sup>(2)</sup> can also be considered as a part of the nuclear polarization due to the quadrupole interaction.

---

<sup>1</sup>D. Hitlin, S. Bernow, S. Devons, I. Duerdoth, J. W. Kast, E. R. Macagno, J. Rainwater, K. Runge, C. S. Wu and R. C. Barrett, Proceedings of the International Conference on Electromagnetic Sizes of Nuclei, Ottawa, 1967, and D. Hitlin, Thesis, Columbia University, 1968.

<sup>2</sup>L. Wilets, Dan. Mat. Fys. Medd. 29, #3 (1954); B. A. Jacobsohn, Phys. Rev. 96, 1637 (1954).

Recently M. Y. Chen has extended nuclear polarization calculations in deformed nuclei to include states other than the lowest muonic and nuclear states. Before this improved nuclear polarization correction was made, the most unsatisfactory feature of the results was the very small value of the skin thickness obtained. In addition the value of the quadrupole moment was larger than that derived from Coulomb excitation measurements, and it was not possible to obtain a reasonable fit to the relative intensities of the K and L X-rays. In order to bring the quadrupole moment obtained from the h.f.s. spectrum into agreement with that obtained from Coulomb excitation, the skin thickness was assumed to be a function of the polar angle:  $a' \rightarrow a(1 + \beta'Y_{20})$ . For the nuclei studied a best fit to the data was obtained with rather large negative values of the  $\beta'$  parameter, implying that the nuclear charge distribution was more diffuse at the "equator" ( $\theta = 90^\circ$ ) than at the poles ( $\theta = 0^\circ$ ). With this four-parameter model the average skin thickness was still unusually small, however, and there was no improvement in the fit to the intensities.

When the improved nuclear polarization corrections are applied, the skin-thickness of the three parameter distribution is increased to about 2.2 F., a value similar to that obtained for neighboring spherical nuclei. At the same time the quadrupole moment agrees with the Coulomb excitation result and a better fit is obtained to the relative intensities of the X-rays. The



hyperfine results for deformed nuclei are summarized in Table IV.H.1. In section a) only the nuclear polarization in the "model space" is calculated resulting in the large negative values for  $\beta'$ . The average value of  $t$  ( $= 4\log 3a$ ) is 1.6 F, and the  $\beta'$  parameter is no longer needed. In sections b) and c) the CERN and Carnegie-Mellon-Argonne-Binghampton results are listed.<sup>(1)</sup> Their analyses did not include nuclear polarization corrections and the skin-thicknesses which they obtained are seen to be unusually small.

Our analysis illustrates the extreme importance of applying precise nuclear polarization corrections in interpreting muonic X-ray data. It appears that the three-parameter deformed Fermi distribution is adequate to describe the charge densities at present.

I. Muon and Pion Induced Fission of Uranium Isotopes  
(Phy. Rev. Letters 24, 604 (1970))

The capture of a pion near the nuclear surface results in a deposition of approximately 80 MeV of excitation energy in the nucleus. Emulsion studies, on the absorption of slow pions by  $^{238}\text{U}$  nuclei, have shown that the subsequent fission process is predominantly a symmetric division of the nucleus. Muons can also induce fission by being captured from a 1s orbit. In this case, however, most of the  $\mu$  rest mass is carried off by a neutrino and

---

<sup>1</sup>S. A. DeWitt, G. Backenstoss, C. Daum, J. C. Sens and H. L. Acker, Nucl. Phys. 87, 657 (1967); R. A. Carrigan, Jr., P. D. Gupta, R. B. Sutton, M. N. Suzuki, A. C. Thomson, R. E. Cole, W. Y. Prestwich, A. K. Gaigalas, and S. Raboy, Bull. Am. Phys. Soc. 13, 65 (1968).

TABLE IV.H.1.

Parameters of the Charge-Distribution of Deformed Nuclei

Without Nuclear Polarization and Lamb Shift Corrections						With Nuclear Polarization and Lamb Shift Corrections, $\beta' = 0$ .				
a) Columbia (1)						a') Columbia (1)				
	c, fm.	t, fm.	$\beta$	$\beta'$	$Q_0$	c, fm.	t, fm.	$\beta$	$Q_0$	$(Q_0)_{C.E.}$
$^{150}\text{Nd}$	6.083	$1.68 \pm .02$	0.274	0	5.27	5.863	2.35	0.278	5.14	$5.17 \pm .12$
$^{152}\text{Sm}$	6.093	$1.77 \pm .02$	0.302	-0.22	5.85	5.900	2.37	0.296	5.76	$5.85 \pm .15$
$^{162}\text{Dy}$	6.26	$1.59 \pm .02$	0.337	-0.28	7.38	6.00	2.41	0.338	7.34	$7.12 \pm .12$
$^{164}\text{Dy}$	6.34	$1.30 \pm .03$	0.329	-0.12	7.53	6.02	2.41	0.340	7.44	$7.50 \pm .20$
$^{168}\text{Er}$	6.34	$1.51 \pm .02$	0.354	-0.92	7.77	6.17	2.17	0.332	7.75	$7.66 \pm .15$
$^{170}\text{Er}$	6.42	$1.26 \pm .03$	0.341	-0.87	7.80	6.27	1.95	0.325	7.71	$7.45 \pm .13$
$^{182}\text{W}$	6.47	$1.85 \pm .02$	0.272	-0.51	6.57	6.41	2.12	0.248	6.56	$6.58 \pm .06$
$^{184}\text{W}$	6.49	$1.84 \pm .03$	0.269	-0.78	6.19	6.39	2.23	0.238	6.27	$6.21 \pm .06$
$^{186}\text{W}$	6.55	$1.75 \pm .02$	0.243	-0.54	6.01	6.46	2.10	0.222	5.88	$5.93 \pm .05$
b) CERN (4)										
$^{159}\text{Tb}$	6.2	$1.5 \pm 0.4$	0.30		$7.6 \pm 0.4$					
$^{165}\text{Ho}$	6.27	$1.5 \pm 0.4$	0.30		$7.9 \pm 0.5$					
$^{181}\text{Ta}$	6.51	$1.5 \pm 0.4$	0.25		$7.5 \pm 0.4$					
$^{232}\text{Th}$	7.10	$1.49 \pm 0.14$	0.23		$9.8 \pm 0.3$					
$^{233}\text{U}$	7.11	$1.50 \pm 0.5$	0.24		$10.3 \pm 0.3$					
$^{235}\text{U}$	7.14	$1.44 \pm 0.17$	0.241		$10.6 \pm 0.2$					
$^{238}\text{U}$	7.15	$1.46 \pm 0.12$	0.253		$11.25 \pm 0.15$					
$^{239}\text{Pu}$	7.18	$1.35 \pm 0.3$	0.26		$12.0 \pm 0.3$					
c) Carnegie-Mellon-Argonne-Binghamton (5)										
$^{151}\text{Eu}$	6.27	$1.3 \pm 0.4$			2.75					
$^{153}\text{Eu}$	6.06	$1.78 \pm 0.4$			$7.01 \pm 0.10$					
$^{158}\text{Gd}$	6.33	0.714			7.15					
$^{160}\text{Gd}$	6.35	0.57			7.38					
$^{175}\text{Lu}$	6.24	$2.07 \pm 0.3$			$8.02 \pm 0.12$					
$^{232}\text{Th}$	7.07	1.75			11.3					
$^{238}\text{U}$	7.10	1.75			11.3					

Remarks: Argument of the Fermi charge distribution function:

$$\text{In a)} \quad \frac{r - c [1 + \beta Y_{20}(\theta)]}{a [1 + \beta' Y_{20}(\theta)]}; \quad \frac{r - c [1 + \beta Y_{20}(\theta)]}{a}$$

In b) and c)

$$\frac{r [1 + \beta Y_{20}(\theta)] - c}{a}$$

only about 15 MeV is left in the form of nuclear excitation energy.

In 1958 Zaretsky<sup>(1)</sup> pointed out that fission may be an alternative mode of de-excitation of a muonic atom. For heavy nuclei ( $Z > 90$ ) the energy of the  $2p - 1s$  muonic transition is roughly equal to the height of the fission barrier and to neutron binding energies in these nuclei. The muon may therefore transfer its excitation energy in a radiationless process producing an excited nucleus with a muon in a  $1s$  orbital. Both fission and neutron emission are open channels to the excited nucleus. The muon may either be captured or be internally converted by a heavy fission fragment. The emission of prompt neutrons without fission has recently been observed.<sup>(2)</sup> Zaretsky estimated that the ratio of  $\mu$ -capture induced fission to radiationless  $\mu$  de-excitation induced fission is about 4:1.

Our apparatus consisted of two banks of 400 mm silicon surface barrier detectors (Ortec 7904 series) between which thin targets of fissionable material could be placed. The target and detectors were placed in a brass cylinder 8 inches in diameter and 8 inches long that was closed at both ends by thin plates of aluminum and evacuated. A conventional beam telescope<sup>(3)</sup> signalled the stopping of a pion or a muon in the chamber. The pion and muon beams were

---

<sup>1</sup>D. F. Zaretsky, in Proceedings of the Second United Nations International Conference on the Peaceful Uses of Atomic Energy, (CERN Geneva, 1958)

<sup>2</sup>C. K. Hargrove, et al., Phys. Rev. Letters 23, 215 (1969).

<sup>3</sup>See, for example, T. T. Bardin et al., Phys. Rev. 160, 1043 (1967).



separated by inserting different thicknesses of aluminum absorber.

The pulses from the 24 detectors in both banks were fed to units that contained both charge sensitive and voltage sensitive preamplifiers. Fast pulses from the voltage sensitive preamplifiers connected to one bank were OR'd together, and could be put in coincidence with a pulse from any of the detectors in the other bank. A triple coincidence could then be established with a pulse from the beam telescope. The output of the final coincidence drove a gate generator that enabled one or more multichannel analyzers. For singles work, the fast outputs of both banks are first OR'd together.

A second output of the final OR unit was fed to the start input of a time-to-amplitude converter (TAC). The stop signal from the TAC is a delayed (300 ns) pulse from the beam telescope. The output of the TAC, corresponding to the time distribution of the arrival of fission fragments at the detectors, was stored in one of the 400 channel analyzers whose gating is described in the previous paragraph.

The slow pulses from the charge sensitive preamplifiers that contain the energy information were added together and stored in another gated 400 channel analyzer. Provision was also made in the logic design for observing the energy distribution of delayed fission events on a third analyzer.

All targets were in the form of a V with a right angle between the arms. Each arm had an area of 4 inches x 4 inches. Four distinctly different types of targets were used in the experiment.



Thin targets of  $^{235}\text{U}$  and  $^{233}\text{U}$  were prepared by electrospraying techniques.

Prior to a run the detectors with their individual charge sensitive preamplifiers were first calibrated on the  $\alpha$  particles from radioactive thorium or polonium sources. Then the resolution of the entire apparatus and associated electronics was determined by observing the neutron induced fission spectrum from the target to be run. In addition, the energy scale of the multichannel analyzer was calibrated with the aid of a  $^{252}\text{Cf}$  spontaneous fission source before and after each run.

In Figure IV.I.1. we show data obtained in the coincidence experiment on  $\pi$  induced fission. The fitted curve corresponds to a least-squares-fit to the data in which three Gaussian functions were allowed to vary in height, width and position. The center peak corresponding to symmetric fission dominates the pattern, has a width of roughly 22 MeV, and is centered at an energy of 57 MeV. The most probable energies of the heavy and light fragments from neutron induced fission in our target are 60 MeV and 84 MeV, respectively. These energies represent a degradation of the fission fragment energy in passing through the target material and/or the nickel backing. However, it is clear that the most probable energy of the two fragments following the capture of slow pions is considerably lower than the average energy for the capture of slow neutrons. A displacement of the peak corresponding to symmetric fission of  $^{238}\text{U}$  by protons of

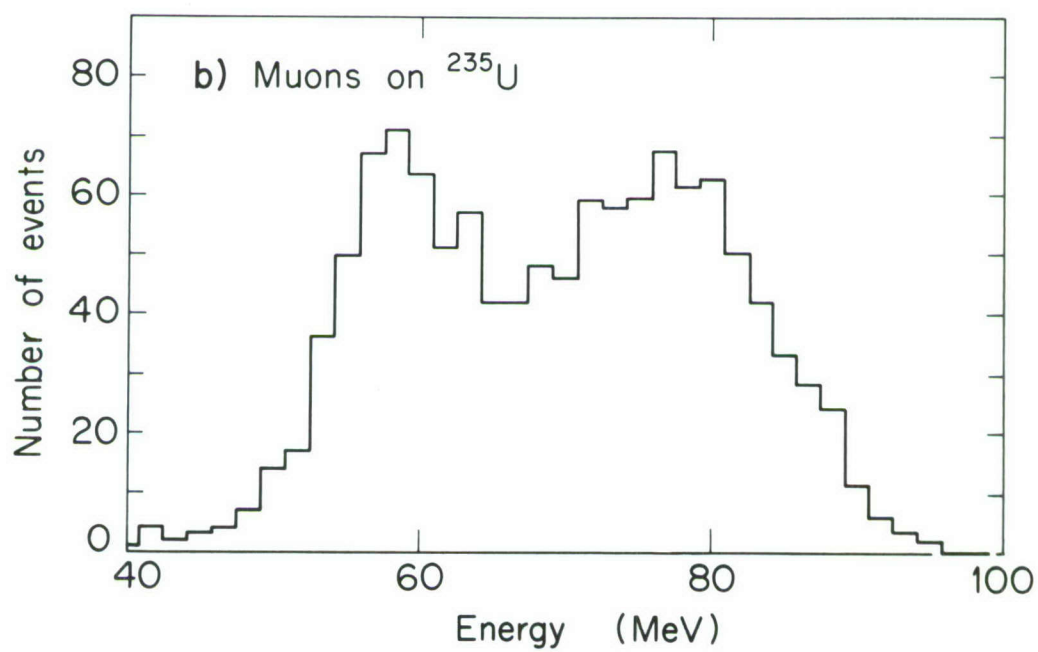
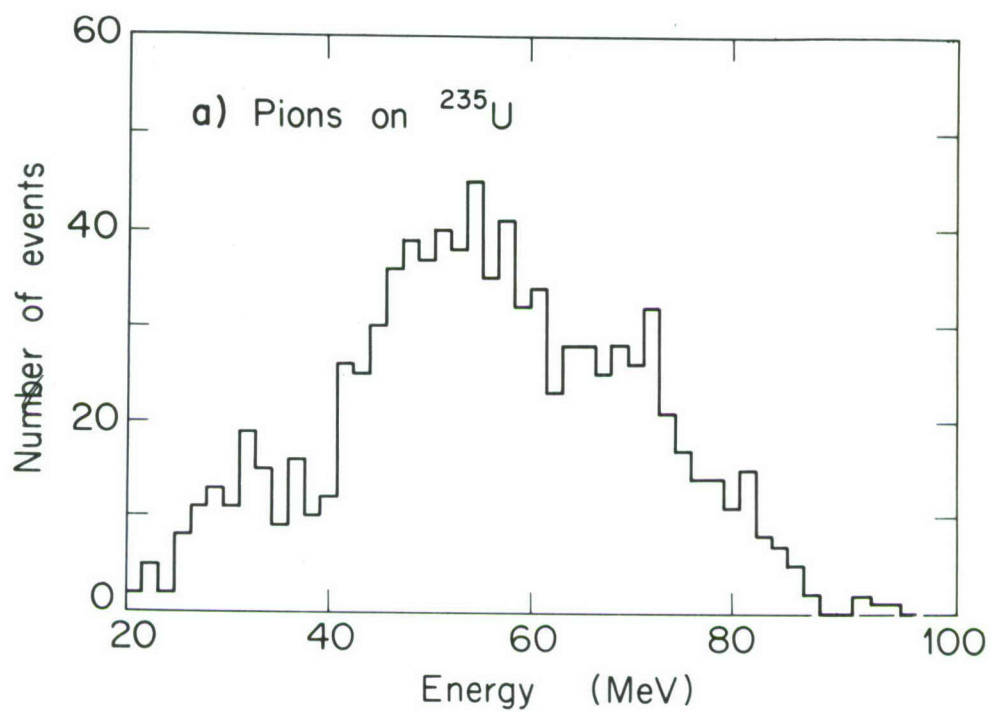


Figure IV.I.1.

156 MeV incident energy has also been observed.<sup>(1)</sup> On the other hand, our results indicate that muon induced fission is an asymmetric division of the nucleus. Although 15 - 20 MeV are available for nuclear excitation in the case of  $\mu$ -capture, no definite indication of an increased preference for symmetric fission was observed, compared to fission induced by slow neutrons. The two processes as observed for  $^{233}\text{U}$  and  $^{235}\text{U}$  are quite similar. Only the time distribution of the fission events can definitely tell them apart.

Table IV.I.1. summarizes the information we obtained on the time distribution of fission events after muons stopped in targets of all three isotopes. The decrease in mean life with decreasing mass number is easily comprehended in terms of the Primakoff Theory.<sup>(2)</sup> In fact, if the  $^{235}\text{U}$  result is taken as a normalization value, mean lives of 71.5 ns and 60.9 ns are predicted for  $^{238}\text{U}$  and  $^{233}\text{U}$ , respectively.

Fission events that originate from the radiationless transfer of energy from muonic atom to nucleus occur approximately  $10^{-13}$  seconds after the muon enters a high atomic orbit. These events manifest themselves as an excess of events in the first few bins of the time distribution, over and above the number expected from muon capture in the earliest time intervals. The small percentage of radiationless fission events observed in our experiment confirms

---

<sup>1</sup>L. Kowalski, thesis, University of Paris (1963).

<sup>2</sup>H. Primakoff, Rev. Mod. Phys. 31, 802 (1959).

TABLE IV.I.1.

Isotope	Mean Life (ns)		Radiationless Events $\mu$ -Capture Events	
	This Experiment	Earlier Work <sup>(a)</sup>	This Experiment	Earlier Work <sup>(a)</sup>
$^{238}\text{U}$	$74.1 \pm 2.8$	$75.6 \pm 2.9$	$0.048 \pm 0.025$	$0.072 \pm 0.022$
$^{235}\text{U}$	$65.3 \pm 2.8$	$66.5 \pm 4.2$	$0.063 \pm 0.025$	$0.111 \pm 0.021$
$^{233}\text{U}$	$6.17 \pm 3.8$		$0.046 \pm 0.030$	



the results of Diaz et al.<sup>(1)</sup> An explanation for the rarity of prompt events has been given by Zaretsky and Novikov.<sup>(2)</sup> The presence of the  $1s$  muon inhibits the fission process by raising the barrier by approximately  $0.1$  MeV. This is sufficient to decrease the fission probability by an order of magnitude.

---

<sup>1</sup>J. A. Diaz, S. N. Kaplan and R. V. Pyle, Nuc. Phys. 40, 54 (1963).

<sup>2</sup>D. F. Zaretsky and V. M. Novikov, Nuc. Phys. 28, 177 (1961).

V. NEUTRON INTERACTIONS WITH CONDENSED MATTER - T. I. Taylor,  
J. Markisz and W. W. Havens, Jr.

Without the availability of a reactor, the major part of the past year was devoted to the moving of the crystal spectrometer and its related components to the TRIGA reactor, reassembling it and getting it into operating condition. A baseplate was designed and built, which allowed the spectrometer to be assembled on a set of heavy duty casters so that it could easily be moved around while the reactor was inactive, and could be wheeled away from the reactor face with a minimum of time and effort, should that be necessary when the reactor is operating. An adjustment of four leveling screws and four bolts into a pair of I-beams are all that are necessary to detach the spectrometer physically from the face of the reactor. The adjustable collimator from the Brookhaven Graphite Research Reactor, which had been used in conjunction with the crystal spectrometer, was pulled from that reactor and brought into Columbia after sufficient decontamination. Suitable shielding and adapting apparatus are being constructed. Shielding for the entire spectrometer, along with mounting equipment, is being constructed.

Calculations of cross sections from data taken on methane, ethane, dimethylacetylene, and methylammonium chloride before the closing of the Brookhaven Graphite Reactor have been completed and considerations have been given to additional measurements needed to complete the research when the facilities are available. Theoretical calculations of total cross sections as a function of temperature

have been continued with special emphasis on suitable models and equations for methane at the low temperatures.

Manuscripts have been prepared for publication of the results of measurements on polymers and related materials involving methyl groups and large molecules.

## VI. KINETICS OF NEUTRON AND PHOTON GASES

### A. Moments Solution to the Time-Independent Neutron Transport Equation - C. Weisbin, L. J. Lidofsky, and H. Goldstein

The moments code described in the last Progress Report (NYO-72-227, p. 81) has been made much more powerful and versatile with the addition of two major features during the past year. The first of these is a variable dimensioning technique which permits rapid generation of moments codes efficiently dimensioned in proportion to the input parameters of the problem. Where needed, it is possible for example, to use virtually the entire available core of Columbia's IBM 360/91 ( $\sim 1.2 \times 10^6$  bytes) for large scale transport calculations (e.g. one with 2,000 or more energy points). On the other hand, another version of the code can be prepared tailored to small scale investigations, e.g. involving only one element, elastic scattering only and, say, 200 energy points. The advantages in computing efficiency are obvious.

The second addition is the capability to read input cross section data directly from ENDF/B files. This provision is in line with the desire of the AEC to standardize on ENDF/B format for evaluated cross section data. In the sensitivity studies, the present "first round" sets of ENDF/B data are used for the initial calculations and as a point of departure for investigating the effects of cross section changes. (Our studies have had the incidental effect of revealing gross inadequacies in these "first-round" ENDF/B



evaluations of Be, Fe and Li at least as regards shielding calculations.

All of the series of programs related to the moments calculations have been linked together. It is, therefore, possible to carry out as a single computer "job", a calculation which starts with an ENDF/B tape of cross sections, introduces specified changes in these cross sections, computes the spatial moments of the spectrum, reconstitutes the flux from the moments, and finally produces tabulations and plots of the output results. Work has been also initiated to incorporate the recently acquired SEL computer into the input preparation and output analysis sections of the chain of moments-programs.

The investigation of neutron transport in beryllium oxide, previously reported, has been continued. Present indications are that the transport of fission neutrons is remarkably insensitive to variations in the cross section data within the uncertainty limits now known. In addition, similar calculations have been started for pure beryllium, for which the following preliminary results have been obtained:

	Fission source	14 MeV source
Fast effect	1.075	2.97
Age ( $\sim 1.4$ ev) $p = 1.85$ gm/cm <sup>3</sup>	73.68 cm <sup>2</sup>	144.18 cm <sup>2</sup>

The transport of neutrons in carbon under specified conditions of source and geometry had been proposed by the Radiation Shielding Information Center as a "benchmark" problem for shielding studies. Moments calculations for nearly identical conditions have therefore been carried out for carbon, and compared with previous discrete ordinates calculations (GGA) and Monte Carlo calculations (ORNL). The scalar flux so computed agrees with these other predictions to 10% or better, except in the highest energy group where the discrepancy is a factor of two. The source of discrepancy is presently being investigated.

The moments computational procedure as of June 1969, and preliminary results for BeO, have been described at length in a doctoral thesis (C. Weisbin) which has subsequently been issued as a report, NYO-268.

B. The Effect of Cross Section Fluctuations on Fast Neutron Transport - W. Preeg and H. Goldstein

The study of the effect of isolated minima in the total cross section (discussed in the previous report, p. 82) has been continued. A semi-quantitative model has been developed which agrees reasonably well with rigorous calculations in oxygen and iron. Neutrons born above the energy of the minimum are slowed down in the vicinity of the source; some fraction slow down into a small energy band centered around the exact minimum point. These, plus the source neutrons born in the band, then travel far either without collision or with only very small-angle elastic collisions. They then act as a virtual, nearly monoenergetic, source distributed through the medium. The

flux spectrum below the minimum is determined solely by local slowing down from this virtual source, irrespective of the nature of the actual source.

Where the cross section exhibits minima that are close together (relative, say, to  $\bar{\xi}$ ) and arise as the result of rapid but relatively shallow cross section fluctuations, the phenomena are more complex. Iron is a convenient nucleus for which these effects can be studied, as the fluctuations persist into the MeV range, and there are at least two high resolution measurements of the total cross section in this region (from Gulf General Atomic and Karlsruhe). By a series of moments calculations, ranging up to a "monster" 2500 energy point problem, it has been possible to show that the characteristics of the nucleus interactions at the minima of the total cross sections still determine the nature of the deep penetration. It appears important to include fluctuations in both the total and the differential elastic cross sections, but preliminary results seem to show fluctuations in the inelastic cross section are not significant.

In the usual multigroup transport calculation a single group may include 20 or so of these fluctuation minima. It is, therefore, important that the weighing spectrum used to calculate the multigroup cross sections should suitably emphasize the minima in the cross section. The customary  $1/E$  weighing with the GAM II group structure has been shown to give fluxes incorrect by a factor of 10 or more through 80 cm of iron. Various weighting "prescriptions"



have been developed, none of which gives exactly the correct result throughout the entire energy spectrum. However, it has been found that a weighting spectrum derived on the assumption that the collision density varies smoothly as  $1/E$  gives adequate accuracy and is a simple recipe to apply.

The investigations summarized here will be described at length in a doctoral thesis by W. Preeg.

C. Reconstruction of the Spatial Dependence of the Flux from the Spatial Moments - P. Soran, H. Goldstein, and L. J. Lidofsky

Various ideas for obtaining a continuous spatial dependence from a knowledge of a discrete number of moments have been examined exhaustively. The only new techniques to have survived and proven useful are the use of convolution kernels, use of sums of specified dissimilar functions (e.g., a gaussian plus exponentials) and function fitting by a non-linear least-squares process. It has been found that the curve of the ratio of successive even moments, plotted against the order of the moments, is very helpful in giving a qualitative picture of how the flux curve behaves. On that basis, it is possible to predict which fitting techniques should be suitable. Conventional function-fitting procedures have been elaborated in various ways (e.g., fitting to every other moment, or starting with the  $n=2$  moment instead of  $n=0$ , etc.). The combination of these old and new techniques provides an armory of weapons adequate to deal with all types of moment behavior so far encountered. Particularly, it has been found possible to fit all situations in which the classical fitting techniques failed to give any physically realistic spatial dependence for the flux.



D. A Discrete-Energy Discrete-Ordinate Transport Computational Technique - J. Ching and H. Goldstein

The available discrete-ordinate anisotropic codes suitable for deep penetration calculations, such as ANISN, are based on a multigroup formalism. While the multigroup approach is probably the most efficient way of including in some measure the effect of rapid cross section variations on transport phenomena, it is a cumbersome technique when frequent changes in the input microscopic data are to be made. However, it has been possible to demonstrate that the multigroup  $S_N$  codes can also be looked upon as discrete-energy solutions of the transport equation. What are labelled as "group transfer coefficients" can be replaced in a one-to-one correspondence by certain "scattering constants" which appear, e.g. in the discrete energy moments method solution. It therefore seems possible to perform a marriage between the moments method code of Weisbin and ANISN to bring forth a discrete-energy discrete-ordinates code. The practical feasibility of this approach, and whether it possesses advantages for cross section sensitivity calculations, is now being investigated.

E. Data Preparation and Analysis Computer - L. J. Lidofsky, E. Reich, and J. Hahn

Additional bits and pieces of the computer (SEL 810B) and associated auxiliaries have been trickling in during the year. By the end of the calendar year, there had arrived and been put into operation the following items:

Computer CPU, with paper tape input, and teletype I/O

Disc unit ( $3 \times 10^6$  characters) and controller

Tape unit (7 track) and controller

Card reader

Line Printer

Extra 8K words of fast memory (total core now 16K)

No display is yet available, although an alpha numeric display has been ordered, and a rudimentary point-plotting CRT display is being built. Shakedown tests have revealed various hardware and software bugs. These have nearly all been eliminated, but final acceptance is not yet completed.

F. Effects of Perturbations on Particle Transport in Otherwise Homogeneous Media - H. Lichtenstein and L. J. Lidofsky

A method has been developed for the solution of the flux distribution for a certain class of particle transport problems. These problems are characterized by a known source in an extended medium. The homogeneity of the medium is perturbed by a localized inclusion of material having properties differing from those of its surroundings. As a specific example of interest, the localized inclusion may be a void.

The method of solution envisions a decomposition of the original problem into two related problems, such that certain characteristics of the original problem are isolated. This isolation of the characteristics reduces the complexity of the solution.

The two related problems may be described in the following manner: (1) the case of the original homogeneous medium and source prior to the inclusion of the perturbation; (2) the case of the homogeneous medium, source-free outside the region of the inclusion, but

having an effective source distribution inside the inclusion. The effective source of the latter problem can be shown to be a function of the solution to the first related problem and the properties of the homogeneous and perturbing media, only.

Since the first related problem is geometrically homogeneous, it may be solved by a variety of established techniques. The possible geometric complexity and the existence of an isolated effective source in the region of primary interest, however, suggests a Monte Carlo approach for the second problem, and a Monte Carlo code has been written. It is designed to solve for the scalar flux in two dimensional, multigroup problems, with the following restrictions: (1) the extended homogeneous medium is in slab geometry, (2) the perturbing region is cylindrically symmetric about an axis perpendicular to the surface of the slab; (3) the scattering is assumed to be independent of angle; (4) only down-scattering is assumed. The last restriction allows for a sequential solution, one group at a time, starting from the highest energy group. This Monte Carlo code is being tested at the present time.

G. High Energy Gamma Ray Production by 14 MeV Neutrons - M. Stamatelatos, B. Lawergren, L. J. Lidofsky

The object of the research has been to measure spectra of gamma radiation from 14 MeV neutron interactions, in particular, neutron capture in medium to heavy elements (copper, antimony, Zirconium).

The source of neutrons was a Texas Nuclear Corporation Cockcroft-Walton-type neutron generator, and the detector a specially built coincidence-anticoincidence telescope pair spectrometer composed of three thin and one thick NE-102 plastic scintillators.



The spectrometer was calibrated against gamma radiation in the range of 12-21 MeV from proton and deuteron reactions  $H^3(p,\gamma)He^4$ ,  $B^{11}(p,\gamma)C^{12}$ ,  $B^{11}(d,n\gamma)C^{12}$ . The protons and the deuterons were accelerated with the Pegram Van de Graaff. A spectrometer response function has been generated using these calibration spectra and a specially written non-linear least squares program. The function will be used in the final unfolding of the data obtained from the neutron capture reactions. Since the  $(n,\gamma)$  spectra are continuous rather than strongly peaked, an iterating unfolding technique, based on that of N. Scofield, has been adopted. It is currently being used for unfolding the data from copper, antimony and zirconium. The spectra and cross sections will be compared with various predictions of theoretical calculations including "semi-direct" capture.

ABACUS II, a nuclear optical model code written by Auerbach for the CDC 660 computer has been modified to run on the IBM 360/91 Columbia computer and will be used in the comparisons.

H. Response of Ge Li Detectors to Gamma Radiations - A. Tavitian and L. J. Lidofsky

A Monte Carlo code has been completed and is applicable to the energy range 0.1 MeV to 10.00 MeV, for the geometrical configurations listed below. The processes taken into account are: Compton effect, photo-electric effect, and pair production.

The output for each case consists of the generated gamma-ray spectrum and the peak-to-total ratio. Calculation of the single or double escape peak-to-total ratio, and the intrinsic efficiency can be inserted with a minimal amount of work.



The following source-crystal geometrical configurations are considered in the code:

A. Regular

1. Point isotropic source on the axis of a solid cylindrical crystal.
2. Point isotropic source on the axis (perpendicular to the plane of the front face) of a solid rectangular crystal.
3. Point isotropic source on the axis of a cylindrical shell crystal with a vacuum core.
4. Point isotropic source on the axis of a cylindrical shell crystal with an absorbing core.
5. Point isotropic source on the axis of a solid cylindrical crystal attached to a cylindrical shell (of the same radius) with an absorbing core.

B. Special

1. Point isotropic source on the axis of a solid cylindrical crystal; the total energy deposited in the detector as a function of the energy deposited in the front portion of the crystal. The front portion considered can be varied. The aim is to test means of reducing non-full energy events.
2. Point isotropic source on the axis (perpendicular to the plane of the front face) of a solid rectangular crystal; narrow in one direction, the azimuthal angle

of the scattered photon in a Compton interaction is picked by considering polarization. The aim is to calculate the polarization sensitivity of the detector.

Machine Time: 14 sec for 1000 histories.

## VII. ELECTRONIC INSTRUMENT DEVELOPMENT

### A. Time Analyzer - J. Hahn, C. Gillman, V. Guiragossian, A. Zidon, R. Mayer

As described in Progress Report NYO-72-227, the time-of-flight analyzer in use at the Nevis Laboratory is being replaced. The replacement was divided into two phases. Phase one has been completed and is described in the above report. Step one of phase two has been completed and will be used in the next experiment.

The major elements of the phase two system have been discussed previously and will not be discussed here. The previous discussion did not describe the manner in which data is emptied from the 16 word buffers, or the EMR 6130 interface. We will discuss these briefly, as well as the overall timing sequence of the complete system. We will also describe in some detail the Expansion of the I/O Bus System, the Display Controller, and the I/O Test Unit.

#### Buffer Output Logic

The buffer output data arrives as a 16 bit word at the output of each of the two buffers (described in report NYO-72-227 and a recent paper, "A 16,000 Channel, 50 MHz Time-of-Flight Analyzer for High Data Rates," presented at the 1969 IEEE Nuclear Science Symposium). With each word of data a flag bit is also sent and recognized by the output logic. Upon arrival of the flag bit, the output logic generates a parity bit for the data word and sends the data plus parity and a "DATA AVAILABLE" signal to the input gates of the interface. When the interface has transferred the data to the computer, it returns a

"DATA ACCEPTED" signal to the output logic, which then resets the flag bit of the appropriate buffer. When this has been completed, the output logic will service data in the second buffer, providing data is available at its output. If new data is not available, the output logic will await the arrival of new data.

### The Interface

The interface is the input/output link between the EMR 6130 computer and the time-of-flight system. It communicates with the central processor and controls communication between the time-of-flight and the word/byte channel. Communication is initiated between the central processor and the time-of-flight by the computer program sending an XIO START to the interface. The XIO START directs the time-of-flight analyzer to begin channel communication and to inform the channel of the desired mode of operation.

The two modes of operation possible between the channel and the time-of-flight are internal or external addressing. In the internal addressing mode, data sent to the channel from the time-of-flight will be stored sequentially in a pre-assigned memory area and used at a later time to build a histogram. In the external addressing mode, data sent to the channel from the time-of-flight will be put directly into the histogram by the channel. This is accomplished by the channel's taking the data as an absolute memory address and incrementing the contents of that location by one.

A simple timing diagram of the time-of-flight system is given in Fig. VII.A.1.



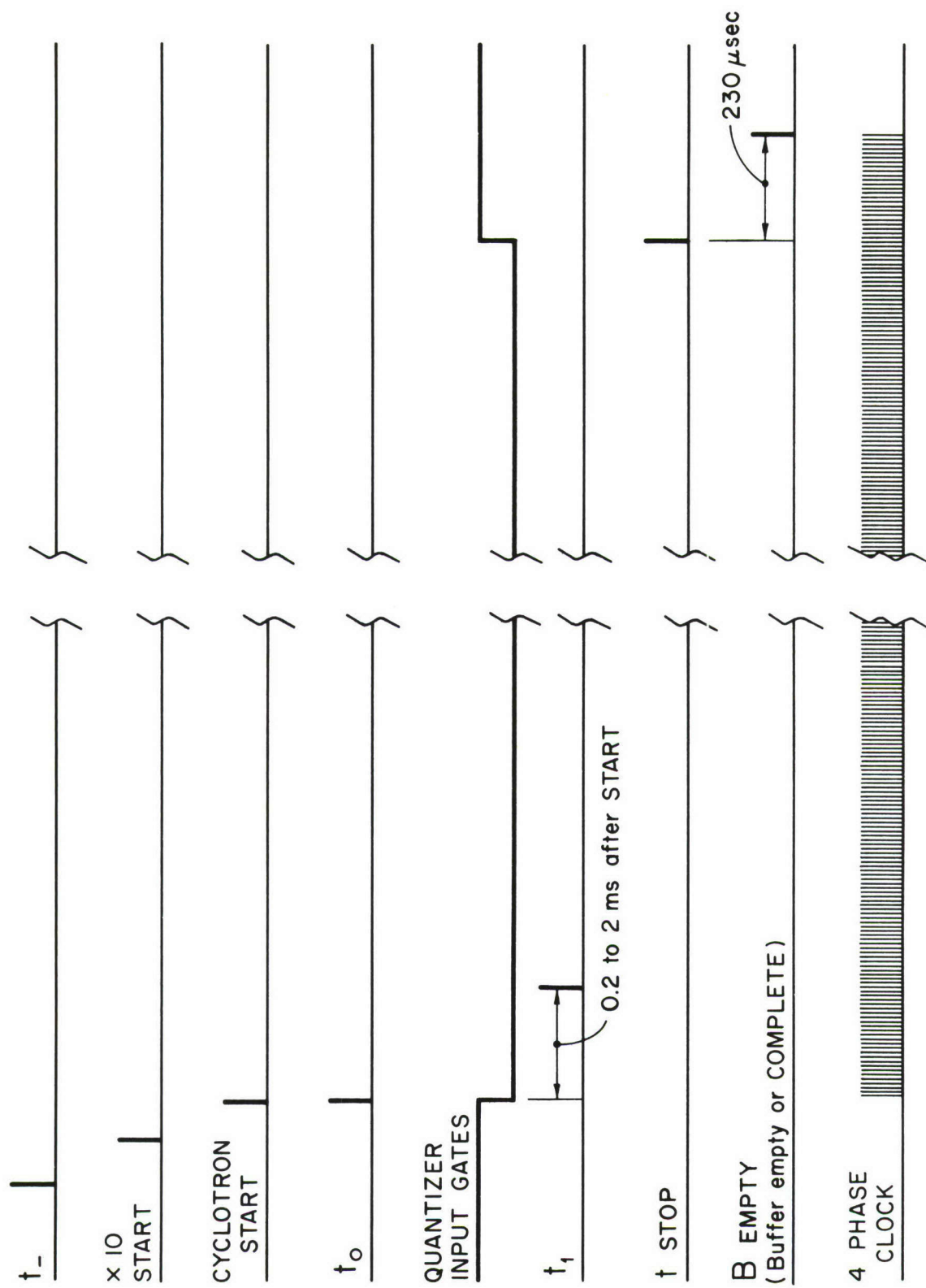


Figure VII.A.1.

## SIMPLE TIMING DIAGRAM — TOF SYSTEM

The cyclotron "START" signal indicates that the neutron pulse has occurred. A "t<sub>-</sub>" pulse is generated approximately 100  $\mu$ sec prior to the START pulse. It acts as a priority interrupt to the EMR 6130, which then communicates with the time-of-flight by sending an XIO START signal to it. When the time-of-flight receives an XIO START signal, it initiates communication with the channel and awaits the arrival of the cyclotron START.

The cyclotron START will start the 4-phase clock and the time-of-flight scaler. The scaler generates a "t<sub>0</sub>" signal, which opens the data gates of the quantizers and sends an interrupt to the computer, indicating the beginning of the data taking interval.

The scaler also provides a "t<sub>1</sub>" signal which can be manually set to come from 200 to 2000  $\mu$ sec after "t<sub>0</sub>". This signal can be used to delay the opening of one or more quantizers until the data arrival rate has fallen below some desired value, as well as to send an interrupt to the computer. The "t<sub>stop</sub>" pulse is generated by the scaler at the end of the last group of 512 channels. It is used to close the input gates of the quantizers and, after a 230  $\mu$ sec delay, to generate a "B<sub>empty</sub>" signal. The delay is generated in order to insure the emptying of any data remaining in the buffers. "B<sub>empty</sub>" stops the 4-phase clock and terminates communication with the channel.

#### Expansion of EMR 6130 I/O Bus System

Circuits were designed to expand the input/output bus system of the EMR 6130 computer used with the Nevis Neutron Velocity Spectrometer.

Two general types of I/O control are provided with the 6130 computer: direct programmed I/O (XIO) and compatible I/O operation. In addition, the computer is also equipped with two buffered Word/Byte channels, which utilize the compatible channel I/O lines. In the following paragraphs we shall describe 3 general interfaces: one for direct XIO and one each for the two Word/Byte channels (designated CCHIO-1 and CCHIO-2 hereafter).

#### XIO Interface:

The direct programmed I/O channel as obtained from the manufacturer is equipped with the Short Lines Transmission System. This transmission system imposes severe limitations on the number of devices which may be connected to the XIO channel through the XIO line, which cannot exceed 30 feet. Only eight devices are permitted, and the distance between a station and the I/O lines must be kept under four inches. Various portions of the processor itself make use of seven devices, and all of the 30 feet allowed are used up in the main frame.

In order to overcome these limitations, an XIO Bus Expander was designed and built which connects to the Short Line System as the 8th device allowed. This unit provides a link for data flow between the computer and the various peripheral devices through the expanded bus system.

Besides allowing additional external devices to be connected to the processor, the Expander unit also transforms all bi-directional lines into uni-directional ones. The 16 data lines from the Bus Adapter to the peripheral devices are uni-directional. The direction of data transfer is program controlled and will be explained later.

The expanded I/O bus contains 16 output data lines, 16 input data lines and numerous control lines. Three cables connect all peripheral devices to the Expander unit in a daisy chained manner so that all devices appear identical from the mainframe.

Typical connections used to perform input and output data word transfers are illustrated in Fig. VII.A.2. which shows the basic system organization for the transfer of one bit of data to or from the processor. Fig. VII.A.3. shows the schematic diagram of an XIO data transmission card which can handle four bits.

The circuit cards used to transmit the various control signals are identical to the data cards except that only the input or output sections are utilized, since all control signals are uni-directional.

As shown in Fig. VII.A.2. the basic XIO System includes two shielded twisted-pair transmission lines, one for data into the computer and one for data out of the computer. The data out line is balanced and is terminated with its characteristic impedance at the far end of the line, since data is always fed at the computer end only. External devices distributed along this line must use a Motorola differential line receiver, type MC1020, to receive the signal at the intended point of use.

The Data In line is unbalanced since the MC1026 MECL drivers used in the external devices are not gated. This line is terminated at both ends, since signals are fed into it anywhere along the line. Termination at both ends is an absolute necessity in order to avoid



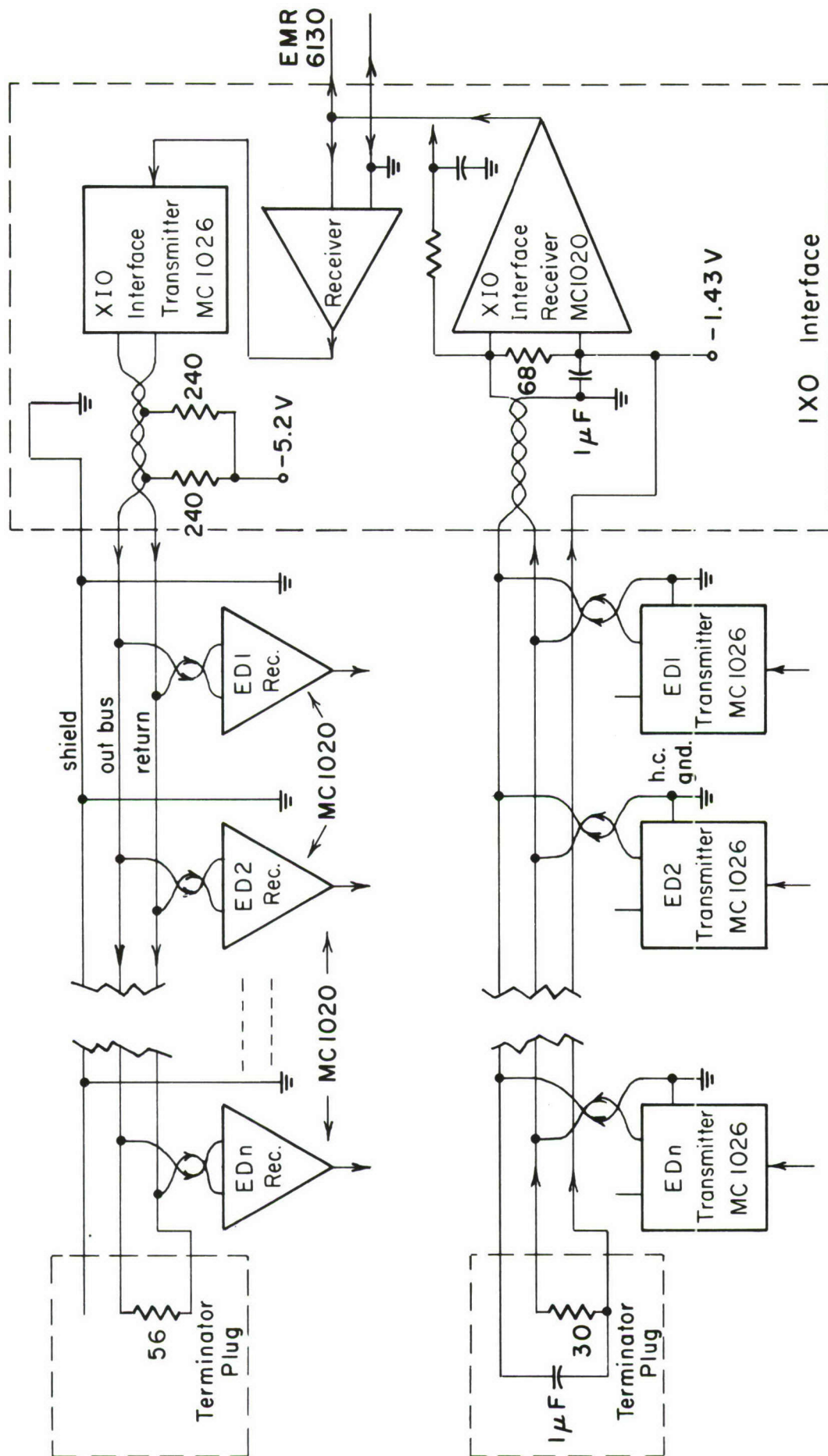


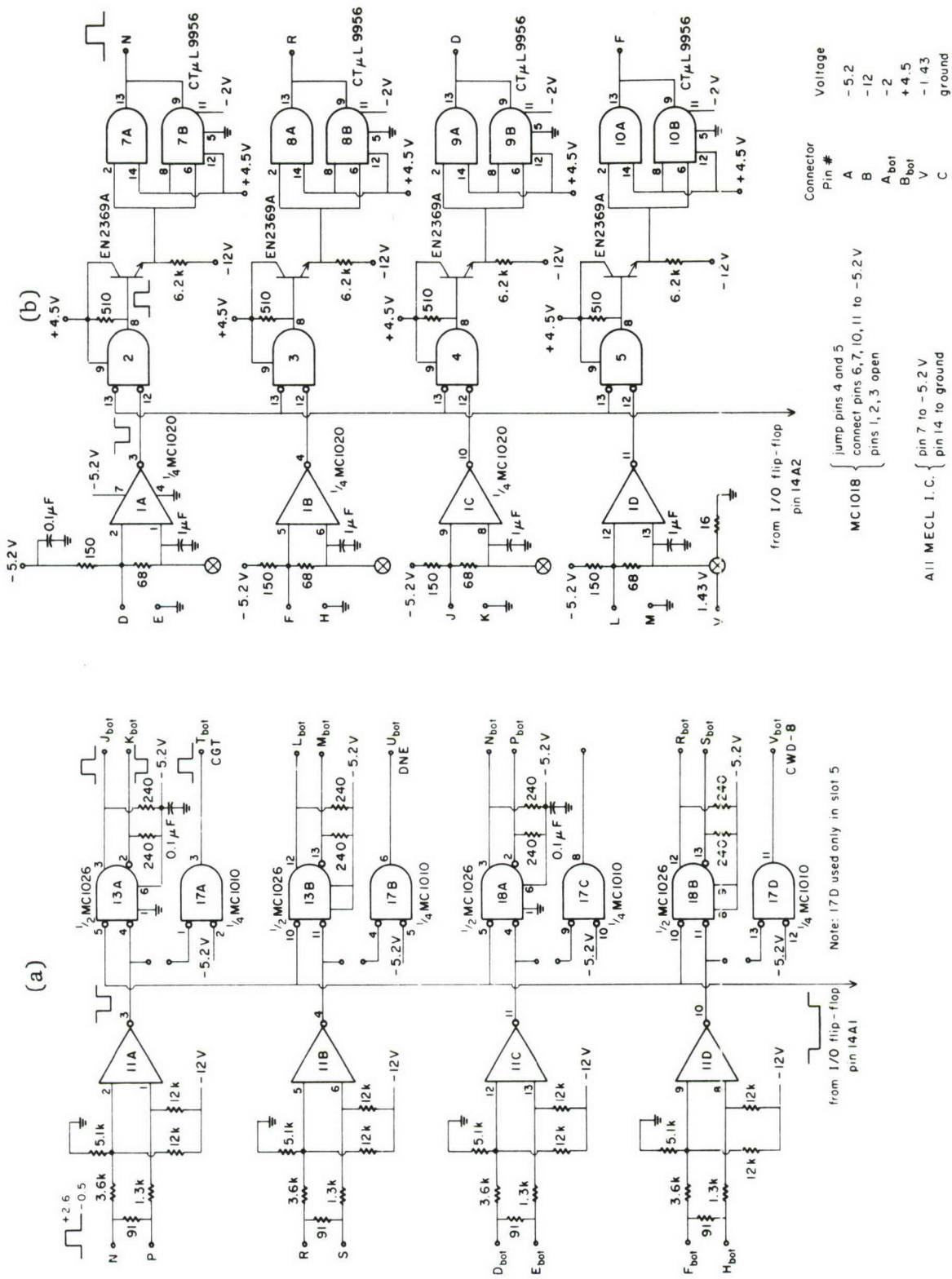
Figure VII.A.2.

troublesome reflections. At the far end of the line the terminating resistor is  $30\Omega$ , while at the sending end the input impedance of the line receiver in parallel with the parallel combination of the  $68\Omega$  and  $150\Omega$  resistors effectively terminates the pair. This value was chosen experimentally to obtain the best waveform possible.

Figure VII.A.3. shows the circuit diagram of a typical data transmission card which handles four data bits. It consists of 2 sections: section (a) receives information from the processor and transmits it to the external devices, while section (b) transmits information in the reverse direction.

A Motorola type MC1020 differential line receiver is used to receive the signal in both sections (a) and (b). The line receiver is a special type of differential comparator and its functions are to restore the logic dc level, to reshape the incoming signal, to reject common-mode noise and to suppress the effects of differential noise. All signals are pulses of 100 nsec duration and are transmitted with twisted pairs of wires.

Referring to section (a), the CTL signal levels from the processor (logical one = 2.5 V, logical zero = -0.5 V) are changed to MECL levels (logical one = -0.8 V, logical zero = -1.6 V) by the resistive network at the input of the line receivers. The shaped signal from the output of the line receiver is fed to one of the inputs of a MC1026 gate, while the second input is connected to the Input/Output switching control circuit. The output from the MC1026 provides complementary outputs which drive a balanced shielded



All I.C. supply pins bypassed with 0.1  $\mu$ F capacitor

Figure VII.A.3.

twisted-pair line. A resistive terminator adjusted to match the surge impedance of the line is used at the far end of the line. The last unit in the daisy chain is equipped with a terminator plug. Any peripheral device connected to this line must receive the signal with a MC1020 line receiver.

In section (b) the shaped signal from the line receiver is fed to one of the inputs of a MC1039 circuit used as a level translator to change the MECL logic levels into saturated logic levels of 0 V and +5 V suitable to drive the output CTL drivers. The second input of MC1039 receives a gating signal from the input/output switching control circuit.

#### CCHIO-1 and CCHIO-2 Interface

CCHIO-1 and CCHIO-2 data cards are slightly different from the XIO data cards, although both function in the same manner and their input and output characteristics are identical.

The system organization for CCHIO-1 data lines is identical to the XIO lines system as illustrated in Fig. VII.A.2.

CCHIO-2 is used exclusively to connect the time-of-flight system (described elsewhere in this report) to the processor. Since there is only one user, both input and output signals are transmitted along balanced lines.

#### Input/Output Switching Control

Figs. VII.A.4 and VII.A.5. show the schematic diagrams of the Input/Output data switching control circuits associated with the XIO and CCHIO interfaces. The two circuits are quite different from one another, although they perform the same function, namely, to control



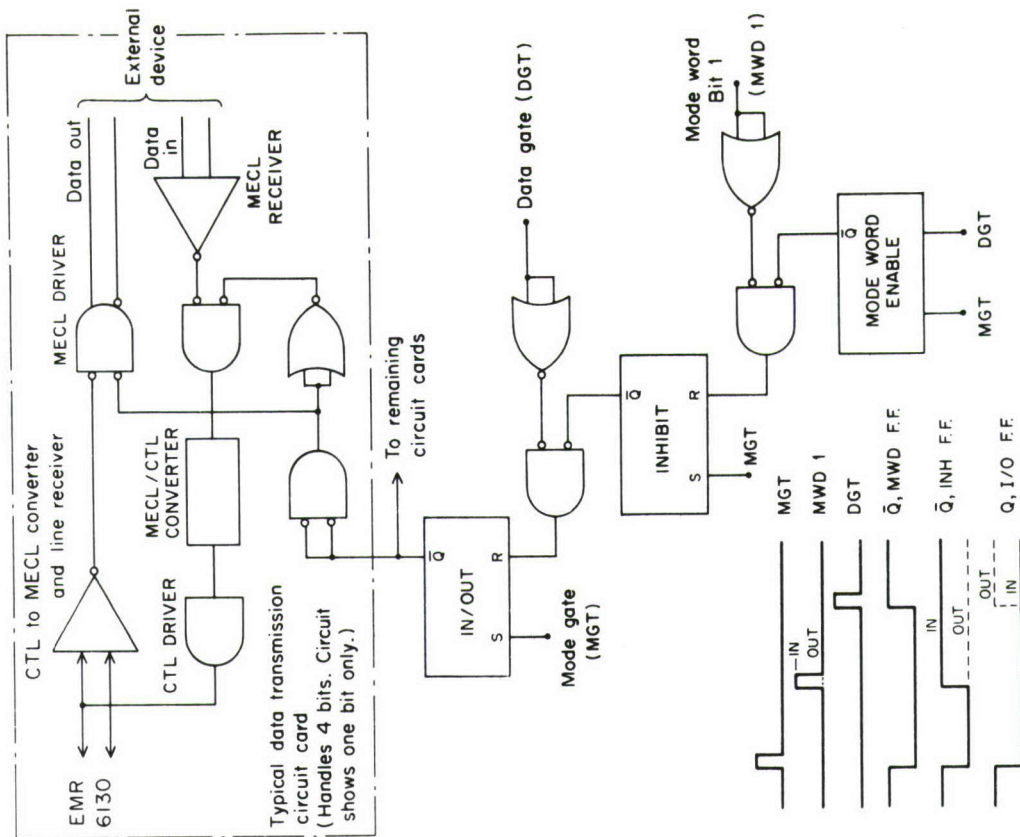


Figure VII.A.5.

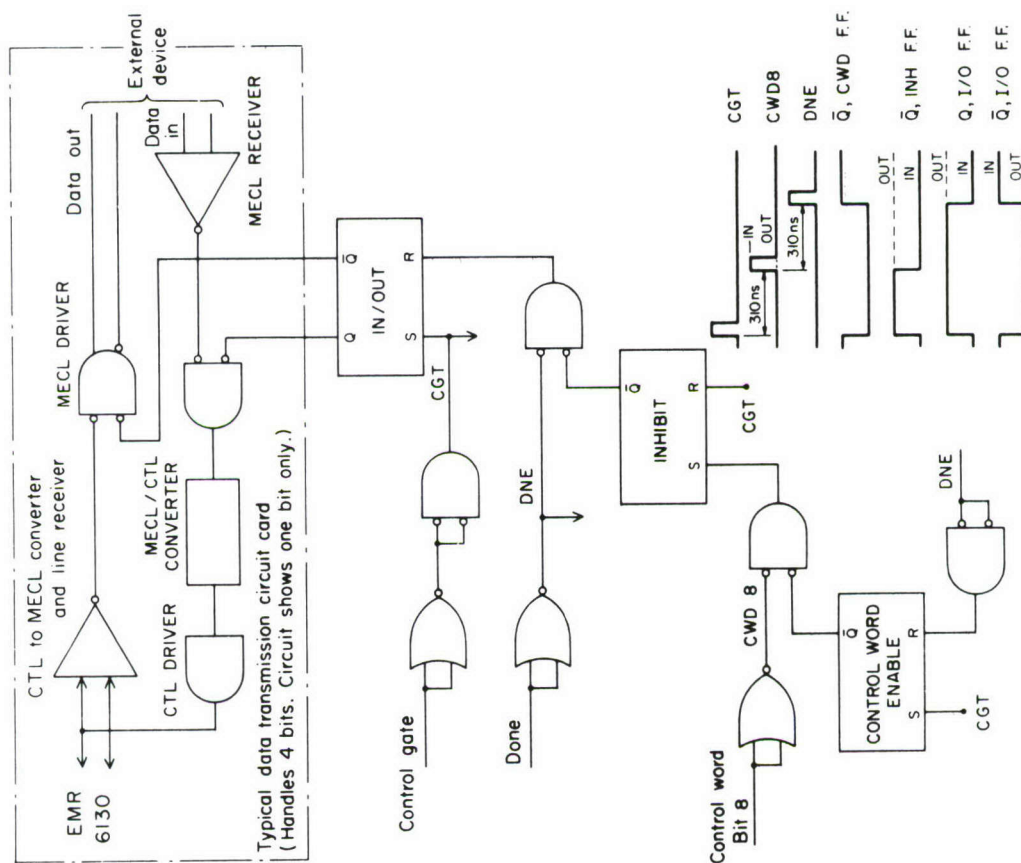


Figure VII.A.4.

the direction of data flow in or out of the computer, upon computer command.

(a) XIO control

The circuit and timing diagrams in Fig. VII.A.4. show how the input/output data switching is performed. A typical data transmission card is also shown on the figure in block diagram form. Each data transmission card can handle 4 data bits, but the diagram shows the circuits for one bit only. The remaining three circuits are identical to the one shown. Every data card is equipped with its own I/O switching control circuit, which consists of three flip flops and two input logical AND gates.

An XIO communication uses two transfers on the data lines. The first data transfer is always a control word (CWD) which originates in the processor and specifies what the second data transfer will be. The second data transfer may be an instruction to an external device, a data input, or data output transfer.

The direction of data flow is determined by bit 8 of the Control Word. Bit 8 = "1" means data input operation and bit 8 = "0" data output operation. As a result of the program execution of an XIO instruction, the processor sends a series of control pulses on the XIO control lines. The first pulse, Control Gate (CGT) is used to reset the Inhibit (INH) flip flop and set the Control Word (CWD) and Input/Output (I/O) flip flops. An XIO communication always starts with the I/O flip flop set in order to allow the transmission of the Control Word to all external devices.

After a 320 nsec delay following Control Gate, the processor sends the Control Word. If bit 8 of the Control Word is "0", meaning the second word will be an output data transfer, no change occurs, since the output data lines are already open. If CWD8 = "1", the INH flip flop is set, and the Done (DNE) pulse, which is sent from the processor 320 nsec after the Control Word, resets the I/O flip flop. The resetting of the I/O flip flop closes the data out lines and opens the data input lines.

Bit 8 of the Control Word should be properly isolated so as not to confuse it with bit 8 of a data word. This is accomplished by setting the XIO flip flop with CGT and immediately resetting it with DNE after bit 8 is examined.

(b) CCHIO control

Unlike the XIO data transmission cards, the CCHIO cards are not equipped with individual I/O switching control circuits. There is only one circuit and it controls all 16 data lines through a set of inverters located on each transmission card as shown in Fig. VII.A.5.

The external device is first commanded from the processor through the XIO. The external device then initializes the channel to which it is connected by sending certain control signals on the compatible channel control lines. The first signal sent is the Mode Gate (MGT), which is followed by the Mode Word (MWD) if there is to be any communication between the external device and the channel. Bit 1 of the Mode Word determines the direction of data transfers. If bit 1 is a logical "1", the communication is to be input of data from the external device. The third signal of interest in our case is the Data



Gate (DGT) issued from the external device, which means that the external device is going to send a data word to the channel or it is ready to accept a data word from the channel.

Fig. VII.A.5. and the accompanying timing diagram show how the circuit works. The control circuit starts with the input sequence, since the first communication on the CCHIO data lines is the transmission of the Mode Word from an external device.

The Mode Gate Signal is used to set all 3 flip flops.  $\bar{Q}$  terminal of I/O flip flop is low and therefore the input data lines are open for the Mode Word to go through. If bit 1 of the Mode Word is "1", the Inhibit (INH) flip flop is reset and inhibits the resetting of the Input/Output flip flop when the external device sends the Data Gate pulse. The input data lines thus remain open. If  $MWD1 = "0"$ , meaning output data transfers, the INH flip flop remains set and the DGT pulse resets the I/O flip flop which closes the input data lines and opens the data out lines.

Bit 1 of the Mode Word should be properly isolated so as not to confuse it with bit 1 of a data word. This is accomplished by setting the Mode Word flip flop with MGT and immediately resetting it with DGT after bit 1 has been examined.

#### Construction

The logic circuitry for the three systems described in the bus expansion is comprised of Motorola MECL II and Fairchild CT $\mu$ L integrated circuit elements, as well as discrete component circuits. In all, 357 integrated circuit packages are used, with sockets for ease of replacement. All circuits are wired on 5" x 5 1/4" copper



clad boards with card edge connectors. Fifteen such circuit cards, comprising the logic circuitry for CCHIO-1 and CCHIO-2 interfaces are mounted in a parallel row within a standard 19" module mounting frame. A second bin houses 7 circuit cards comprising the XIO interface logic. All interconnections between the circuit cards are made at the card mounting connectors. Both mounting frames are housed in the computer cabinet.

The equipment contained within the cabinet also includes power supplies and an I/O panel with three sets of connectors. Three I/O cables, one each for Data In, Data Out, and Control signals, extend the input/output bus to the first peripheral unit in the daisy chain.

All equipment is located in the rear of the third bay and is accessible by removing the rear panel.

The three interfaces were installed in July and have been performing satisfactorily.

#### Display Controller

A Display Controller was designed and interfaced to the DMR 6130 computer used with the synchrocyclotron time-of-flight system at the Nevis Laboratory. The present digital display system connected to the EMR 6130 is manufactured by Information Displays Incorporated and the displays generated are entirely under program control. The purpose of the unit described here is to enable the experimenter to control or modify the display programs manually from a switch controlled external device.

The Display Controller is made up of two separate units: an operator input consisting of various types of data-entry switches and a control logic unit for transferring into the computer the information contained in the switch registers.

The switches are mounted on the control panel of a small desk-top type cabinet, which is conveniently located on the display operator's desk, and connects to the control unit with two 15 foot cables, each with 50 conductors. The outputs from the switches are collected into six 16 bit registers and each register is assigned a unique device number. In this way information from the switches can be transferred into the processor upon computer command addressed to a particular set of switches.

Octal code numbers 12 through 17 are assigned to the six switch devices listed below together with their respective functions.

Device # 16: This register has its 16 inputs connected to the X<sub>0</sub> switch used to set the initial channel X<sub>0</sub> at which it is desired to start the display. X<sub>0</sub> can be set to any decimal number from 0 to 19999 with a 5 decode BCD coded thumbwheel type switch. The high order bit from the fifth decode is collected into bit 16 of device #17.

Device #15 and device #14 are used to provide fiducial markers for determining the X and Y coordinates of any point in the display. The X position of the fiducial marker can be set from 0 to 19999 while the Y fiducial marker can be set anywhere in the range from 0 to 29999. As with the X<sub>0</sub> switch, both X and Y fiducial marker

controls consist of 5 decode BCD coded thumbwheel switches each, and as with the previous device, the 17th bit of  $X_f$  is collected into bit 15 while the two high order bits from  $Y_f$  are collected in bits 14 and 13 of device #17.

Device #17: Besides collecting the leftover bits from  $X_o$ ,  $X_f$  and  $Y_f$  switches, device #17 controls the operation of the X and Y scale thumbwheel switches. The outputs from one octal BCD coded Y scale switch are connected to bits 1 through 3 while the five output lines from the And/Nor type X scale switch are tied to bits 4 through 8. Bits 9 through 12 are unused and are permanently wired to the logical zero level.

Devices #13 and 12 consist of a row of 16 toggle and 16 push button switches for stationary options such as adjusting the intensity of the beam on the display scope, shifting marker positions, or removing the grid etc. . . . The signals from these switches become flags to the program for starting a new routine or for branching the program to another point. The push buttons are used for momentary commands such as typing out some counts on the teletypewriter, starting the line printer program or the plotter program, etc. . . .

The control unit consists of logic which receives the information from the switch assembly and communicates with the computer via the Direct Programmed I/O channel.

Direct XIO is a two word communication. As a result of the program execution of an XIO instruction, a Control Word is first transferred on the output data lines to all external devices. This Control Word is addressed to a particular device and specifies the



nature of the second word. In the present application the second word is always an Input Data Word from one of the switch registers. These data words are then transferred on the input data lines with strobe pulses which are gated against their respective unit decode logic in order to ensure that only the addressed unit is commanded. All signals are pulses of 50 to 100 nanoseconds duration and are transmitted with twisted pairs of wires.

A block diagram of the control-interface is shown in Fig.

VII.A.6. Reading of the information contained in the switch registers starts when the processor sends a series of pulses on control wire for each XIO instruction to be executed.

The processor first sends a Control Gate (CGT) signal on the XIO control lines. Upon receipt, this signal is used to clear the Input Data Register, the Device Sample circuit and the six Device Select flip-flops. The Control Gate signal also sets the Receive flip-flop (RCV) thereby opening the gates to the data receiving register.

After a 320 nanosecond delay following Control Gate, the processor sends the Control Word on the output XIO data lines. The 7 least significant bits of this word are received into the Data Register. Bits 1 through 6 specify the address of the switch register to which this communication is directed, while bit 7 specifies whether the communication is a Scanned Interrupt communication (Bit 7 = 1) or a Direct XIO instruction (Bit 7 = 0).

Three hundred twenty nanoseconds after sending the Control Word the processor sends a Done (DNE) signal, which by resetting the Receive



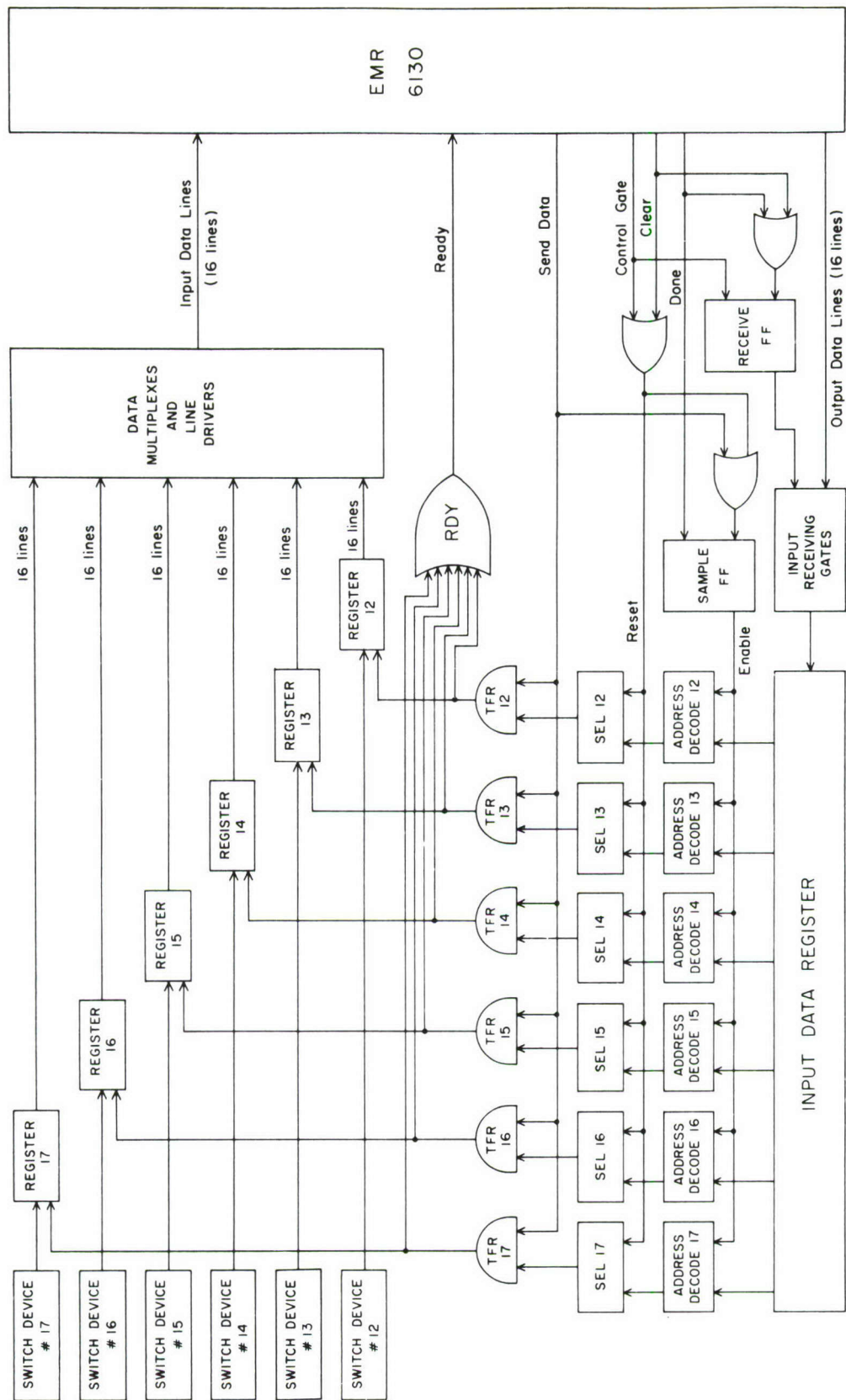


Figure VII.A.6.

(RCV) flip-flop closes the data input gates. The Done signal is also used for sampling the Address Decode circuits.

Each Address Decode circuit, upon recognizing its address, sets its Device Select flip-flop to the "one" state. The "one" output from each Device Select flip-flop is connected to the enable input of a two input AND gate labeled Transfer Gate, while the second inputs of all gates are tied to the Send Data line.

The computer sends the Send Data (SDA) signal 320 nanoseconds after the Done signal. Upon receipt of this signal the output from the enabled Transfer Gate strobes the contents of the specified switch register on the XIO input data lines.

At the same time as data is being supplied to the data lines, a Ready signal (RDY) is transmitted to the processor. This Ready signal, produced by ORing the six Transfer Pulses, indicates to the computer that the control unit is able to respond to another XIO communication.

The system described was constructed exclusively with Motorola MECL II dual in line integrated circuits in order to make all input, output and control signals compatible with the logic levels provided by the XIO Bus Expander described elsewhere in this report.

In all 118 integrated circuit packages are used with sockets for ease of replacement. All circuits are wired on 4 1/2" x 5 1/4" copper clad boards with card mounting connectors. Twelve such circuit cards are mounted in a parallel row within a standard 19" rack mounting NIM bin which also contains the units power supply. All intercommunications between the circuit cards are made at the card mounting connectors.

An I/O panel located at the rear of the NIM bin contains three sets of connectors designated P1, P2, P3. Each set consists of a pair of 50 pin Amp connectors with all their corresponding pins tied together. Three I/O cables, one each for Data In, Data Out, and Control Signals plug into one of the P1, P2, P3 connectors to connect the Display Controller to the XIO Bus Expander. The second P1, P2, P3 connectors from each pair provide for connecting the cables which extend the input/output bus to the next peripheral unit in a daisy-chained manner.

#### EMR 6130 I/O Test Unit

A Test Unit was designed and built for checking and debugging the Display Controller connected to the EMR 6130 computer (the Display Controller is described in detail elsewhere in this report).

The Test Unit simulates the EMR 6130 for this particular application by generating timing and control signals normally supplied by the processor when it is executing a programmed I/O instruction. Direct XIO is a two word communication. A Control Word is first transferred on the output data lines to all external devices, followed by a Data Word.

A block diagram of the Test Unit is shown in Fig. VII.A.7. It consists of the following major elements:

Control Word Generator: This circuit generates the seven least significant bits of the Control Word required to command the Display Controller. Bits 1 through 6 specify the address of one of the six display switch assemblies from which a data word will be read into a digital indicator circuit. Bit 7 specifies whether the communication is a scanned interrupt interrogation (Bit 7 = 1) or a direct XIO instruction (Bit 7 = 0).

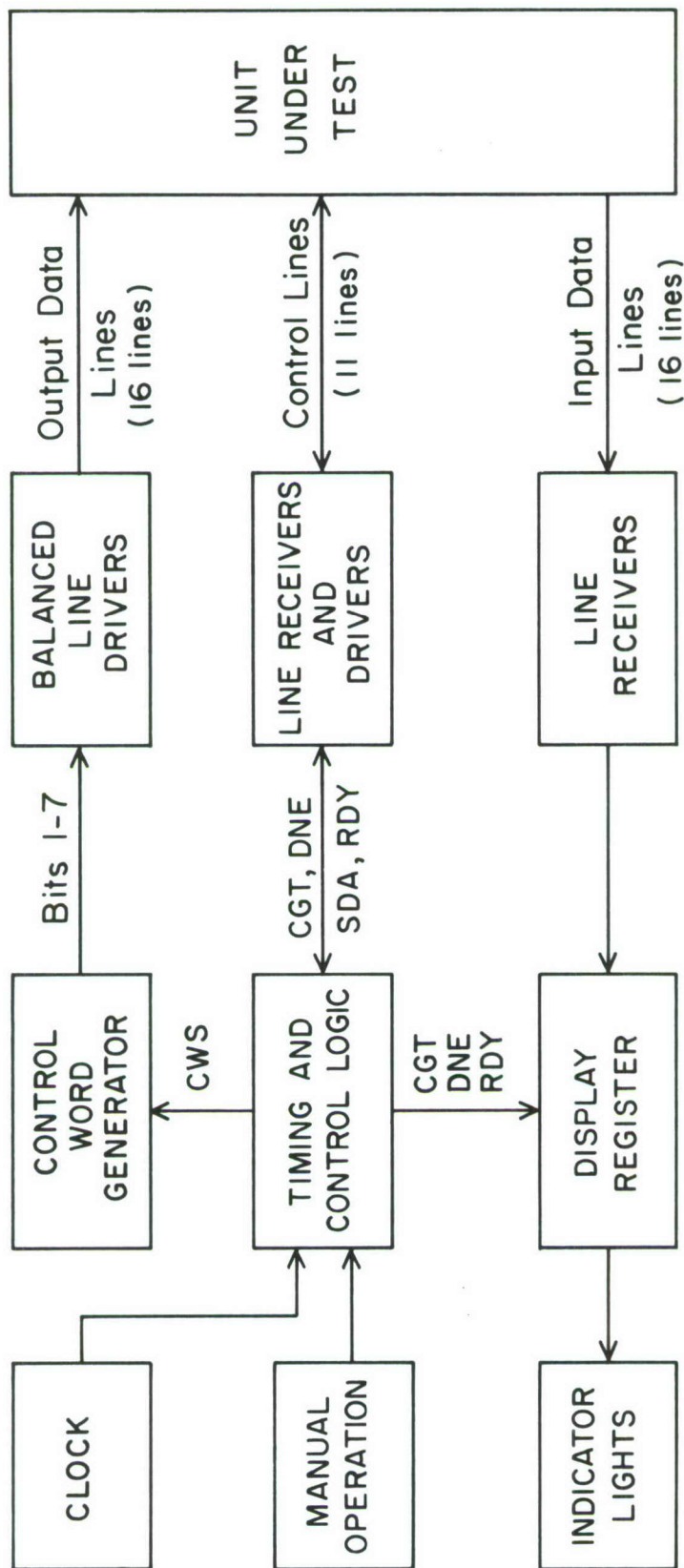


Figure VII.A.7.



Individual bits of the Control Word Register are set manually with toggle switches mounted on the front panel of the unit. The contents of this register is then gated on the output data lines with the Control Word strobe signal.

Digital Indicator Lights: The Control Word is received by the Display Controller where it is decoded. A signal from the address device decode circuit is then used to enable the particular switch device addressed. Upon receipt of the Send Data signal the contents of the enabled switch register is immediately transferred to the Test Unit where it is visually displayed.

Sixteen indicator lights are mounted on the front panel of the Test Unit, one for each bit of the data word transferred. Buffer flip-flops are added to each bit so that the lights continuously display the information from the switch device last addressed. The flip-flops are cleared only with the Control Gate signal at the start of another read sequence.

Line Receivers and Drivers: Three I/O cables connect the Test Unit to the Display Controller. A set of balanced cable drivers and differential line receivers are used for both the data lines as well as for the control lines. All signals are pulses of 100 nanoseconds duration and are transmitted with twisted pair wire.

Construction: The Test Unit was constructed with integrated TTL and MECL modules on a 7" x 8 1/2" copper clad board and is housed in a triple width AEC Nuclear Instrument Module.

The Unit was originally designed for testing the Display Controller, but it could easily be adapted to check any external device which inputs data into the computer via the Direct Programmed I/O channel.

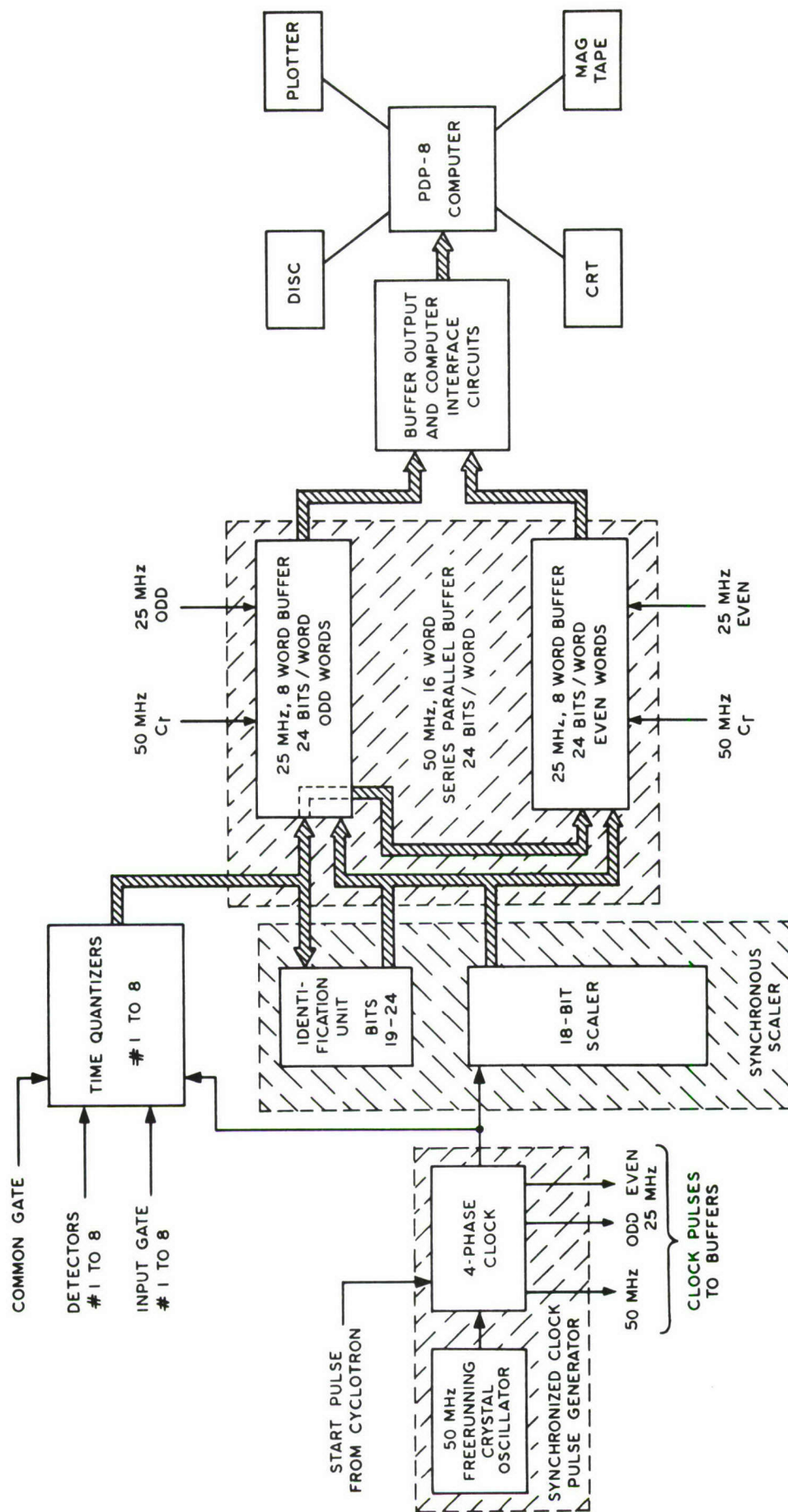
B. 262,000 Channel Time-of-Flight Analyzer - J. Hahn, T. Becker, S. Cucancic, A. Zidon

A 262,000 channel time-of-flight analyzer has been designed and constructed for use with a PDP-8 computer by the Fission Experiment Group.

This time-of-flight analyzer is fundamentally similar to the 16,000 channel time-of-flight analyzer described in Section VII.A. of this report and in previous reports. A simplified block diagram of the system is given in Fig. VII.B.1.

The major differences between the two analyzers are:

- 1) The 262,000 channel analyzer uses an 18 bit synchronous scaler. The scaler always works at a 50 mHz rate; that is, channel widths are always 20 nsec and do not have variable width, as in the 16,000 channel system.
- 2) A 24 bit, 16 word buffer is used. This buffer uses 6 of the 18 bit, 8 word buffers described in detail in connection with the 16,000 channel analyzer.
- 3) Six bits of the detector coding information are merged with the 18 bits of timing information to form the 24 bit event word. (The details of the coding information are described below.)
- 4) The 24 bit event word is transferred to the PDP-8 as two 12 bit data transfers. (The details of the output logic and interface are described below.)



SIMPLIFIED BLOCK DIAGRAM OF NEUTRON TIME-OF-FLIGHT SYSTEM

Figure VII.B.1.



All input and output levels are MECL levels, i.e. -0.8V is a high level and -1.6V is a low level, both measured relative to the ground. The only exceptions to this are the oscilloscope trigger output and the 60 Hz output.

Data Inputs: There are 8 independent data inputs. The input signals are negative pulses, i.e. high level measuring 0, low level measuring 1. The length of the pulses is arbitrary.

The data inputs are automatically gated internally. When the instrument is operating properly, any data acceptance is prevented between bursts. At the beginning of the burst, data inputs are automatically opened immediately after the arrival of the START pulse. The inputs are closed approximately 600  $\mu$ sec before the SCALER OVERFLOW pulse, which is used to generate the program interrupt of the computer.

Identification of data inputs: Bits 1 through 18 of each word sent to the computer are time-of-flight data bits, and bits 19 through 24 are used to identify the data input at which data occurs. The truth table is shown below. In cases where data appears simultaneously at more than one input, bit 24 is set to 1 and the state of bits 19 through 23 is the logical OR of the individual bits.



Input No.	Bit Number					
	19	20	21	22	23	24
1	1	0	0	0	0	0
2	0	1	0	0	0	0
3	1	1	0	0	0	0
4	0	0	1	0	0	0
5	1	0	1	0	0	0
6	0	1	1	0	0	0
7	1	1	1	0	0	0
8	0	0	0	1	0	0
9	0	0	0	0	1	0
more than one	0	0	0	0	0	1

Gate Inputs: Each data input can be individually gated with pulses (anticoincidence mode operation) or with levels. No modification of the instrument is necessary to switch from one mode to another.

For antineutrino mode operation, the gating pulses are positive and their timing corresponds to the input data pulses. The leading edges of both pulses are either coincident or the leading edge of the gate pulse arrives a few nanoseconds earlier. The duration of the gate pulses should be at least 40 nsec, for safe operation.

The gating width levels operate as follows:

high gating level → data inputs are gated

low gating level → data inputs are not gated.

The common gate input: All data inputs can be gated simultaneously by the COMMON GATE INPUT. This gating is usually done by levels, i.e.

high level → all data inputs are gated simultaneously

This gating does not effect the internal automatic gating. Only during the active period can an additional gating be obtained.

60 Hz output: In the absence of a cyclotron start pulse, this output can be used for testing purposes. The waveform is a limited and roughly squared sine wave obtained from the 120 VAC line.

Oscilloscope trigger output: This output pulse is synchronized with the occurrence of the first clock pulse. It is a positive pulse of approximately 3 V amplitude.

Data monitor output: All the input data pulses after reshaping and quantizing are logically OR-ed and fed as negative pulses to this output for monitoring purposes.

Output logic unit: The output logic unit is essentially a control unit. Its purpose is:

- 1) to detect if there is any data available from either of the buffer memories (or both)
- 2) to decide from which buffermemory data will be delivered to the computer and to control the format selection in order to assure that the 12 more significant bits (13-26) are delivered first and the 12 less significant bits (1-12) are delivered afterward.

3) to reset the last flag of the corresponding buffer memory after data has been accepted.

In relation to communication with the computer, its purpose is:

- 1) to send to the computer a BREAK REQUEST signal level whenever there is data available to be sent
- 2) to receive a DATA ACCEPTED signal from the computer and to switch the selection from the first to the second half of the word, or to switch to the other buffer if there is more data available
- 3) to receive an ADDRESS ACCEPTED signal from the computer and reset the BREAK REQUEST signal if there is no more data available.

TOF Buffer Interface: The TOF buffer supplies two 12 bit words for each detected event as explained above in the section on the output logic. These data words are transferred directly to the PDP-8 computer's core memory through the data break facility. A single-cycle data break is used so that each word transfer takes 1.5  $\mu$ sec of memory time or each event takes 3  $\mu$ sec for a double word.

For the single-cycle data break, a 12 bit Data Break Address Register is provided in this interface to specify the core address of each transfer. Memory locations 7200 to 7600 (oct) have been reserved as a buffer memory in the computer. The input to the Address Register is inhibited after 512 words to prevent writing over the program in memory locations past 7600 (oct). The number of accepted events per burst is expected to be much less than the 256 events allowed in this buffer.

Referring to Fig. VII.B.2., the circuit operates in the following manner:

When data is available in the TOF Buffer memory, a TOF BREAK REQUEST signal is sent to the interface. The TOF BREAK ANDed with the TOF ENABLE requests a Data Break, initiating the following sequence of events: the computer completes the current instruction, generates an ADDRESS ACCEPTED pulse, then enters the break state. The ADDRESS ACCEPTED pulse is sent to the TOF, increments by one the Data Break Address Register, and resets the BREAK REQUEST signal if there is no more data available. The BT1 computer timing pulse then reads the data into the memory and is ANDed with the computer B BREAK signal to provide the DATA ACCEPTED pulse to the TOF. If the BREAK REQUEST signal is removed before T1 time of the data break cycle, the computer performs the transfer in one 1.5  $\mu$ sec cycle and returns to the program. Since each event consists of a double word, a minimum data break is 3  $\mu$ sec.

The Break Request gate can be enabled or disabled by program instruction through the TOF ENABLE flip-flop. This is accomplished with pulse IOT 6174, which adjusts the state of the ENABLE flip-flop according to presence or absence of ones in the accumulator bits 2 and 3.

The TOF Scaler Overflow signal, which arrives 6 msec after a Start signal to the TOF, is used as a clock to provide a Program Interrupt to the PDP-8. After identifying the Clock as the source





of interruption, the computer program issues an IOT pulse to test the skip gate associated with the TOF Clock Interrupt Flag. If the Clock skip gate responds, the program enters the TOF servicing sub-routine to transfer and store the information present in computer buffer locations 7200 to 7600 (oct). The TEST CLOCK signal also resets the CLOCK FLAG flip-flop. Included in the TOF service sub-routine would be an instruction which would issue an IOT RESET REGISTER pulse to reset the Date Break Address Register to 7200 (oct).

The interface, except logic level converters and data line receivers, was built using Flip-Chip modules supplied by Digital Equipment Corporation. Data bits are fed to the computer by a twelve twisted pair line. Motorola MC 1020 line receivers are used at the computer interface followed by single transistor level converters to convert the MECL levels -0.8 and -1.6 volts to the Dec levels of -3 and 0 volts.

The following IOT commands have been assigned to the TOF Buffer System:

- 6151 Skip on Address Register Overflow (>7600 (oct)).
- 6152 Test Clock, resets Clock Flag.
- 6154 Reset Address Register to 7200 (oct).
- 6174 Operating mode determined by accumulator bits 2 and 3.

AC2	AC3	
0	0	No operation.
0	1	Set TOF ENABLE flip-flop.
1	0	Reset TOF ENABLE flip-flop.

A complete interconnection diagram of the system is given in Fig. VII.B.3.

### C. PHA Interface - T. Becker

A logic control system was designed and built to interface a 8196 channel Northern Scientific ADC (model NS-627) to the PDP-8 computer to be used by the Fission Experiments group for the study of gamma rays using a germanium detector.

The ADC supplies 13 data bits, while the PDP-8 is only a 12 bit machine. Therefore, a two word transfer is made with the extra bits being used as an identification code. The first word contains a five bit code and the seven most significant data bits. The second word also contains the 5 bit code and the six least significant bits.

Referring to Fig. VII.C.1., the circuit operates in the following manner:

When the ADC finishes digitizing an input event it sends a READY signal to the interface. The Ready level, ANDed with the Enable level, requests a Program Interrupt, initiating the following sequence of events: the computer upon receiving the Program Interrupt enters a special subroutine to identify the source of interruption through the Input/Output skip facility. The computer issues an IOT pulse to test the skip gate associated with the ADC Interrupt Flag. If the ADC skip gates respond, the program enters the ADC servicing subroutine to transfer and store the information present on the address register output lines of the converter. The READY signal also sets the WORD FLAG so that the first READ ADC followed by CLEAR

262,000-CHANNEL TIME OF FLIGHT ANALYZER  
BLOCK DIAGRAM

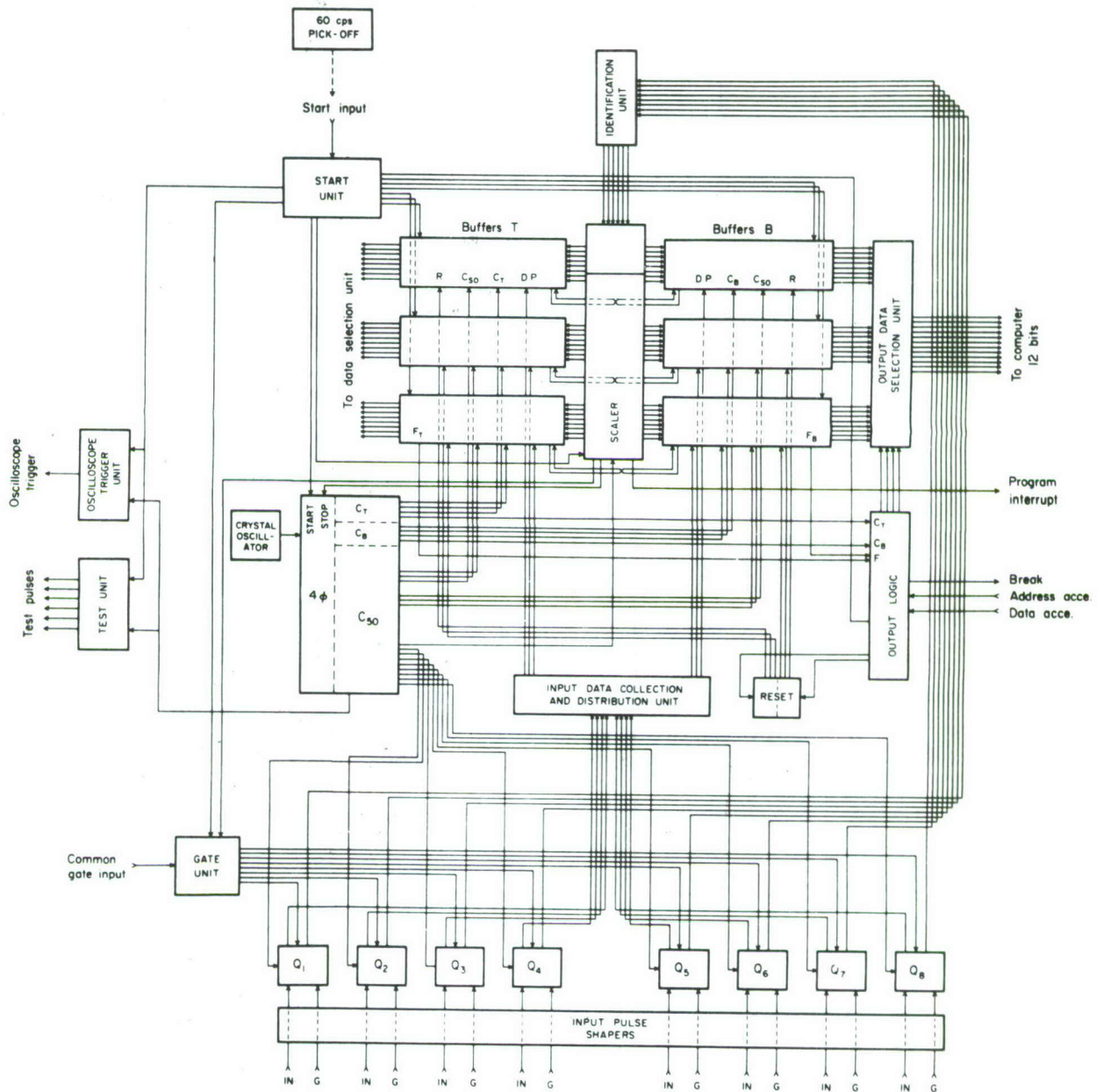


Figure VII.B.3.



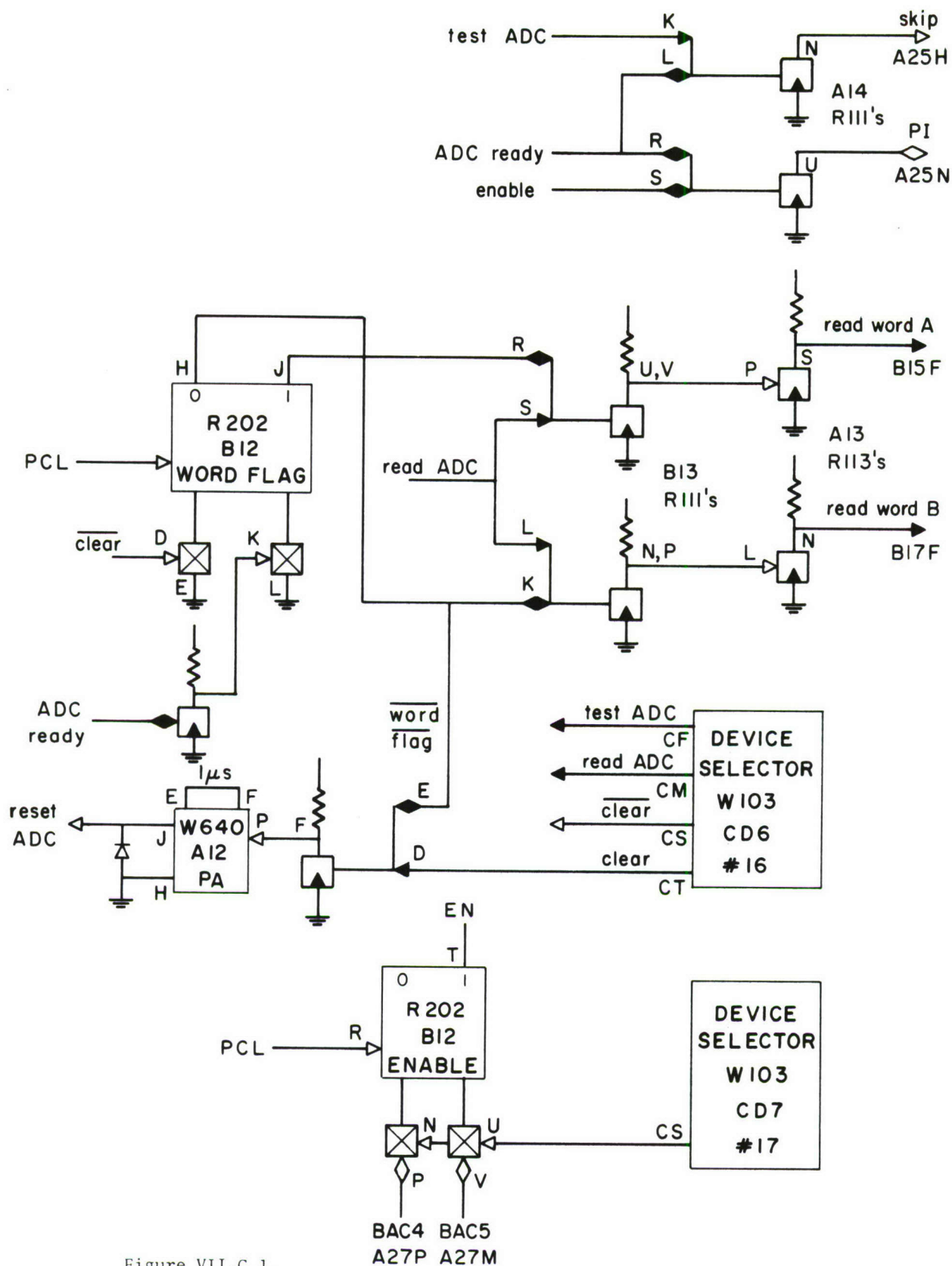


Figure VII.C.1.

reads WORD A into the computer and resets the WORD FLAG. The second READ ADC followed by CLEAR reads WORD B into the computer and resets the ADC.

The Interrupt gate can be enabled or disabled by program instruction through the ENABLE flip-flop. This is accomplished with IOT pulse 6174, which adjusts the state of the ENABLE flip-flop according to the presence or absence of ones in the accumulator bits 4 and 5.

The interface, including logic level converters, was built using Flip-Chip modules supplied by Digital Equipment Corporation. The computer requires the levels 0 and -3 volts for logic "zero" and "one", while the ADC delivers levels between 0 and +3 volts.

The following IOT commands have been assigned to the converter system:

6161 Skip on ADC Ready.

6162 Read ADC.

6164 Resets WORD FLAG and resets ADC if WORD FLAG is reset  
(i.e., after second word has been read).

6174 Operating mode determined by accumulator bits 4 and 5.

AC4	AC5	
0	0	No operation.
0	1	Set ENABLE flip-flop.
1	0	Reset ENABLE flip-flop.

#### D. 256 Channel ADC Interface - R. Bondurant

An interface has been constructed to couple a 256 channel ADC to the PDP-8 computer used by the Fission Experimental Group. The ADC was described in the 1967-68 Progress Report. A block diagram of the interface is shown in Fig. VII.D.1. The logic is similar to that of the Northern Scientific ADC interface described in Section VII.C. of this report. The ADC output is transferred to the computer accumulator in one word. With accumulator bits 5 to 11 receiving the ADC data and bits 0 to 3 receiving an identification code.

The ADC interface uses the following IOT microinstructions:

6741 Skip on ADC ready  
6742 Read ADC data  
6744 Reset ADC  
6144 Enable or disable ADC program interrupt as  
determined by accumulator bits 10 and 11.

AC10	AC11	
0	0	No operation
0	1	Enable
1	0	Disable

#### E. SEL Card Reader and Line Printer Interfaces - R. Bondurant

A card reader and a line printer have been interfaced to a System Engineering Laboratories (SEL) 810B computer used by the Kinetic Theory Group.

The SEL 810B is a 16 bit computer, having a memory cycle time of 750 nanoseconds. The 810B I/O structure includes the capability of

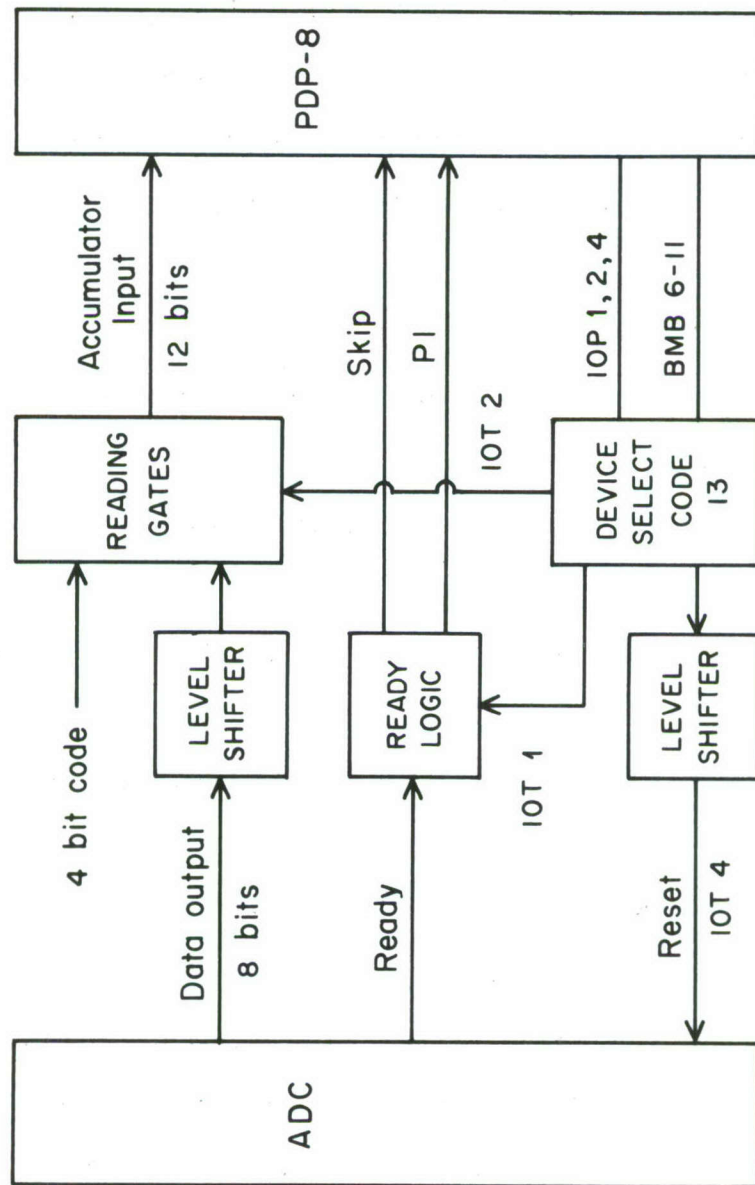


Figure VII.D.1.

## 256 CHANNEL ADC INTERFACE



transferring information under program control between external devices and core memory or the A-accumulator. High speed channels or Block Transfer Control (BTC) units are also available for transferring data in and out of core memory under hardware control. At present, the card reader and line printer are operated only under program control.

Programmed control of I/O devices is accomplished by using the following six I/O instructions to transfer words between the processor and external devices.

CEU (Command External Unit) - outputs a command word to control device functions.

TEU (Test External Unit) - a conditional skip used to interrogate device status.

AIP, AOP (A-Input, A-Output) - transfers words in or out of the A-accumulator.

MIP, MOP (Memory Input, Memory Output) - transfers words in or out of a selected memory location.

I/O instructions (except AIP and AOP) are formed by two memory words. The first word contains the operation code and the six bit device address. The second word is either the instruction operand (immediate mode) or the effective address of the operand (address mode).

I/O instructions, except TEU, can be executed in either a wait mode or a skip mode. In the wait mode, the computer program will halt at the I/O instruction until the device is ready to accept the instruction. In the skip mode, if the device is ready, the instruction

execution is completed and the program operations resume after skipping the next instruction. If the device is not ready, the program does not halt. Instead, the next instruction is executed. This feature allows the program to bypass the I/O instruction if the device is not ready.

#### 1. Data Terminal

I/O devices are connected to the processor by a daisy-chained I/O Bus. The I/O Bus contains 16 bi-directional data lines, 6 device address lines, and 13 control lines. Each device is interfaced to the I/O Bus through a Data Terminal. A Data Terminal contains logic to accept control signals from the processor, interpret them, send control signals back to the processor, and control data transfers.

A general Data Terminal has been developed to facilitate interfacing various devices to the 810B. A complete logic diagram of the Data Terminal is shown in Figure VII.E.1. I/O transfer instructions are executed in the following basic sequence. The processor fetches the first word of an I/O instruction from memory and gates the device address along with control signals appropriate to the instruction out onto the I/O Bus. The address code is used to select a particular Data Terminal by the select logic which is wired to respond only to the desired code.

Signals called Unit Sync Return (USR) and Unit Test Return (UTR) are used to indicate the device status to the processor. The processor will halt at the I/O instruction until it receives the USR. The UTR enables the execution of the I/O transfer. If the instruction is executed in the wait mode, the Data Terminal will not send either





USR or UTR unless the device is ready. In the skip mode, the USR is returned indicating that the device has received the first part of the transfer, but the UTR is returned only if the device is ready.

Transfers are executed only when the processor receives both USR and UTR. For an output transfer, a word is gated out onto the I/O Bus along with the Computer Data Here (CDH) signal. The CDH enables the generation a register strobe pulse to strobe data from the I/O Bus into a register.

The Unit Data Accepted (UDA) signal is then sent back to the processor to indicate that the transfer is completed. For an input transfer, data from the device is gated onto the I/O Bus coincident with the UTR. When the processor has accepted this data, the Computer Data Accepted (CDA) signal is sent to the Data Terminal to indicate completion of the I/O instruction.

## 2. Card Reader

The General Design Incorporated Model 100 Card Reader reads 80 column, 12 row punched cards at rates up to 200 cards per minute. The card reader interface includes a Data Terminal and additional logic to control reader operation and data transfers. The control logic is shown in Fig. VII.E.2.

A CEU instruction initiates reader operation. If the reader is ready and bit 6 of the CEU function word is a "one", the pick flip-flop is set, causing the reader to process one card. The reader selects the next card from the supply hopper and passes it through the read station. During this time, the unit ready signal is held low



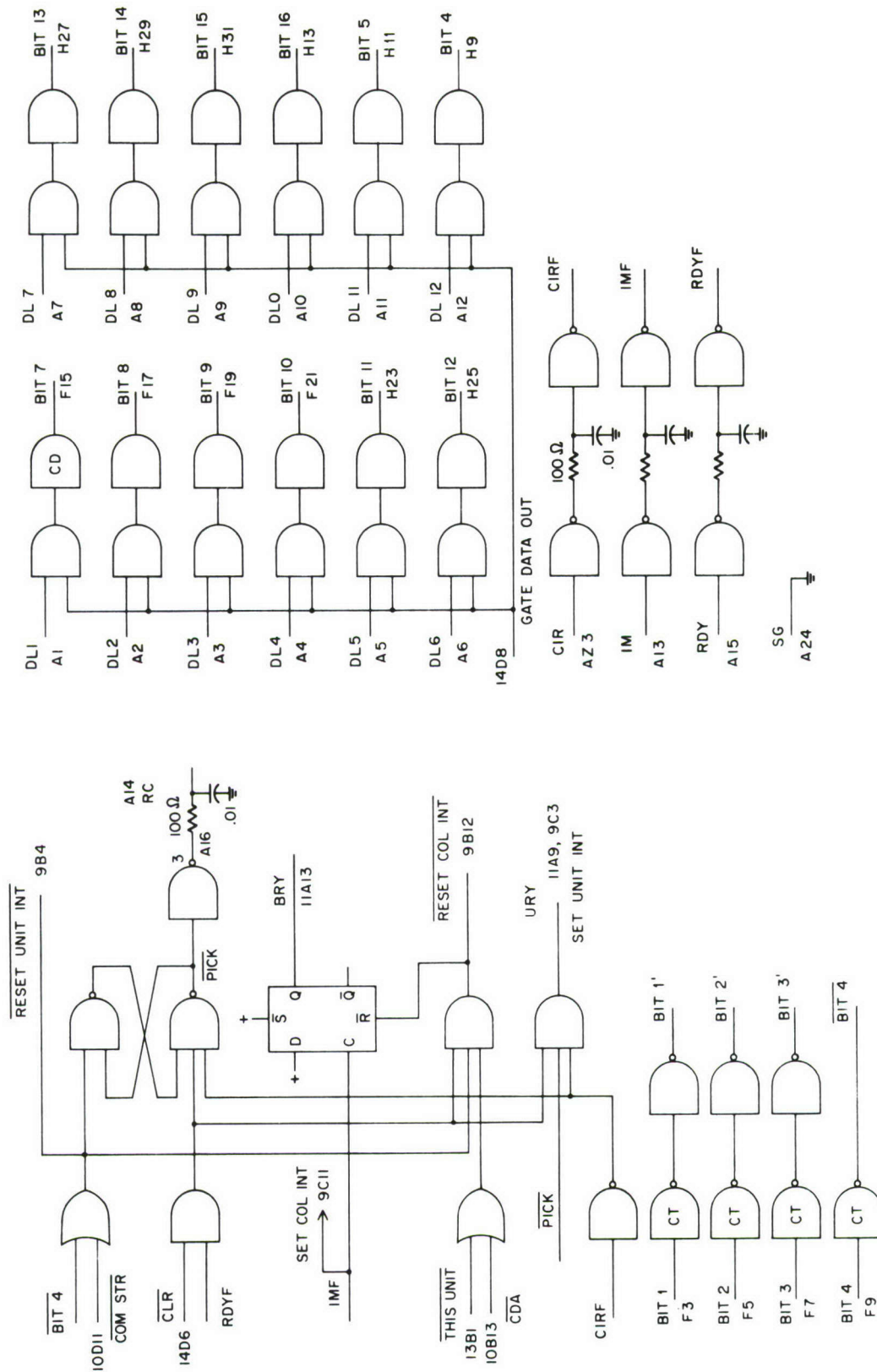


Figure VII.E.2.

to inhibit any additional CEU instructions. As the card passes through the read station, each column of data is read in parallel by 12 photodiodes. Reader timing circuits develop an index marker pulse as each of the 80 card columns is read. Index marker pulses transfer data from the photodiodes into a buffer register in the reader and set a buffer ready flip-flop which enables the execution of an AIP or MIP to transfer data from the register to the processor. The buffer ready flip-flop is reset at the completion of each transfer. After the card has passed the read station, it is stacked in the output hopper.

### 3. Line Printer Interface

The Datamark Series 300 line printer can print text in lines of up to 132 characters at a maximum rate of 300 lines per minute. A 6 bit ASCII coded character set is provided. A line to be printed is assembled in the printer buffer character by character. When a line is complete, a program command initiates the print cycle. When the print cycle is finished, the paper may be advanced. The program may assemble the next line during the paper advance cycle. If a print command is issued when the buffer has been loaded with less than 132 characters, the remaining columns will be left blank.

A block diagram of the printer controller is shown in Figure VII.E.3. Printer mechanical operations are initiated by CEU instructions. The vertical format and print logic decodes the instructions and commands the printer to print a line, advance the form one line, or advance to the top of the form. AOP or MOP instructions are used for

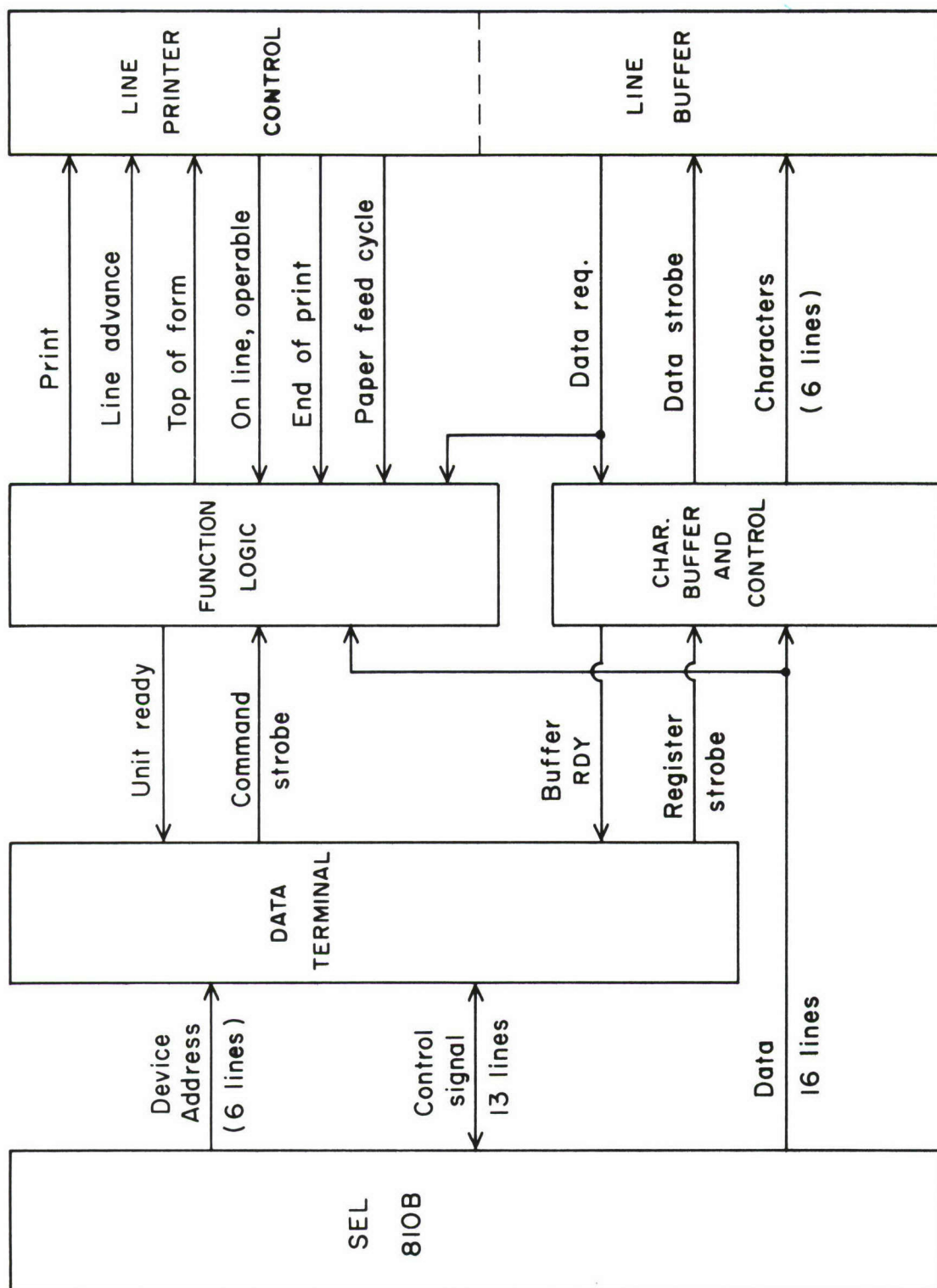


Figure VII.E.3.

## LINE PRINTER INTERFACE

loading the print buffer under control of the data transfer logic. Output data is transferred to the printer through a register in the controller.

Printer status is defined by two flags 'unit ready' and 'buffer ready'. The 'unit ready' flag is set if the unit is operable, on line, and not in a print or paper advance cycle. CEU instructions can be executed only if the unit ready flag is set. AOP and MOP instructions are enabled by the buffer ready flag when the printer is operable, on line, and not in a print cycle and the print buffer is not full.

Priority interrupts are available to indicate the end of the print cycle, the end of the line feed cycle, and that the buffer ready flag is set.

#### F. Incremental Plotter Control - V. Guiragossian

An Interface-Control unit is being designed to connect a Calcomp incremental plotter to the SEL 810B computer used by the Macroscopic Neutron Physics Group.

The Calcomp model 565 is a digital two-axis drum type plotter capable of producing high quality graphic presentation of the computer output data.

Drum type plotters produce one increment of pen movement relative to the surface of the paper for each input command executed. The Y-axis plot is produced by lateral movements of the pen carriage while the X-axis plot is produced by rotary motion of the chart drum.

The basic movements on each axis are 0 degrees and 90 degrees. The plotter can be commanded to plot increments of +x, -x, +y, -y, or combinations of x and y increments. Only one command is necessary



to plot a point at  $45^\circ$ ,  $135^\circ$ ,  $225^\circ$  or  $315^\circ$ . The remaining two movements are pen up and pen down. Operating speed is 300 increments per second with a plotting increment of 0.01 inch.

Figure VII.F.1. is a block diagram showing the manner in which the plotter is coupled to the computer.

The computer instruction used to control the plotter is Command External Unit (CEU). Each CEU instruction is a two word communication. The first word determined if the plotter is ready to accept a command and the second word contains the information necessary to generate one or more plot commands.

The first word of the CEU instruction contains the six Unit Select bits which are sent to the Address Decode circuits. If the unit is selected and ready the computer then places the second word of the instruction on the computer I/O data lines.

Six bits of the second word of the CEU command are used as control bits and are received into the Function Decode logic circuits. The commands are then strobed to the plotter lines when computer timing pulses are output. The Function Decode Logic also determines when the plotter is able to accept plot commands.

The plotter is able to accept more than one plot command simultaneously. Each incremental step can be in any one of eight directions through appropriate combinations of the X and Y axis instructions provided that the commands are not contradictory.

The Plotter Control logic uses one of the two standard Priority Interrupts which, if enabled, will be sent to the computer after the time required to perform the plot command has elapsed. The

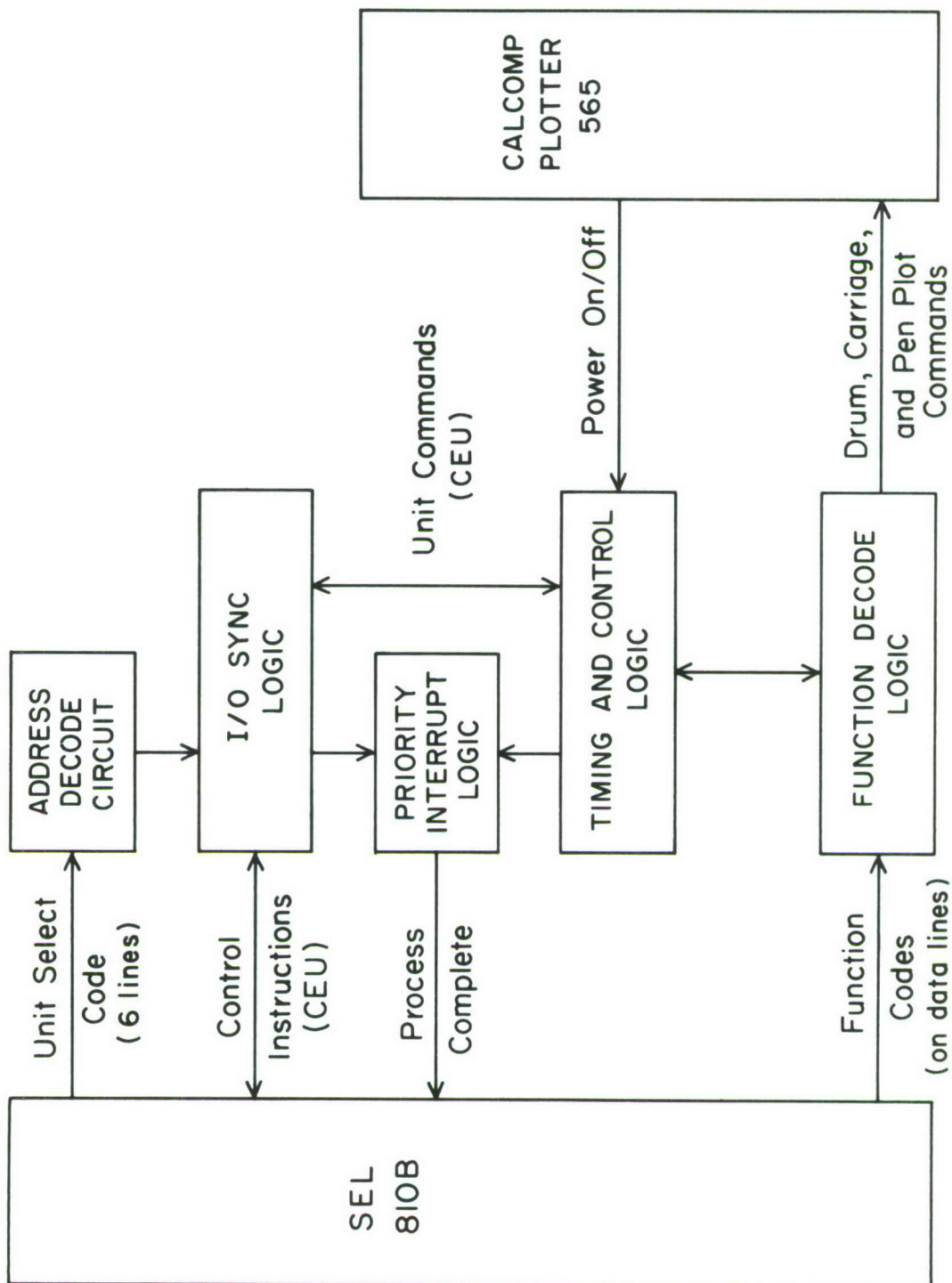


Figure VII.F.1.

interrupt circuits are enabled or disabled by CEU instructions in the program. A single CEU instruction can enable or disable the interrupt circuit depending on the state of bits 1, 2 and 3.

If the priority interrupt circuit is enabled, an interrupt command is presented to the computer at the end of each plot command in preparation for the following plot command.

#### G. Card Reader and Control - V. Guiragossian

A logic control unit is being designed to interface a GDI card reader to the PDP4 computer in use at the Van de Graaff accelerator experimental area.

When completed this unit will enable the computer to accept program material in the form of standard IBM punched cards. At present the development or modification of programs has to proceed using the teletype and paper tape reader through the computer itself, which is seldom free since it is used on line running with the accelerator.

The GDI model 100 card reader is a small table-top unit which employs a photoelectric read station and a unique vacuum pick finger to separate a single card from the input deck. This picking technique allows the reader to process damaged cards, even cards that have been stapled, patched or cards with uneven edges. Cards are processed with a reading speed of up to 200 cards per minute, and throughout the operation light current checks, dark current checks and card motion checks are continuously performed to verify the proper operation of the reader.

Figure VII.G.1. is a simplified block diagram of the reader control logic which works in the following way:

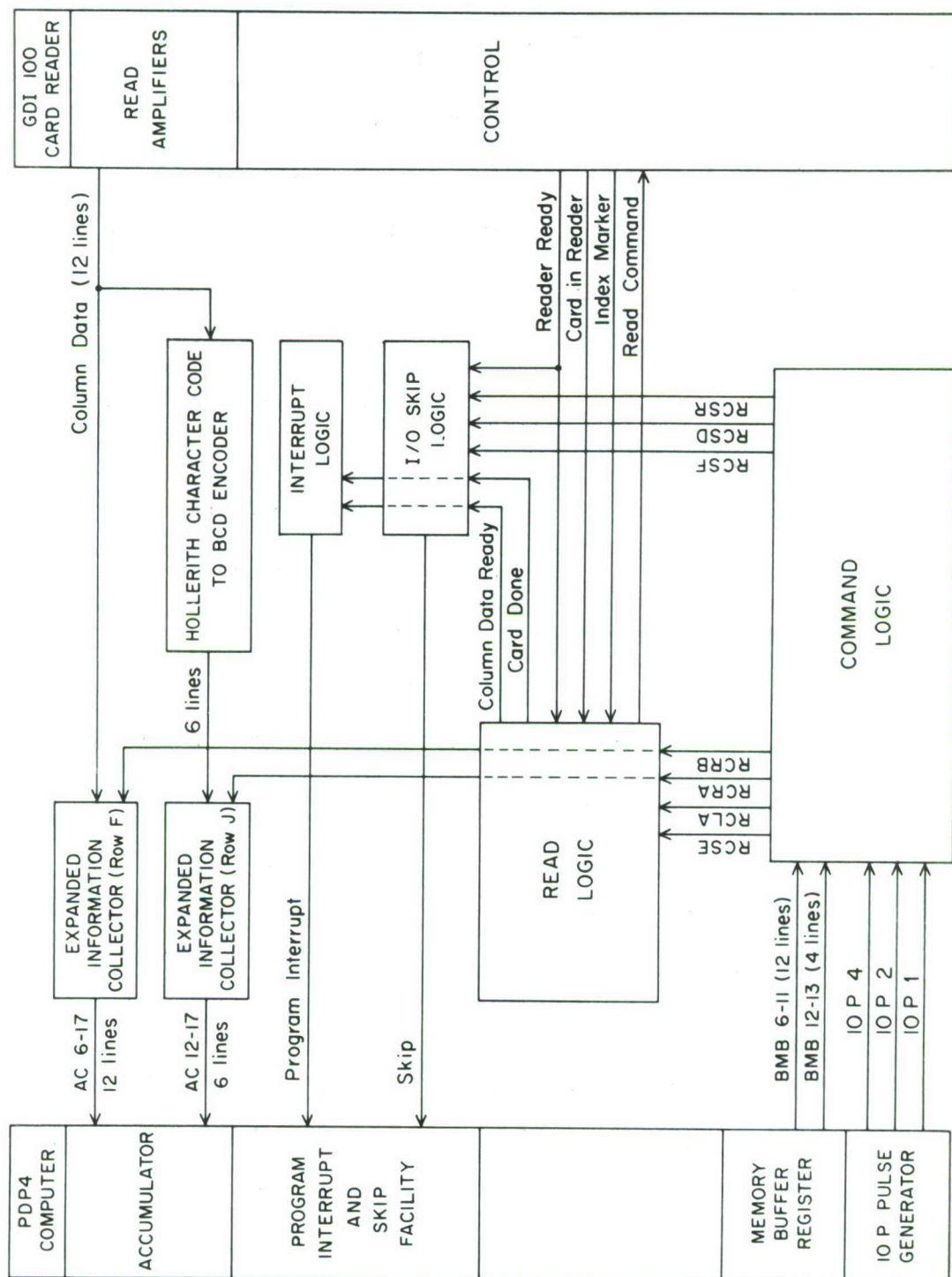


Figure VII.G.1.



A read sequence is started when a Read Command signal from the Read Logic circuit is fed to the card reader as a result of the issuance of a Select Command (RCSE) from the Command Logic. The cards are read column by column with the data being presented in bit parallel, character serial format on twelve output lines in synchronism with a timing signal IM (Index Marker).

A Ready line from the reader will signal the control unit that the reader is in an operable condition and awaiting a Read Command input. A Read Command RC may be supplied anytime the Ready line (RDY) is high and the Card In Reader line (CIR) is low. The CIR signal reports the presence of a card in process at the read station.

In the event of trouble the RDY line is inhibited and the reader will stop. Error indicator lights will show the cause of the non-operable condition which may be: hopper empty, stacker full, or photocells not lit. Motor Start is used as a reset to clear the error indicators and start the card reading process over again.

Column information may be read in one of the two program selected modes: alphanumeric or binary.

In the alphanumeric mode, the 12 information bits in one column are interpreted as a Hollerith character code. The Encoder circuit automatically translates these bits into a 6-bit card reader code for the character which has been read. This code transfers into the least significant bits of the accumulator through the information collector facility of the computer.

In the binary mode, the 12 bits of each column are accepted directly as a 12 bit binary number and are transferred into the accumulator bits 6 through 17.

Three program flags are associated with the reader control logic. They are used to indicate card reader conditions to the computer through the interrupt and input/output skip facility. These flags are Reader Ready, Column Data Ready and Card Done. The Column Data Ready and Card Done flags are connected to the Program Interrupt and I/O Skip lines, and may be individually tested by a skip instruction in preparation for the next "read a column" or "select a card" commands respectively. The Reader Ready flag is connected only to the skip line.

All command signals as well as I/O skip test pulses are produced in the Command Logic circuit by decoding computer instructions.

The design of the reader logic has been completed and the unit will soon be built.

#### H. Single Channel Analyzer - T. Becker

A Timing Single Channel Analyzer has been designed and built, using integrated circuit discriminators and logic. The use of integrated circuits improves reliability and reduces construction time.

There are two versions of the Single Channel Analyzer (SCA) presently available. The general purpose model 75 SCA has a 5 volt input range and enables the user to select leading edge or zero cross-over timing. The model 74, with a 1 volt input range and leading edge timing, was designed to analyze the output from photomultipliers used with NaI detectors with no intervening amplification. The next neutron velocity spectrometer run at Nevis will use 14 model 74 SCA's with the time-of-flight system.

The basic single channel analyzer consists of three independent discriminators. Two are amplitude discriminators and the third is a timing discriminator. A mode switch enables the user to select differential or integral operation. In the differential mode, an output is generated for input signals that trigger the timing discriminator and are greater than the lower level discriminator (LLD) and less than the upper level (ULD). The upper level discriminator is disabled in the integral mode. Two lights on the panel warn the user if the upper level is set less than the lower level or if the lower level is less than the leading edge (LE) timing discriminator.

Referring to Figure VII.H.1., the circuit operates in the following manner. Each upper and lower level discriminator consists of a high-speed differential comparator, Fairchild 710C, followed by a 1 ma current switch,  $Q_1$  and  $Q_2$ . A positive input is applied to the inverting input of the comparator. When the input amplitude exceeds the threshold level set by the 500  $\Omega$  ten turn Helipot, the comparator output state changes and switches the current switch. The 1 ma switched from  $Q_1$  to  $Q_2$  feeds back to the positive input of the comparator. This produces a hysteresis varying from 5 mv to a maximum of 500 mv, when the bias is at its highest value.

Use of the Fairchild 710C comparator provides a very stable discriminator threshold. In model 75, where  $R_3$  has a value of 510 ohms, the input drift is less than 50  $\mu$ volts/ $^{\circ}$ C. As a percent of the full input range, this corresponds to approximately 0.002%/ $^{\circ}$ C







for both models. However, the overall stability is  $.01\%/^{\circ}\text{C}$ , since both discriminator threshold voltages are derived from the +24 volt NIM power supply, which has a specification of  $.01\%/^{\circ}\text{C}$ .

The timing discriminator is similar to the level discriminators, with the exception that the reset level can be set independently of the threshold level. The initial bias level is determined by the voltage on the 24 ohm resistor at the positive input of the timing comparator. This bias voltage is controlled by the current through the current switching pair  $Q_{13}$  and  $Q_{14}$ . The ten-turn LE potentiometer varies the current over a range of 0 to 17 ma, which corresponds to an initial bias voltage of 0 to 400 mv. When the comparator is turned on,  $Q_{14}$  switches off, so that its current no longer flows through the 24 ohm resistor. The RESET potentiometer is adjusted such that the comparator resets at some voltage from 0 to 90 independent of the value of the initial threshold level. The RESET can be adjusted so that the timing discriminator reset occurs at the baseline crossover of the input pulse, when used with bipolar pulses, or at some small positive value when used with unipolar pulses.

The three set-reset flip-flops U, L, and T are set by the leading edge of the outputs from the upper, lower, and timing discriminators, respectively. In addition, the R flip-flop is set by the trailing edge or reset of the timing discriminator. The output from the R flip-flop, delayed by the RESET DELAY of 350 nsec, resets all four flip-flops independent of the mode of timing.

Zero Crossover (ZC) or Leading Edge (LE) timing may be selected by toggle switch on the front panel. For the zero crossover

mode, the output from R is differentiated by gates C and D and then "ANDed" at gate J with the outputs L and U. An output from gate J obtained at a time corresponding to the baseline crossing of an input pulse whose amplitude is between the upper and lower levels selected.

The LE mode selects the T flip-flop output delayed by the LE DELAY as the input to the coincidence gate J. The delay is inserted in order to allow the input of the SCA to reach its maximum amplitude for correct operation of the upper and lower discriminators. The standard LE DELAY is variable from 0.4 to 1.0  $\mu$ sec with a stability of 0.05%/°C. A smaller timing capacitor can be used with fast rise-time signals to obtain an output as early as 70 nsec from the leading edge of the input signal.

The output from the coincidence gate J triggers the OUTPUT WIDTH Univibrator, consisting of gates E and J, to provide 60 nsec. positive and negative pulses at the output. A visual indication that the SCA is operating is given by lamp.  $L_3$ , which is turned on for 8 msec for each output pulse.

The SCA is constructed on a double sided printed circuit board and housed in a single width NIM module. All logic gates and flip-flops are Sylvania SUHLII TTL integrated circuits. These circuits are characterized by 5 nsec risetimes and 6 nsec gate propagation delays. Logic levels of 0 and 3 volts are "zero" and "one", respectively. The power required from the NIM Bin is: +12v, 260 ma; +24v, 50ma; -12v, 75ma; -24v, 15ma.

## I. A Time Pick-Off Circuit for the Van de Graaff Accelerator -

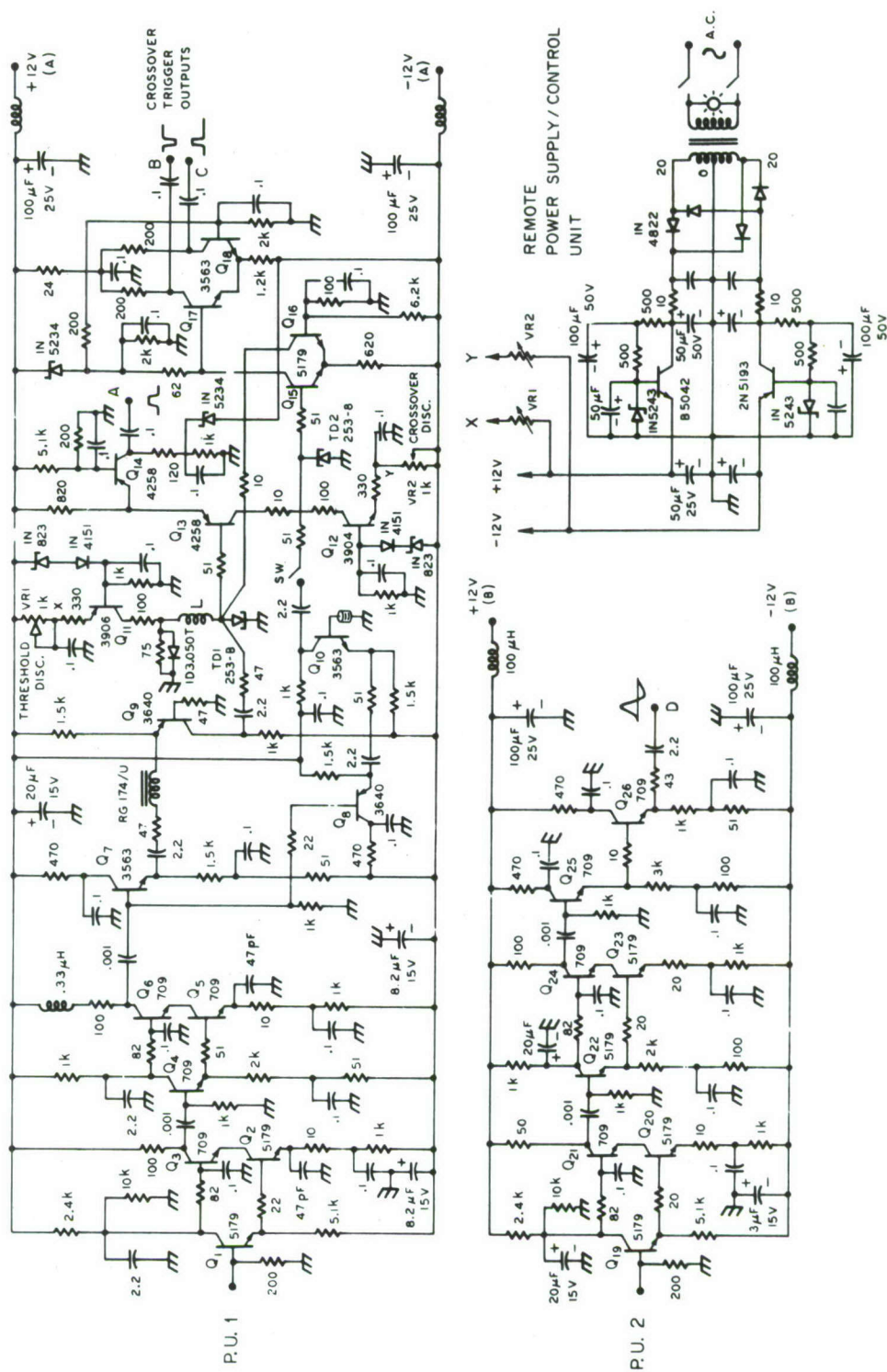
I. J. Taylor and T. Becker

A time pick-off circuit has been constructed for use with the 5 MHz pulsed beam of the Van de Graaff accelerator. The requirements of the circuit are to detect the beam burst and provide an output timing signal with as low a time-walk as possible and also to provide a linear amplification of the beam burst for direct oscilloscope display. The sensitivity of the system was required such that it would operate with a time averaged beam of as low as 0.5  $\mu$ A from the accelerator.

To avoid time walk dependence on the timing signal a "true-zero crossover" detector is used with a threshold discriminator priming the crossover detector circuit, as explained below. Since the zero crossover point is the same for all pulse heights, "true zero-crossover" timing eliminates time walk dependence on beam intensity variations, timing jitter then being more closely related to high frequency noise on the pulse.

The circuit is shown in Fig. VII.I.1. and is used in conjunction with the time pick-off cylinder arrangement described in Section II.A. of this report. It was decided to use separate circuit sections for the time pick-off triggering and the linear amplification stages as the triggering stage should have fast crossover as its primary concern, rather than linearity. Direct connection is made at the base of transistor  $Q_1$  to the upper time-pick-off- cylinder, and a positive going bipolar pulse is developed as the beam burst passes through the cylinder. Transistors  $Q_1 \rightarrow Q_6$  comprise two cascode stages in a configuration that







has been analyzed by Williams and Neiler (IRE Trans. Nucl. Sci. NS9, 1 (1962)). Interstage gain is maintained by use of  $Q_4$  as a driver, and negative feedback at each cascade stage is obtained through the emitter resistor, decoupled for high frequency gain.

The output of the cascade amplifier branches at  $Q_7$  and  $Q_8$  through current drivers  $Q_9$ ,  $Q_{10}$  to the tunnel diodes TD1 and TD2. The signal to TD1 is cable delayed by approximately 1 1/2 nanoseconds to ensure that the priming of TD2 (by TD1) occurs while a positive-going signal is present at TD2. Tunnel diode TD1 forms the active part of the Threshold Discriminator set by adjustment of helipot VR1 which is part of an external control unit. Transistor switching pair  $Q_{13}$ ,  $Q_{14}$  with  $Q_{13}$  normally ON provides approximately 13 mA of suppression bias current to TD2 and this current is released when the Threshold Discriminator is triggered. The width of the triggering pulse is determined by choke L, typically 2  $\mu$ H, and is set to be approximately 15 to 20 nanoseconds thus adequately covering the time of crossover of the positive-going bipolar pulse presented at TD2. A Threshold Discriminator output pulse is obtained (at A) from the collector of  $Q_{14}$ .

Tunnel diode TD2 forms part of the cross-over Discriminator, set by adjustment of helipot VR2 which (like VR1) is included in an external control unit at the Van de Graaff control desk. Current through  $Q_{12}$  is adjusted such that on release of the reverse bias current from  $Q_{13}$  tunnel diode TD2 is set at its switching point and is triggered into the forward conduction region on the negative-going crossover. Transistors  $Q_{15}$ ,  $Q_{16}$  form a fast reset circuit restoring TD1 and TD2 to

their original states. When TD2 triggers on detection of crossover,  $Q_{15}$  (normally ON) is turned OFF and standing current of approximately 18 mA is diverted to TD1 overcoming the threshold bias, forcing TD1 to return to backward conduction and turning transistor  $Q_{13}$  ON. When  $Q_{13}$  is turned ON, the suppression bias current of 13 mA returns to TD2 which is also forced into backward conduction. This sequence is quite fast, and the Crossover Discriminator resets in approximately 5 nanoseconds. Transistor switching pair  $Q_{17}$ ,  $Q_{18}$  respond to the Crossover Discriminator output at the collector of  $Q_{15}$  and positive and negative going output timing pulses are obtained at C and B from the collectors of  $Q_{18}$  and  $Q_{17}$ . The negative output is used as the START signal for time-of-flight experiments and the positive going signal is used for triggering a sampling oscilloscope in the control room which displays the linear signal obtained from the amplifier section ( $Q_{19} \rightarrow Q_{26}$ ) of the circuit. Direct connection to a second pick-up cylinder is made at the base of  $Q_{19}$  and signal amplification occurs through two cascode stages, similar to the arrangement described earlier, with transistors  $Q_{25}$ ,  $Q_{26}$  as output drivers. The amplified signal (at D) is fed to the sampling oscilloscope via approximately 20ft of RG 8/U cable terminated in 50 ohms by the oscilloscope input. The amplifier gain, for a 5 nanosecond test pulse, is approximately 15 X and amplifier rise time approximately 2 nanoseconds. The +12v, -12v power supply for the circuit is contained in the external control unit and consists simply of zener regulated pass transistors. The ripple at the outputs is approximately 2 millivolts peak to peak. Separate filtered output lines are taken to the timing and linear amplifier sections of the circuit

which are well isolated to prevent pick-up of fast transients. Within the circuit the bias currents defining the discriminator levels of TD1 and TD2 are obtained from current sources  $Q_{11}$ ,  $Q_{12}$  referenced to temperature compensated zener diodes (IN 823) and with first order temperature compensation using silicon diodes across the base/emitter junctions.

As with the majority of fast amplifier circuits, the construction and layout are important aspects of the final performance. Thus the layout and wiring are made in accordance with high frequency practice using minimum lead length, utilizing the ground plane to minimize pick-up, and inserting filtering condensers directly at active points. Nevertheless, the original circuit, designed for the fast type 2N 5179 and the slower type 2N 709 transistor in the cascode stages. The initial layout, governed primarily by the required direct connection of the circuit to the time pick-off cylinder unit, was not subsequently optimised for amplifier performance.

To assist in the initial set-up when using the circuit, a switch (SW) is inserted between  $Q_{10}$  and TD2. With the switch open, and beam bursts activating TD1 as observed by detection of Threshold Discriminator output events at A, the Crossover Discriminator is adjusted until trigger output events are just being generated (at outputs B and C). This indicated TD2 is set at its switching peak and very close to the "true zero crossover" detection point. In practice, having determined this operating point only slight adjustment has been required of the Crossover Discriminator whose dial settings seem



to be quite reproducible. This procedure, though not as precise as the more rigorous method of determining true crossover detection via minimum time walk as a function of pulse amplitude, is more amenable to general purpose use of the circuit. Figure VII.I.2. shows a dual trace sampling oscilloscope display for the circuit in operation with a pulsed proton beam from the accelerator. The upper trace shows the linear signal obtained from the lower pick-off cylinder. The signal is bipolar, representing  $V = R \frac{d}{dt} Q(t)$  where  $Q(t)$  is the charge induced by the beam burst entering and departing from the cylinder, and  $R$  is the input resistance. The recovery of the negative undershoot is determined by the input time constant of the circuit, formed by  $R$  and lumped 'cylinder-plus-stray' input capacitance. The sharpness of the rising pulse is related to the time compression of the beam burst. The sharpness of the rising pulse is related to the time compression of the beam burst. The lower trace shows the crossover timing signal that is generated by the circuit.



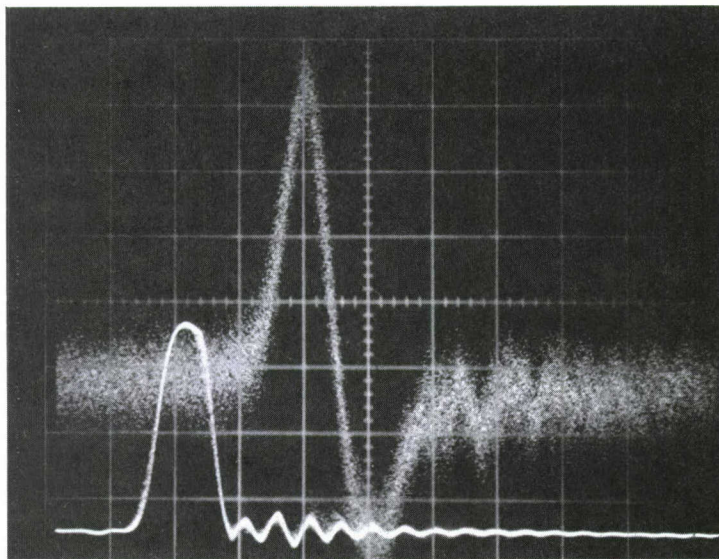


Fig. VII.I.2. A dual trace sampling oscilloscope display for the time pick-off circuit in operation with a pulsed proton beam from the Van de Graaff accelerator. The upper trace shows the linear signal obtained from the lower pick-off cylinder. The time scale is 5 nanoseconds per cm. and the vertical scale is 5 millivolts per cm. The lower trace shows the crossover timing signal that is generated by the circuit. The vertical scale for the lower trace is 200 millivolts per cm.

## APPENDIX A

### JOURNAL PUBLICATIONS

1. C. S. Wu and L. Wilets, "Muonic Atoms and Nuclear Structure," Ann. Rev. of Nuclear Science, Vol. 19 (1969).
2. Y. W. Chow, E. S. Greenbaum, R. H. Howes, F. H. H. Hsu, P. H. Swerdlow, and C. S. Wu, "Mössbauer Effect Following Coulomb Excitation Measurements of Electric Quadrupole Moment Ratios in the First Excited  $2^+$  States of  $W^{182,184,186}$ ," Physics Letters 30B, 3 (1969).
3. W. Y. Lee, S. Bernow, M. Y. Chen, S. C. Cheng, D. Hitlin, J. W. Kast, E. R. Macagno, A. M. Rushton, C. S. Wu and B. Budick, "Finite Distribution of Nuclear M1 and E2 Moments in Muonic  $^{115}\text{In}$ ,  $^{133}\text{Cs}$  and  $^{141}\text{Pr}$ ," Phys. Rev. Letters 23, 648 (1969).
4. C. Ho, Book review of "Fast Breeder Reactors - Proceedings of the London Conference, Organized by the British Nuclear Energy Society, May 1969," Nuclear Engineering and Design 4 (1969).
5. M. Y. Chen, "Nuclear Polarization in Muonic Atoms of Deformed Nuclei," submitted to Physical Review, November 1969.
6. M. Y. Chen, "Nuclear Polarization in Muonic Atoms of Spherical Nuclei," submitted to Physical Review, November 1969.
7. W. Y. Lee, S. Bernow, M. Y. Chen, S. C. Cheng, D. Hitlin, J. Kast, E. Macagno, A. M. Rushton and C. S. Wu, "The Resonance Process and the Intensity Anomaly in Muonic  $^{127}\text{I}$ ," submitted to Phys. Rev. Letters, 1969.
8. B. Lawergren, G. C. Neilson, J. L. Honsaker, "K = 1/2 and K = 5/2 Components in the Ground States of  $^{27}\text{Al}$ ," Physics Letters 30B, 470 (1969).
9. B. Lawergren, I. J. Taylor, M. Nessim, "Nuclear Structure in the  $\gamma$ -decay of Isobaric Analog States in  $\text{Mg}^{24}$ ,  $\text{Al}^{27}$  and  $\text{Si}^{28}$ ," submitted to the Physical Review, 1969.
10. J. D. Ullman, C. S. Wu and P. Harihar, "Search for Double Gamma Emission from the First Excited States of  $\text{Ca}^{40}$  and  $\text{Zr}^{90}$  to be published in Physical Review.
11. J. Markisz and J. D. Gelter, "Quantitative Aspects of Base-Catalyzed Michael Addition," Can. J. Chem. 47, 1965 (1969).

12. T. I. Taylor and M. Jeevanandam, "Preparation of 99.5% Nitrogen-15 by Chemical Exchange between Oxides of Nitrogen in a Solvent Carrier System," *Advan. Chem. Ser.*, No. 89 (1969), Am. Chem. Soc.
13. F. Rahn et al., "Neutron Resonance Spectroscopy  $\text{Sm}^{150,154}$ ,  $\text{Sr}^{86,87,88}$ ," *BAPS* 14, #12, 1235 (1969).
14. D. Cokinos, E. Melkonian, W. W. Havens, Jr., "Neutron Thermalization Experiments in Pulsed Gadolinium-Poisoned Assemblies," *Transactions of the American Nuclear Society*, 12, #2 (1969).
15. D. Hitlin, S. Bernow, S. Devons, I. Duerdoth, J. Kast, E. Macagno, J. Rainwater, C. S. Wu, R. C. Barrett, "Muonic Atoms I: Dynamic HFS in the Spectra of Deformed Nuclei," submitted to the *Physical Review*, November 1969.
16. E. Macagno, S. Bernow, S. C. Cheng, S. Devons, I. Duerdoth, D. Hitlin, J. Kast, W. Y. Lee, J. Rainwater, C. S. Wu, R. C. Barrett, "Muonic Atoms II: Isotope Shifts," submitted to *Physical Review*, November 1969.
17. E. Melkonian, M. Derengowski, "Double Energy, Single Time-of-Flight Measurements of Fission Fragments in Thermal Neutron-Induced Fission of  $\text{U}^{235}$ ," submitted to *Physical Review*, December 1969.
18. P. Harihar, J. D. Ullman, C. S. Wu, "Search for Double Gamma Emission from the First Excited States of  $\text{Ca}^{40}$  and  $\text{Zr}^{90}$ ," submitted to *Physical Review*, December 1969.



## APPENDIX B

### PAPERS PRESENTED AT MEETINGS

1. M. Slagowitz, J. Hahn, J. Rainwater, W. W. Havens, Jr., "Neutron Velocity Spectrometry, Data Acquisitions on Analysis," Skytop Conference on Computer Systems in Experimental Nuclear Physics, March 3-6, 1969.
2. B. Lawergren, M. Nessim, I. J. Taylor, "Some M1 Transitions with  $\Delta T = 1$  in  $^{24}\text{Mg}$ ,  $^{27}\text{Al}$  and  $^{28}\text{Si}$ ," Second Conference on Nuclear Isospin, Asilomar, Calif., March 13-15, 1969 (APS).
3. E. Melkonian, J. Felvinci, "Channel Effects in the Interactions of Resonance Energy Neutrons with  $\text{U}^{233}$ ," Conference on Physics and Chemistry of Fission, IAEA, Vienna, July 1969.
4. D. Cokinos, E. Melkonian, "Neutron Thermalization Experiments in Pulsed Poisoned Moderators," Summer Conference of the ANS, Seattle, Wash., June 15-19, 1969 (Transactions of Am. Nucl. Soc., I., 258, 1969).
5. J. Rainwater, W. W. Havens, Jr., J. B. Garg, "High Resolution Total Neutron Cross Section in Vanadium," IUPAP Montreal Meeting on Nuclear Physics, August 25, 1969.
6. F. Rahn, H. Camarda, G. Hacken, W. W. Havens, Jr., H. Liou, J. Rainwater, M. Slagowitz, S. Wynchank, "Neutron Resonance Spectroscopy IV:  $\text{Eu}^{151}$  and  $\text{Eu}^{153}$ ," 1969 Spring Meeting of the American Physical Society, Washington, D.C.
7. H. Liou, H. Camarda, G. Hacken, W. W. Havens, Jr., F. Rahn, J. Rainwater, M. Slagowitz, S. Wynchank, "Neutron Resonance Spectroscopy V: Argon and the Isotopes of Yb and Er," 1969 Spring Meeting of the American Physical Society, Washington, D.C.
8. M. Slagowitz, H. Camarda, G. Hacken, W. W. Havens, Jr., H. Liou, F. Rahn, J. Rainwater, S. Wynchank, "Neutron Resonance Spectroscopy VI: R-Matrix Analysis of Total Neutron Cross-Section Data," 1969 Spring Meeting of the American Physical Society, Washington, D.C.
9. S. Wynchank, H. Camarda, G. Hacken, W. W. Havens, Jr., H. Liou, F. Rahn, J. Rainwater, M. Slagowitz, "Neutron Resonance Spectroscopy I:  $\text{Hf}^{177}$ ,  $\text{Gd}^{152}$ ,  $\text{Gd}^{154}$ ,  $\text{Lu}^{175}$ ," 1969 Spring Meeting of the American Physical Society, Washington, D.C.



10. H. Camarda, G. Hacken, W. W. Havens, Jr., H. Liou, J. Rainwater, F. Rahn, M. Slagowitz, S. Wynchank, "Neutron Resonance Spectroscopy II:  $W^{182}$ ,  $W^{184}$ ,  $W^{186}$ ," 1969 Spring Meeting of the American Physical Society, Washington, D.C.
11. G. Hacken, H. Camarda, W. W. Havens, Jr., H. Liou, F. Rahn, J. Rainwater, M. Slagowitz, S. Wynchank, "Neutron Resonance Spectroscopy III:  $La$ ,  $In^{113}$ ,  $In^{115}$ ," 1969 Spring Meeting of the American Physical Society, Washington, D.C.
12. M. Y. Chen, "Nuclear Polarization in Muonic Atoms of Deformed Nuclei," 1969 Fall Meeting of the American Physical Society, Boulder, Colorado, October 1969.
13. M. Y. Chen, "Nuclear Polarization of Muonic Atoms in Spherical Nuclei," 1969 Fall Meeting of the American Physical Society, Boulder, Colorado, October 1969.
14. C. Ho, "Fast Neutron Physics and Thermonuclear Research," Symposium on Applications of Small Accelerators, New York City, April 8 and 9, 1969.
15. C. Ho, F. Rahn, "Measurement of the Cross Section Resonance Parameters and Integral of  $Eu^{151}$ ,  $Eu^{153}$ ,  $Sm^{153}$ , and  $Sm^{154}$ ," ANS winter Meeting, San Francisco, December 1969.
16. E. Macagno, S. Bernow, M. Y. Chen, S. Cheng, D. Hitlin, J. Kast, W. Y. Lee, C. S. Wu, "Muonic Isotope Shifts in Tin," 1969 Fall Meeting of the American Physical Society, Boulder, Colorado, October 1969.
17. J. Kast, S. Bernow, S. Cheng, D. Hitlin, W. Y. Lee, E. Macagno, A. Rushton, C. S. Wu, "Isotone Shift in Muonic X-Rays in the Tin Region," 1969 Fall Meeting of the American Physical Society, Boulder, Colorado, October 1969.
18. H. Goldstein, W. Preeg, "Effects of Cross Section Minima on Deep Penetration of Neutrons," American Nuclear Society Meeting, Seattle, Wash., June 15-19, 1969 (Trans. Amer. Nucl. Soc. 12, #1, 1969).
19. L. Lidofsky, "Contrasts and Similarities in Systems on Large and Small Computers" Ispra Nuclear Electronics Symposium, May 1969.
20. W. Preeg, "Group Averaging Using Supertog with Arbitrary Flux Weighting," Seminar Workshop on Group Cross Sections, Radiation Shielding Information Center ORNL, October 1969.

## APPENDIX C

### DISSERTATIONS

1. Study of Neutron Density Fluctuation Phenomena, R. Goldstein, 1969.
2. A New Moment Solution to the Neutron Transport Equation, C. Weisbin, 1969.
3. Nuclear Hyperfine Interactions in Tungsten-182, 184, 186 as Studied by the Mossbauer Effect Following Coulomb Excitation, E. Greenbaum, 1969.